Characteristics and Dynamics of the Boundary Layer in RF-driven Sources for Negative Hydrogen Ions

Dissertation zur Erlangung des Doktorgrades
an der Mathematisch-Naturwissenschaftlichen Fakultät
der Universität Augsburg

vorgelegt von

Christian Wimmer

am 10.06.2014

Vorgelegt am 10.06.2014

Tag der mündlichen Prüfung: 16.10.2014

Contents

1 Introduction

Fusion power plants based on magnetic confinement can be an important component of worldwide climate neutral energy supply in the future. A major step towards commercial fusion reactors is the international ITER[1] fusion experiment currently under construction in Cadarache, France.

Heating systems are necessary in order to achieve the large (> 100 mio. K) temperature required for the fusion process of deuterium and tritium. Neutral Beam Injection (NBI) is used to heat the fusion plasma by a beam of fast deuterium atoms. In addition, NBI systems have also the possibility to partially drive the required toroidal current in a tokamak fusion device. A NBI system consists of an ion source, which delivers the required current of deuterium ions, an extraction and acceleration system consisting of several grids accelerating the ions to the required particle energy and a neutralizer, where the accelerated ions are neutralized by charge exchange collisions. Due to limitations of the neutralization efficiency at the required high particle energies, the ITER NBI system has to be based on negative hydrogen ions[2]. A prototype negative hydrogen ion source has been constructed successfully at IPP Garching[3], in which the production of negative hydrogen ions takes place by a surface process. Impinging hydrogen atoms or positive ions, which are created in a hydrogen plasma, are converted into negative hydrogen ions on a caesiated grid. Caesium is required for this process in order to reduce the work function of the metallic surface to approximately half the value. Since caesium is chemically very reactive and there are no ultra high vacuum conditions in these sources, caesium has to be repeatedly or even continuously evaporated into the source in order to achieve a spatial homogeneous and temporal stable work function of the conversion surface. The source needs to be capable to deliver the required negative ion current for a duration of up to one hour, which is the maximum length of an ITER pulse.

---

[1]ITER: Latin term for 'the way'

[2]The ITER NBI source must be capable to operate in both isotopes of hydrogen, ^{1}H and ^{2}D.

[3]Max-Planck-Institut für Plasmaphysik, Garching b. München

The performance of these sources is often limited by the amount of electrons, which are inevitably co-extracted combined with negative hydrogen ions. Co-extracted electrons need to be removed out of the beam, which takes place by magnets, bending the electrons onto the second grid of the extraction system prior acceleration to full energy. The maximum tolerable amount of co-extracted electrons is limited by the generated heat load. Experimentally observed is a larger amount of co-extracted electrons in deuterium operation compared to hydrogen, limiting the amount of extracted D^- current. Thus, a higher negative deuterium current could be extracted by using an increased extraction voltage or using an increased power for plasma generation when reducing the amount of co-extracted electrons.

Special care is taken for the reduction of the amount of co-extracted electrons: the plasma production region is separated from the conversion grid by an expansion chamber with a magnetic filter field applied, resulting in a reduction of the electron density and temperature by one order of magnitude each. The reduction of the electron temperature is also required to minimize the destruction of surface-produced negative hydrogen ions due to electron stripping. In addition, a positive bias of the conversion grid in respect to the source wall reduces the amount of co-extracted electrons, too.

Thus, the most important physics of such an ion source takes place in the region close to the conversion grid – this plasma volume downstream of the filter field in front of the conversion grid is called (extended) boundary layer: the production of negative hydrogen ions, their transport through the plasma as well as their extraction takes place here. The transition from a classical electron–positive-ion plasma to an ion–ion plasma (with negative hydrogen ions being the dominant negatively charged particles) within this layer creates unique plasma conditions.

Gaining a deeper insight into the dynamics within the extended boundary layer is desirable for the following reasons: on the one hand, in order to achieve a stable long-term operation; in particular the high chemical reactivity of Cs in combination with plasma-induced desorption processes lead to a complex Cs dynamics. On the other hand, possible future improvements of the source can be identified. In addition to the theoretical approach, where modeling of the extended boundary layer including the relevant physics may yield valuable information, an experimental approach is also mandatory – for the understanding of the important physics as well as to deliver input parameters and to benchmark modeling codes.

This deeper understanding of the plasma dynamics within the extended boundary layer can be gained by a simultaneous use of a multitude of diagnostics. The simultaneous use is required, since – although the prototype source is capable to deliver reproducible high performance, represented by a large extracted negative hydrogen ion current in combination with a low co-extracted electron current – especially the complex Cs dynamics makes it difficult to achieve similar Cs conditions in different experimental campaigns. Multiple diagnostics are required in order to determine a wide set of parameters: the basic plasma parameters – plasma potential, positive ion density and electron temperature – are locally measured by Langmuir probes. The determination of the Cs and H^- density (measured line-of-sight integrated via tunable diode laser absorption and cavity ring-down spectroscopy) in the extended boundary layer is of particular interest. This enables to make statements regarding the fluxes of caesium, H^- and electrons, and possible links to the performance of the source can be found, at which the electron density is represented as the difference between the positive ion density and the H^- density due to the quasi-neutrality of the plasma.

The aim of this work is to improve the understanding of the Cs dynamics within the source as well as to deliver a detailed experimental characterization of the extended boundary layer, especially related to the difference between hydrogen and deuterium operation in comparison to the source performance.

2 H⁻ sources for plasma heating and current drive of fusion devices

The most promising concepts of fusion devices for power generation are based on magnetic confinement: while a plasma is confined by a magnetic field, it can be heated up to a temperature (100 mio. K), where the fusion process $^2\mathrm{D} + {}^3\mathrm{T} \longrightarrow {}^4\mathrm{He}(3.5\ \mathrm{MeV}) + \mathrm{n}(14.1\ \mathrm{MeV})$ starts taking place in sufficient amount [1]. A toroidal device with a combination of a toroidal and a poloidal magnetic field can achieve a stable plasma confinement [2]. Two different concepts exist for the magnetic confinement: whereas stellarators create the required magnetic field solely by usage of complex external magnetic field coils, the magnetic field in tokamaks is created by a combination of external field coils and a toroidal current inside the plasma.

A sketch of the magnetic field coils and the resulting field lines of a tokamak device is shown in figure 2.1: the poloidal magnetic field $\vec{B}_\mathrm{p}$ is created by a toroidal current I_p in the plasma, whereas the toroidal magnetic field $\vec{B}_\mathrm{t}$ is created by external toroidal field coils. The easiest way to create the toroidal current is by usage of the inductive transformer principle: a solenoid is placed in the center of the torus at which a current ramp is applied. Obviously, only pulsed operation is possible by this method, since the magnetic confinement is lost after ending the current ramp. For future fusion power plants, a continuous operation – or at least pulsed operation with long (several hours) pulses with short breaks (several minutes) – are required in order to achieve cw production of electricity. For this reason, an additional mechanism for creating a toroidal current is helpful for the operation of tokamak fusion power plants.

The upcoming ITER fusion device will go into first plasma operation in 2020 [3]. Several plasma heating systems are foreseen to achieve the required temperature of 100 mio. K: heating systems based on resonant coupling of electromagnetic waves
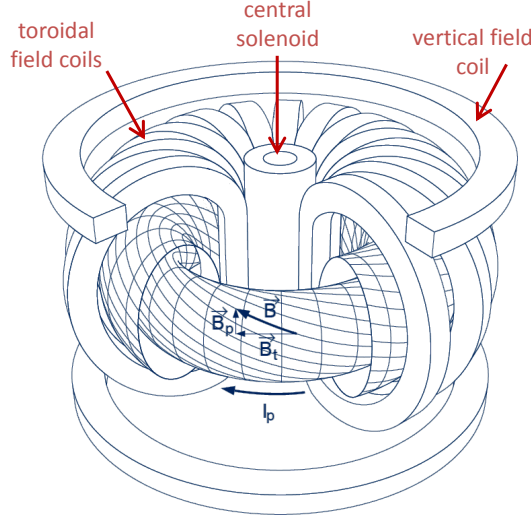
Figure 2.1: *Sketch of the main magnetic field coils of a tokamak fusion device with the resulting magnetic field structure: external toroidal magnetic field coils create a toroidal field $\vec{B}_\mathrm{t}$, whereas a central solenoid induces a toroidal electrical current I_p, resulting in a poloidal magnetic field $\vec{B}_\mathrm{p}$. Vertical field coils control the plasma positioning and shape.*

(Electron Cyclotron Resonance Heating and Ion Cyclotron Resonance Heating) with a heating power of 20 MW each as well as a Neutral Beam Injection (NBI) system with a heating power of 33 MW [1]. NBI systems are based on the heating of the fusion plasma by injection of a beam of fast deuterium or hydrogen[4] atoms, which get confined after ionization by charge exchange or ionization collisions. The NBI system can be used for efficient drive of the toroidal current if injected tangentially [4].

The scheme of a typical NBI system is shown in figure 2.2. Positive or negative hydrogen ions are produced in an ion source, extracted, accelerated by an electric field and neutralized in a gas target by charge exchange collisions:

$$H_\mathrm{fast}^{+,-} + H_2 \longrightarrow H_\mathrm{fast} + ... \ . \tag{2.1}$$

After removing non-neutralized particles using a magnetic or alternatively electric bending field, the beam can be injected into the fusion device. A large scale vacuum pump is required to reduce the pressure in the beamline in order to avoid further collisions of beam particles with background gas. In most present

---

[4]As already mentioned, the NBI system must be capable to operate in both isotopes, deuterium and hydrogen. For simplification, only hydrogen will be mentioned in the following as long as there must be no isotope effect taken into account.
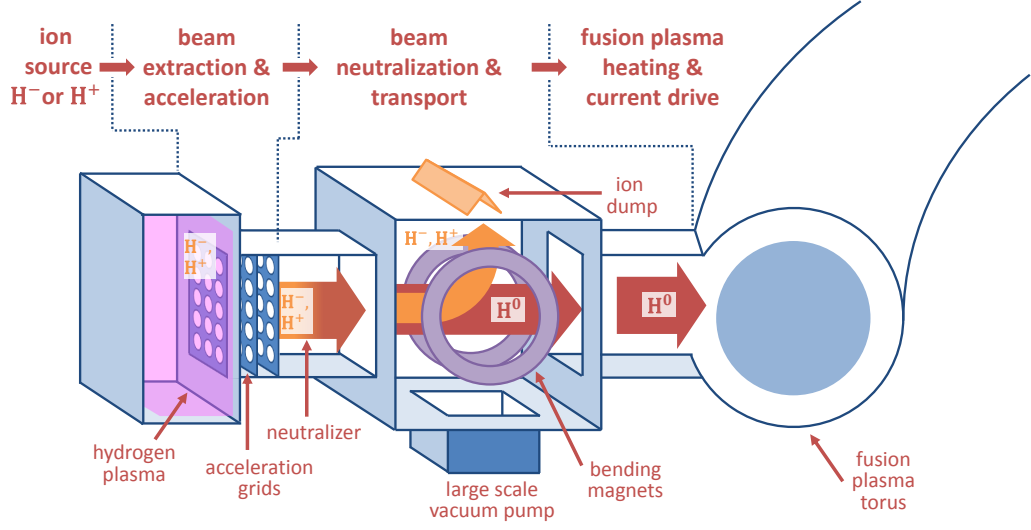
Figure 2.2: *Schematic sketch of a neutral beam injection system, consisting of an ion source for positive or negative hydrogen ions, an acceleration system, a gas neutralizer and an ion dump for non-neutralized particles.*

fusion devices, the particle energy of the NBI system is moderate (e.g. $E \leq 160$ keV at the presently largest tokamak device JET[5] [5]), and the NBI system is based on the production of positive hydrogen ions that can be easily extracted out of a hydrogen plasma.

In order to reach main power absorption of the tangentially injected neutral beam in the core of the ITER plasma, a larger particle energy of the neutral beam than in present tokamak devices in the order of several 100 keV is required [6]. However, the optimal neutralization efficiency of positive ions drops to a value below 10% at these high particle energies, as shown in figure 2.3. In contrary, the neutralization efficiency of negative hydrogen ions stays at a high level of more than 60% even at high particle energies using the optimum neutralizer size. The main reason for the high efficiency is the weakly affinity of the second electron of 0.75 eV [7]; however, the maximum neutralization efficiency is limited to 60% due the increased production of positive ions at larger neutralizer size or increasing amount of transmitted negative ions at lower size [8]. Because of the increased neutralization efficiency at the required particle energy, the NBI system for ITER has to be based on negative hydrogen ions.

However, the benefit of the weakly bound second electron for the neutralization becomes a drawback for their production, since the fragile ions are easily destroyed (the destruction mechanisms will be discussed in section 2.2). For this reason, the

---

[5]JET: Joint European Torus, Culham (UK)
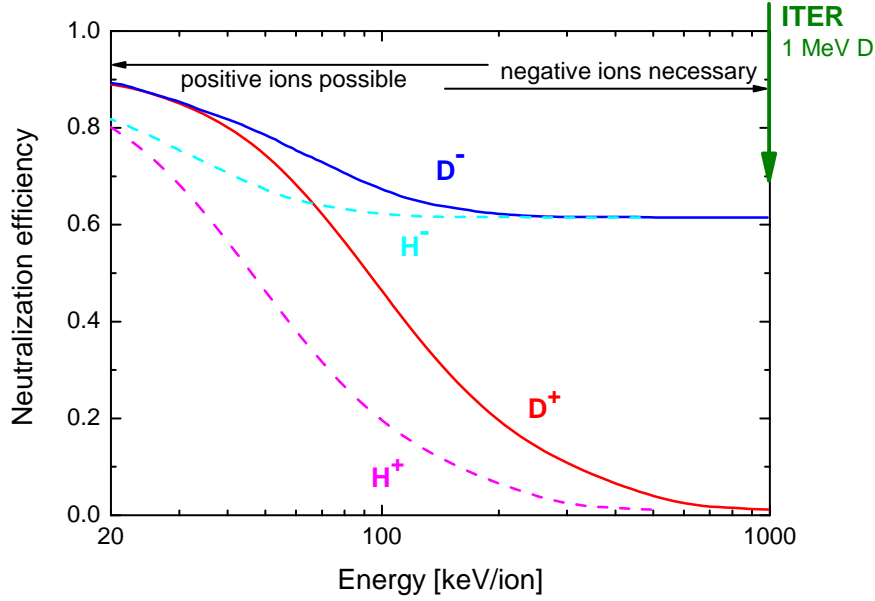
Figure 2.3: *Neutralization efficiency of positive and negative hydrogen and deuterium ions as a function of ion energy for optimum neutralizer thickness. [8]*

extracted ion current density is typically one order of magnitude smaller compared to positive hydrogen ion sources – hence, for similar particle currents, negative hydrogen ion sources must be much larger compared to positive ion sources. In order to achieve sufficient heating power, a trade-off must be taken between the particle energy and current: at ITER, the particle energy has been chosen to be 1 MeV D. The high particle energy is beneficial due to the increased current drive efficiency [6].

The requirements for the ITER Heating Neutral Beam (HNB) system are listed in table 2.1 for deuterium and hydrogen operation. Two heating beamlines with a heating power of 16.6 MW each are foreseen. 1280 extraction apertures with a diameter of 14 mm each create an extraction area of 2000 cm^2. An extracted D⁻ (H⁻) current density of 28.5 (34.5) mA/cm^2 leads to an extracted D⁻ (H⁻) current of 57 (69) A, which is required since losses due gas stripping in the accelerator (20%–30% at a source pressure of 0.3 Pa [9]), in the neutralizer (60% efficiency) and transmission losses have to be taken into account.

As will be shown in section 2.3, the production of H⁻ takes place in a low temperature plasma. When extracting negative hydrogen ions out of a plasma, electrons are co-extracted inevitably which have to be removed out of the beam prior acceleration to full energy. As will be shown in the next section, the tolerable amount of co-extracted electrons is technologically limited by the requirement

Table 2.1: *Requirements for each ITER HNB injector in deuterium (hydrogen) operation.*

	ITER
Heating power	16.6 MW
Particle energy D (H)	1 (0.87) MeV
Extraction area	2000 cm^2
Number of extraction apertures	1280
Extracted D$^-$ (H$^-$) current density	28.5 (34.5) mA/cm^2
Extracted D$^-$ (H$^-$) current	57 (69) A
Amount of co-extracted electrons	$j_\mathrm{e}/j_{\mathrm{D}^-} \leq 1$ ($j_\mathrm{e}/j_{\mathrm{H}^-} \leq 0.5$)
Source pressure	≤ 0.3 Pa
Pulse length D (H)	3600 (400) s
Beam homogeneity	$\pm$ 10%

$j_\mathrm{e}/j_{\mathrm{D}^-} < 1$. To minimize ion losses in the extraction and acceleration system by collisions with background gas particles, the particle source has to operate at a maximum pressure of 0.3 Pa. The HNB facility must deliver the neutral beam for the maximum length of an ITER pulse (3600 s D, 400 s H). The extracted beam has to be homogeneous within $\pm$10% over the full area in order to prevent damages due to unfocused beam parts.

Sources that fulfill all ITER parameters are presently not available and thus being developed. A part of the development program takes place at IPP Garching, where an R&D program has been started in the late 1990s [10]. The RF-driven IPP prototype H$^-$ source has become the ITER reference design in 2007 due to its lower demand for maintenance compared to filament sources [11].

2.1 Development towards ITER NBI

The European ITER domestic agency F4E[6] has defined an R&D roadmap in order to fulfill the development for the ITER HNB facility [12]. For this reason, several test facilities have been in operation in the past, are currently in operation or are under construction for operation in the future. A simplified time line is shown in figure 2.4. The heating neutral beam facility is expected to be ready for commissioning in 2020 at the ITER site in Cadarache (France).

---

[6]F4E: Fusion for Energy, Barcelona (Spain)
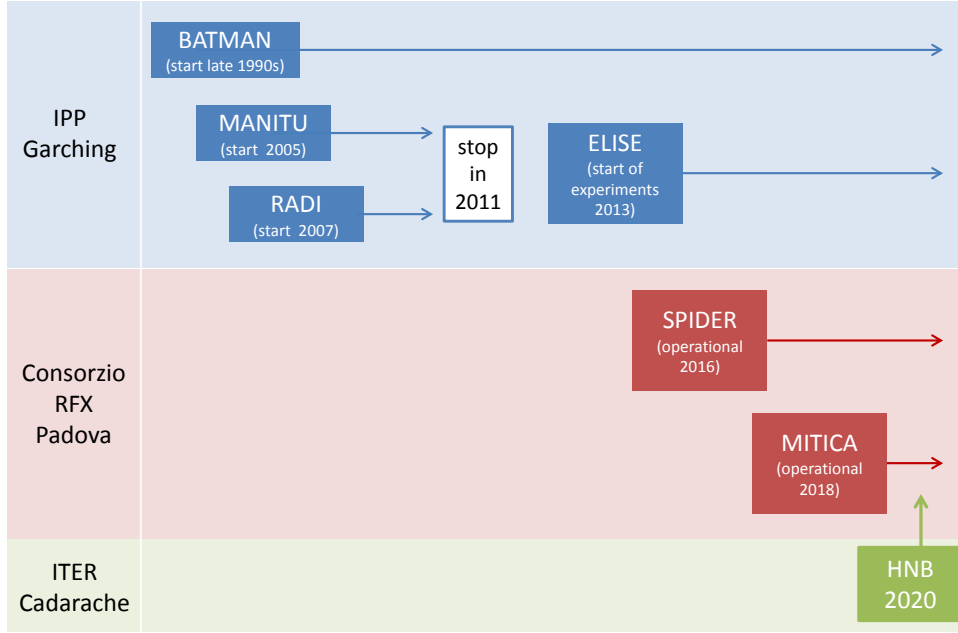
Figure 2.4: *Simplified time line of the development program towards the ITER HNB showing the individual test facilities.*

Four test facilities with two different sizes have been or are still in operation at IPP Garching – the size scaling from the IPP test facilities to the full size ITER source is shown in figure 2.5:

- **BATMAN**[7] [10], which started operation in the late 1990s, is the first test facility at IPP for the production of negative hydrogen ions. The IPP prototype ion source with a size of roughly ⅛ of the ITER source area is installed at BATMAN. Due to limitations in the high voltage (HV) supply and vacuum systems, BATMAN can only run in pulsed operation with a typical pulse duration of 6 s plasma including 4 s beam extraction and a time of ≈ 3 min between pulses. The extraction and acceleration system consists of three grids with a total high voltage of up to 22 kV. Presently, the beam is extracted out of 126 apertures with a diameter of 8 mm each, leading to an extraction area of 63 cm². The ITER requirements regarding the amount of extracted negative ion current density and co-extracted electron current density have been fulfilled at BATMAN. The test facility is still in operation and is used for research of physics aspects due to its easy and flexible access for exchange of diagnostics and components.

---

[7]BATMAN: BAvarian Test MAchine for Negative ions
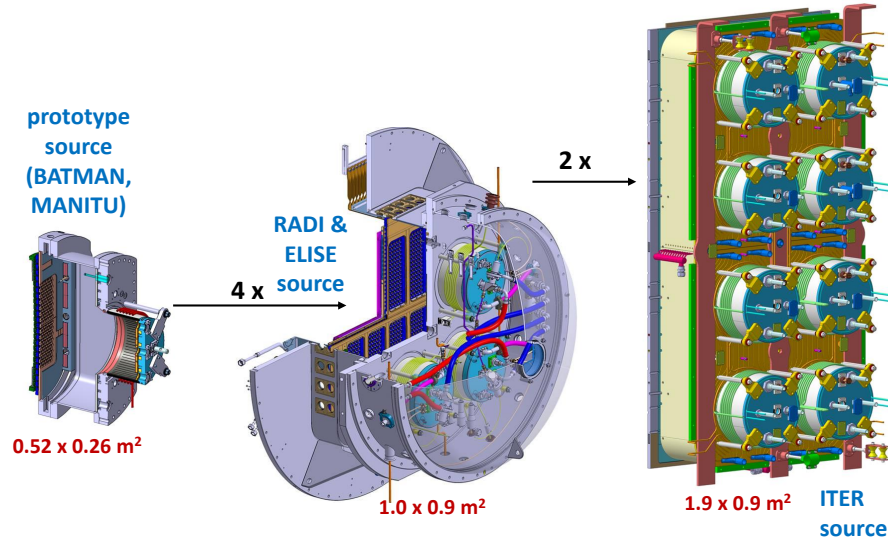
Figure 2.5: *Size scaling from the prototype source installed at BATMAN and MANITU, via RADI and ELISE towards the ITER source.*

- **MANITU**[8] [10], which was in operation 2005–2011, had the same source size as BATMAN; however, without the restriction in the pulse length. It showed the first 1 h deuterium pulse with partly fulfilling the ITER requirements [13]. During this work, the three grid extraction system consisted of 262 apertures with a diameter of 8 mm each, leading to an extraction area of 132 cm^2. Its operation has been stopped together with RADI in 2011 in favor of the construction of ELISE.

- **RADI** [14] was in operation 2007–2011 and has been a pure plasma (no beam extraction system) test facility. Its aim was demonstrating the size scalability of the plasma generation system.

- **ELISE**[9] [15] started experiments in 2013 and is equipped with a ½ ITER sized source (full width, half the height). The beam extraction system consists of three grids containing 640 apertures with a diameter of 14 mm each, leading to an extraction area of 1000 cm^2. ELISE is designed for cw operation and can thus demonstrate the required plasma pulses with a length of one hour. Due to restrictions in the available HV supply system, only pulsed extraction (10 s every 3 minutes) is possible with a total high

---

[8]MANITU: M̲ulti A̲mpere N̲egative I̲on T̲est U̲nit
[9]ELISE: E̲xtraction from a L̲arge I̲on S̲ource E̲xperiment

voltage of up to 60 kV. The main aim of ELISE is to demonstrate the size scaling as well as the feasibility of technological aspects.

The full ITER size source is under construction at Consorzio RFX, Padova (Italy) based on the design of the IPP test facilities. SPIDER[10] will be a test facility dedicated for optimizing the ion source with the possibility to use several diagnostics, whereas MITICA[11] is going to be the ITER-like NBI test facility with – for the first time – acceleration of the full-size beam to the full particle energy of 1 MeV. The extraction and acceleration system will consist of 7 grids, at which the acceleration of the ions takes place in 200 kV steps.

At all test facilities, negative high voltage is applied to the ion source during beam extraction, in which the acceleration of the beam takes place in several steps to ground potential.

2.2 Formation and destruction of negative hydrogen ions

Before the concept of the IPP prototype H⁻ source is explained in detail, the different processes for H⁻ production and destruction are shown in the following.

Formation of negative hydrogen ions

Two processes exist for the production of negative hydrogen ions in a plasma [16]:

- In the **volume process**, H⁻ is produced by dissociative attachment of slow electrons to highly vibrationally excited hydrogen molecules $H_2(\nu)$ [16, 17]:

$$H_2(\nu) + e^- (T_e \leq 1 \text{ eV}) \longrightarrow H^- + H. \qquad (2.2)$$
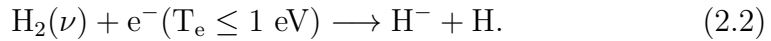
  To enhance the production yield of this process, a large electron density in the production zone as well as a large fraction of vibrationally excited hydrogen molecules with sufficient high vibrationally excitation ($\nu \geq 5$ for $H_2, \nu \geq 8$ for D_2) are required. The production of $H_2(\nu)$ usually takes place in a different plasma regime with higher electron temperature. However, this process is incompatible with the ITER requirements, in particular regarding

---

[10]SPIDER: <u>S</u>ource for <u>P</u>roduction of <u>I</u>on of <u>D</u>euterium <u>E</u>xtracted from <u>R</u>F plasma
[11]MITICA: <u>M</u>egavolt <u>ITER</u> <u>I</u>njector & <u>C</u>oncept <u>A</u>dvancement
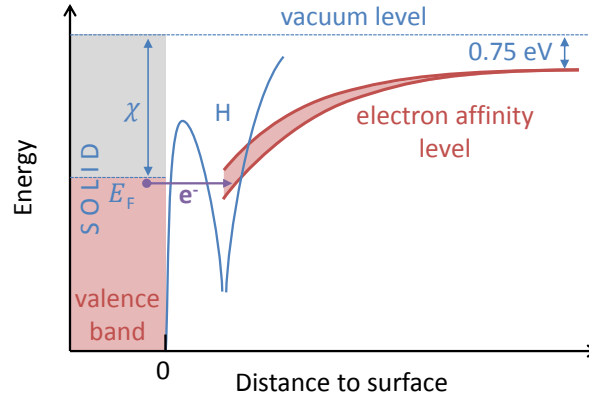
Figure 2.6: *Schematic energy diagram illustrating the lowering and broadening of the electron affinity level close to the surface, enabling the possibility of electron tunneling. E_F denotes the Fermi energy of the solid and χ its work function.*

the amount of co-extracted electrons (a high electron density is beneficial for the production of H^- by the volume process) as well as the required low source pressure.

- Negative hydrogen ions can be produced by the **surface process**. Neutral hydrogen atoms are converted on a surface to negative hydrogen ions [18]:
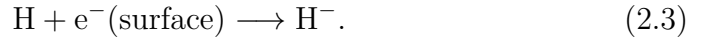
$$H + e^-(\text{surface}) \longrightarrow H^-. \tag{2.3}$$

Also the conversion of positive hydrogen ions is possible by prior neutralization:

$$H_x^+ + e^-(\text{surface}) \longrightarrow H + e^-(\text{surface}) + \ldots \longrightarrow H^-, \ x = 1, 2, 3. \tag{2.4}$$
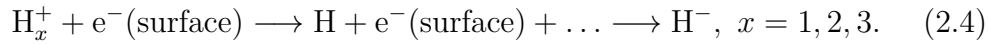
The surface conversion process is illustrated in figure 2.6: the electron affinity level of hydrogen atoms is broadened and lowered for distances close to the surface, enabling the possibility of electron tunneling from the valence band of the solid into the affinity level of H.

Obviously, the conversion yield of the surface process is strongly dependent on the work function of the surface, namely inverse on the exponential work function [19]. For this reason, Cs with a work function of 2.14 eV of bulk material [7] – the lowest work function of all stable chemical elements – is widely used for increasing the efficiency of surface production. Due to its high chemical reactivity, the convertor surface cannot be made out of bulk

Cs; thus, Cs is evaporated into the source forming layers at the metallic walls. A strong increase of the H$^-$ production in a H$^-$ source has been investigated after evaporation of Cs for the first time in the 1970s [20]. In H$^-$ sources for fusion, an increase of the extracted negative ion current by one order of magnitude is observed after evaporation of Cs.

The work function of caesiated metallic surfaces depends strongly on the thickness of the Cs layer. A low work function with a value between 1.5–1.7 eV can be obtained for a small Cs coverag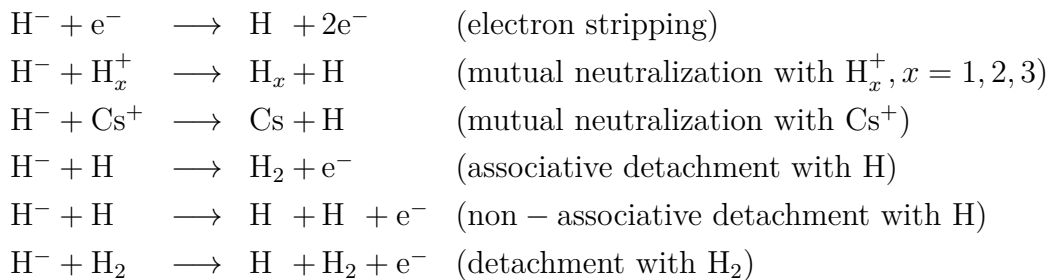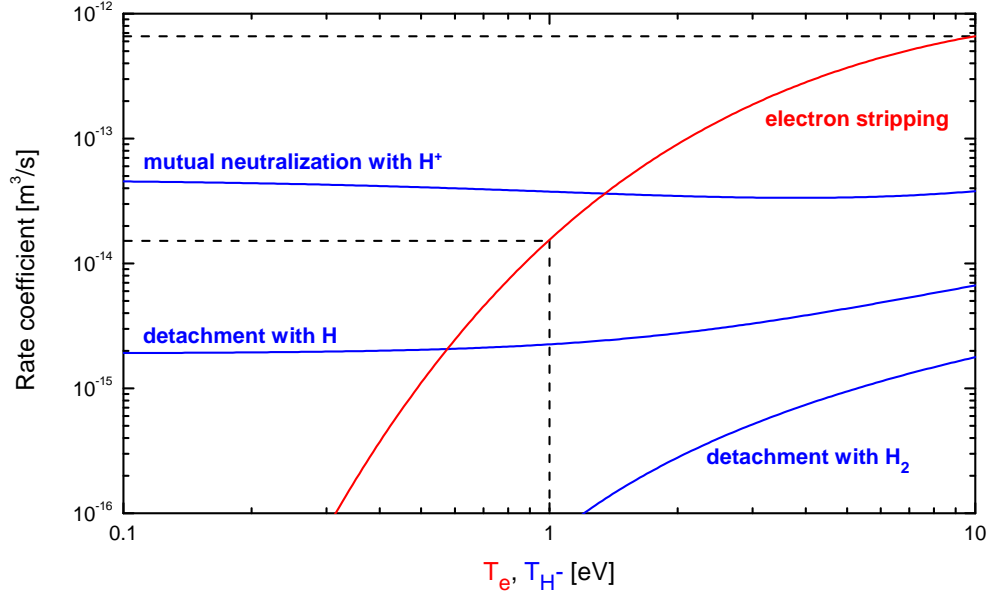e of about 0.6 mono layers (dependent on the substrate as well as on the crystal orientation) [21, 22], whereas for a Cs coverage of several mono layers or thicker the work function of bulk Cs is reached. In H$^-$ sources for fusion, a molybdenum surface is favored for caesiation, because no chemical compounds are formed with Cs as well as the self sputtering yield is low.

For the physical understanding and possible optimization of the IPP prototype ion source, knowledge about the relative importance of the two surface conversion channels out of hydrogen atoms and positive ions is of great interest. For this purpose, the particles fluxes and energy of each species at the conversion surface has to be taken into account (the conditions at the IPP prototype source will be discussed in section 2.5) as well as the conversion yield at the metallic surface, which can reach a value of up to 25% for both channels at an optimum Cs coverage, depending on the particle energy [23, 24]. The result is a dominance of H$^-$ production out of H atoms in the prototype source [25].

Destruction processes of negative hydrogen ions

Due to the weak bounding of the additional electron, H$^-$ can be easily destroyed. Several destruction processes for H$^-$ can take place in plasma or gas environment:

$$
\begin{aligned}
\text{H}^- + \text{e}^- &\longrightarrow \text{H} + 2\text{e}^- &&\text{(electron stripping)} \\
\text{H}^- + \text{H}_x^+ &\longrightarrow \text{H}_x + \text{H} &&\text{(mutual neutralization with H}_x^+, x = 1,2,3) \\
\text{H}^- + \text{Cs}^+ &\longrightarrow \text{Cs} + \text{H} &&\text{(mutual neutralization with Cs}^+) \\
\text{H}^- + \text{H} &\longrightarrow \text{H}_2 + \text{e}^- &&\text{(associative detachment with H)} \\
\text{H}^- + \text{H} &\longrightarrow \text{H} + \text{H} + \text{e}^- &&\text{(non} - \text{associative detachment with H)} \\
\text{H}^- + \text{H}_2 &\longrightarrow \text{H} + \text{H}_2 + \text{e}^- &&\text{(detachment with H}_2)
\end{aligned}
$$

Figure 2.7: *Rate coefficients for several destruction mechanism of H$^-$: electron stripping as a function of T_e ($T_{H^-} = 0.8$ eV), the other processes as a function of T_{H^-} ($T_{H^+} = T_H = 0.8$ eV, $T_{H_2} = 1400$ K). Cross sections from [26], rate coefficients computed by [27].*

The absolute number of destroyed H$^-$ particles per (m$^3 \cdot s$) of each destruction process by collision with particle species k is given by the rate

$$R_{H^-,k} = n_{H^-} \cdot n_k \cdot X_k, \tag{2.5}$$

where X_k denotes the rate coefficient of each process. These are plotted in figure 2.7. The rate coefficient for electron stripping is strongly increasing in the electron temperature range between 1–10 eV ($X_{e^-} = 2 \times 10^{-14}$ m^3 s^{-1} at $T_e = 1$ eV to $X_{e^-} = 7 \times 10^{-13}$ m^3 s^{-1} at $T_e = 10$ eV) – thus the electron stripping becomes the dominant loss mechanism at elevated electron temperatures.

Although the rate coefficient for the detachment processes with H is about one order of magnitude lower at $T_{H^-} = 0.8$ eV compared to the rate coefficient for mutual neutralization with H$^+$ or electron stripping at $T_e = 1$ eV, they become the dominant destruction processes for ion-source relevant parameters (i.e. $n_e \approx n_{H^+} \approx 10^{17}$ m^{-3}, $n_H \approx n_{H_2} \approx 10^{19}$ m^{-3}, see table 2.3). A reduction is not possible due to the requirement of H as conversion particles for the production of H$^-$.

The detachment with H$_2$, which is in the extraction system simply called stripping, limits the tolerable amount of background pressure in the acceleration

system. For this reason, the source pressure has to be below 0.3 Pa for reduction of stripping inside the accelerator. However, at such low pressure, H⁻ can only be produced efficiently by the surface process.

## 2.3 IPP prototype source for negative hydrogen ions

A drawing of the IPP prototype source for negative hydrogen ions is shown in figure 2.8 (a) as a vertical cut view, whereas (b) shows a picture of the IPP prototype source at BATMAN. The prototype RF source has been developed in the past at IPP Garching. In order to extract a sufficient high H⁻ current density at ITER relevant conditions, the source is based on the surface production of H⁻ (see section 2.2). Cs is usually continuously evaporated into the source out of a Cs oven for the formation of a stable Cs layer on the plasma grid (PG, the first grid of a three grid extraction system), at which the production and extraction of H⁻ takes place.

As explained in section 2.2, in order to avoid extensive electron stripping of H⁻, the electron temperature and density has to be low close to the plasma grid. In contrary, for the required flux of conversion particles towards the plasma grid and thus the required dissociation of hydrogen molecules a higher electron temperature is beneficial. For this reason, the plasma generation region in the driver ($T_e \approx 10$ eV, $n_e \approx 10^{18}$ m^{-3}) is separated from the H⁻ production and extraction region by an expansion chamber with a horizontal magnetic filter field applied (field strength of several mT), cooling down the plasma in temperature and density by one order of magnitude each. Subsequently, a transition takes place from an ionizing plasma in the driver (ionization processes play a major role) to a recombining plasma in front of the plasma grid (ionization processes play a minor role).

The plasma inside the driver is generated by inductive RF coupling from a water-cooled copper coil. In order to protect the ceramic driver housing from the plasma, a Faraday screen (molybdenum-coated copper cylinder mantle with axial slits) is installed.

Extraction of negative charged particles takes place at the plasma grid by applying high voltage on the three grid extraction and acceleration system, in which the source is at negative potential and the third grid at ground potential. The voltage applied between the extraction grid (second grid) and the plasma grid
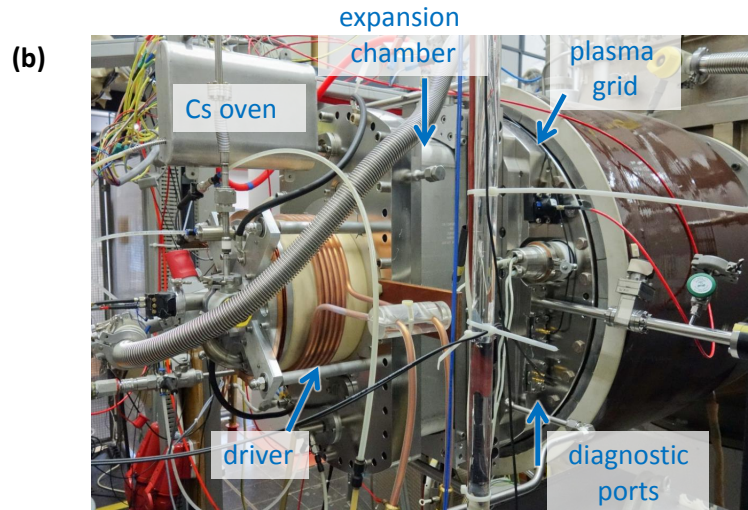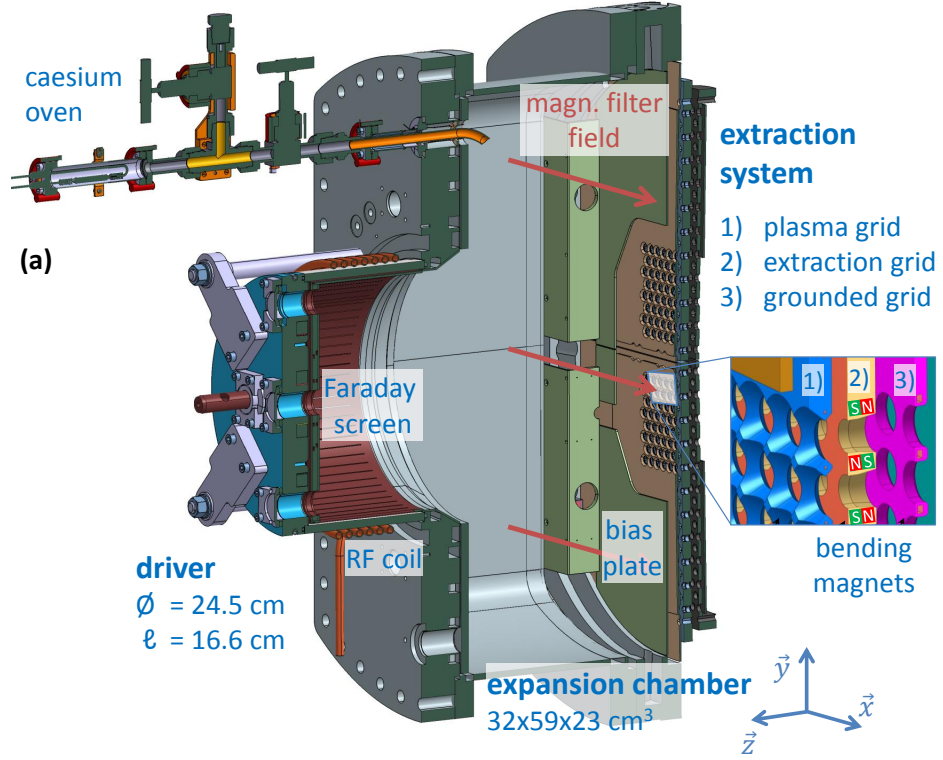
Figure 2.8: *(a): vertical cut view of the IPP prototype source, showing the driver, expansion chamber and extraction system. (b): picture of the ion source at BATMAN.*

is called extraction voltage (typically $U_{ex} = 3$–10 kV), the voltage between the grounded grid (third grid) and the extraction grid acceleration voltage (typically $U_{acc} = 10$–15 kV).

Co-extracted electrons are removed out of the extracted particle beam by usage of deflection magnets inside the extraction grid, bending the electrons onto this grid prior further acceleration. This results in a very high and local heat load on the extraction grid. The maximum allowed heat load (e.g. 32 MW/m^2 in the ELISE design) is limited by the necessarily small size of the cooling channels in the grid and the requirement of minimizing the out of plane deformation of the grid [15, 28]. For this reason, special care on the reduction of the amount of co-extracted electrons has to be taken: on the one hand, the plasma expansion in combination with the magnetic filter field reduces their amount due to the lowered electron density and temperature. In the present setup at BATMAN, the magnetic filter field is horizontally aligned and created by permanent magnets outside the source body in a flexible magnetic frame [29], which axial distance to the plasma grid can be aligned between 9 cm and 19 cm. In the standard setup of the magnetic filter field, which has not been used during this work, the axial distance of the magnets to the plasma grid is fixed at 3 cm. On the other hand, a positive bias of the plasma grid with respect to the source body also reduces the amount of co-extracted electrons [30]. A so called 'bias plate' is used in order to enlarge the source area close to the extraction apertures of the plasma grid. Although the notation 'bias plate' is rather misleading (the 'bias plate' has the same potential as the source wall), it has historically become the common notation for this cover plate.

The extraction grids at BATMAN consist presently of 126 apertures with a diameter of 0.8 cm each (large area grid LAG [10]), leading to an extraction area of 63.3 cm^2. For comparison of electron fluxes towards the plasma grid and their distribution between co-extracted electron current and the bias current, the difference between the size of the uncovered plasma grid and the extraction area has to be taken into account. The area of the uncovered plasma grid (without the extraction apertures) is 426 cm^2 and thus 6.7 times larger than the extraction area.

The parameter range of the present setup of the prototype source and extraction system at the BATMAN test facility are listed in table 2.2.

Table 2.2: *Present parameter range of the ion source and extraction system at BATMAN.*

	BATMAN
RF frequency	$\simeq 1$ MHz
RF power	< 150 kW
Plasma pulse length	$\lesssim 6$ s
Source pressure	$\gtrsim 0.3$ Pa
Total high voltage ($U_{\mathrm{ex}} + U_{\mathrm{acc}}$)	≤ 22 kV
Extraction area	63.3 cm^2

2.4 Low pressure, low temperature plasmas and sheath formation

Before explaining the working principle of the IPP prototype H$^-$ source in more detail, it is necessary to give a brief overview of the physics regarding low pressure, low temperature plasmas within this section.

A plasma is called an at least partial ionized gas exhibiting collective behavior. It consists of positive ions, negatively charged particles (usually electrons) and possibly neutral atoms or molecules. At a macroscopic scale, the plasma is quasi-neutral, meaning that the number of negative charges is equal to the number of positive charges:

$$n_{\mathrm{e}} + \sum_j Z_j n_{\mathrm{i}-,j} = \sum_k Z_k n_{\mathrm{i}+,k}, \qquad (2.6)$$

with the electron density n_{e}, the charge number Z of the particular particle species, the negative ion density $n_{\mathrm{i}-,j}$ of species j and the positive ion density $n_{\mathrm{i}+,k}$ of species k.

At low pressure (typically 0.1–1000 Pa) the mean free path of the particles is long and thus the number of collisions is limited. Since the energy transfer is weak for collisions of particles with high mass difference, electrons are then usually not in thermal equilibrium with the heavy particles (ions, atoms or molecules), but particle species with similar mass can be in thermal equilibrium in low pressure, low temperature plasmas. However, a heavy particle species must not necessarily in thermal equilibrium with an other heavy particle species if e.g. energy is gained during the dissociation process of molecules, leading to different temperatures of the molecular and dissociated species (the conditions in the prototype ion source will be discussed in section 2.5). The effect of differing electron and heavy particle

temperature is enhanced since most plasma heating mechanism transfer energy mainly to electrons. The resulting temperatures in low-temperature plasmas are then some eV for electrons[12], whereas the heavy particle temperature is usually far below 1 eV.

Sheath formation

Low pressure plasmas are enclosed in a vacuum vessel. Close to the wall a sheath is formed. The reason for the formation of the plasma sheath is explained in the following:

Consider a classical plasma, where electrons are the dominant negatively charged particle species. When comparing particle fluxes of electrons and positive ions towards the wall (particle flux $\Gamma = nv_z$, with v_z denoting the particle speed component towards the wall), the flux of electrons is much higher due to their lower mass and higher temperature – the mean speed of Maxwellian distributed particles with temperature T and mass m is $\bar{v} = \left(8k_\mathrm{B}T/\pi m\right)^{1/2}$, k_B denoting the Boltzmann constant. The different charge fluxes lead to a potential shift between the plasma and the wall: the potential of the wall is lowered leading to a reduced electron flux towards the wall, whereas positive ions are accelerated onto the wall. A steady state is reached at a potential difference with equal charge fluxes impinging the wall, in this case the particle fluxes are called ambipolar. Since the potential of the walls of the plasma experiment is often set as the ground potential (= 0 V), this results in a positive value of the potential of the bulk plasma Φ_pl. Quasi-neutrality does then no longer hold in the plasma sheath: the electron density is decreased stronger compared to the positive ion density towards the wall.

The dependencies of the positive ion and electron densities as well as of the potential as a function of the distance to the wall are shown in figure 2.9: a pre-sheath establishes between the bulk plasma and the sheath. The formation of the pre-sheath is required for stability reasons of the sheath. A small potential drop within the pre-sheath (small compared to the drop in the sheath) accelerates positive ions to its speed of sound towards the sheath [2]. Quasi-neutrality of the plasma holds up to the sheath edge, whereas equal positive and negative charge fluxes are formed at the wall. Most part of the potential drop between the plasma and the wall happens in the sheath.

---

[12]1 eV $\simeq$ 11605 K
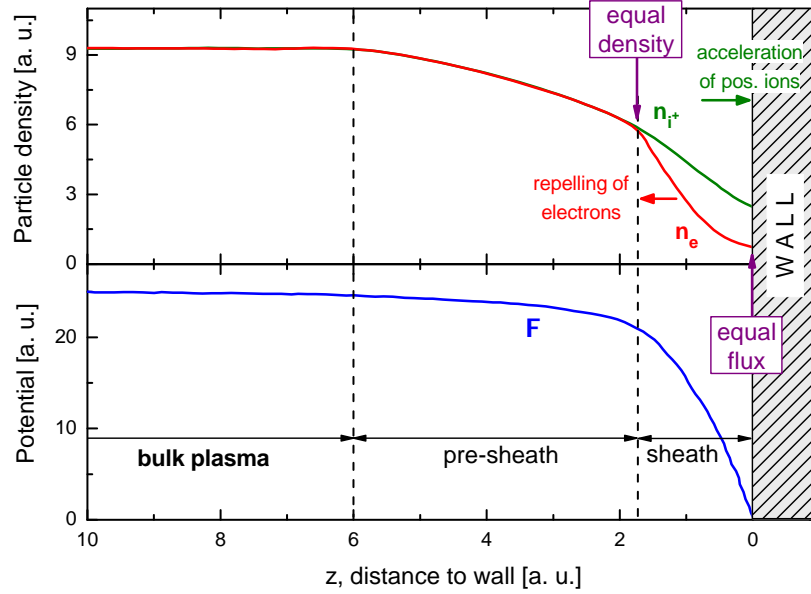
Figure 2.9: *Particle densities and potential in the plasma sheath close to a wall.* *[31]*

It should be mentioned that in a plasma experiment enclosed by metallic walls, only the global flux balance integrated over the whole surface must be ambipolar. In contrary, local fluxes can be non-ambipolar, because compensating currents can flow through the metallic walls. This is in particular the case in the prototype source: due to a high variation of the electron temperature along the magnetic filter field, the local flux balance towards the wall is shifted to electrons in the driver and to positive ions close to the plasma grid.

A characteristic length of a plasma is the Debye length λ_{D}. The Debye length defines the length at which the potential of an additional test charge drops to a value of 1/e due to shielding with plasma particles. As a consequence, the quasi-neutrality of the plasma can only be disturbed within the length of several λ_{D}, leading to the typical thickness of the plasma sheath. The Debye length for electrons is given by

$$\lambda_{\mathrm{De}} = \sqrt{\frac{\epsilon_0 k_{\mathrm{B}} T_{\mathrm{e}}}{n_{\mathrm{e}} e^2}}, \tag{2.7}$$

with ϵ_0 denoting the vacuum permittivity, T_{e} the electron temperature and e the elementary charge. Considering parameters of the negative hydrogen ion source ($n_{\mathrm{e}} = (1 \times 10^{17} – 1 \times 10^{18})$ m^{-3}, $T_{\mathrm{e}} = 1–10$ eV), results in a Debye length in the order of 10 μm – so the thickness of the plasma sheath is well beyond 1 mm inside the ion source and for that reason not accessible by diagnostics.

Influence of negative ions

Firstly, the influence of negative ions in the plasma volume on the plasma sheath is considered. Due to their higher mass, the flux of negatively charged particles towards the wall is reduced. Thus, the plasma potential is decreased. If the electron temperature is higher compared to negative ions $T_e > T_{i-}$, the flux of negative charged particles hitting the wall consists almost only of electrons whereas negative ions are confined by the electric field in the plasma sheath. The Debye length is reduced to a value of [32]

$$\lambda_D^* = \lambda_{De} \sqrt{\frac{1}{1 + \frac{T_e n_{i-}}{T_{i-} n_e}}}.$$

(2.8)

Thus, the influence of negative ions on the Debye length only becomes significant for $n_{i-} \gg n_e$.

The conditions in the sheath are more complicated for surface produced H⁻ ions, since not only the fluxes of plasma particles from the volume towards the surface, but also the flux of H⁻ from the surface towards the plasma volume has to be taken into account. A PIC code modeling the plasma sheath for IPP prototype ion source conditions has been developed in the past [25]. The potential in the sheath close to the plasma grid as well as the electron and ion densities (considered are e, H⁻, H⁺ and Cs⁺) as a function of the distance from the PG is shown in figure 2.10: whereas the positive ion densities as well as the electron density are decreased in a similar way as in a classical sheath (compare to figure 2.9), the H⁻ density is increased towards the plasma grid. The increase is caused due to the surface production of H⁻ and their subsequent acceleration in the sheath potential towards the bulk plasma. In addition, the code revealed that due to the dominant surface production of H⁻ out of neutral H atoms, a potential minimum can be formed in the sheath close to the wall because of the presence of too many negative charges whose compensation is no longer possible by the limited amount of positive ions. This minimum hinders the transport of surface-produced H⁻ towards the plasma and leads to a space-charge limited emission of H⁻ from the surface into the plasma. In this case, the flux of H⁻ ions into the plasma is no longer dependent on the flux of H atoms towards the surface.

Consequently, the amount of negative hydrogen ions penetrating through the sheath can only be increased by a decrease of the surface work function or an increase of the flux of conversion particles towards the surface, as long as no space
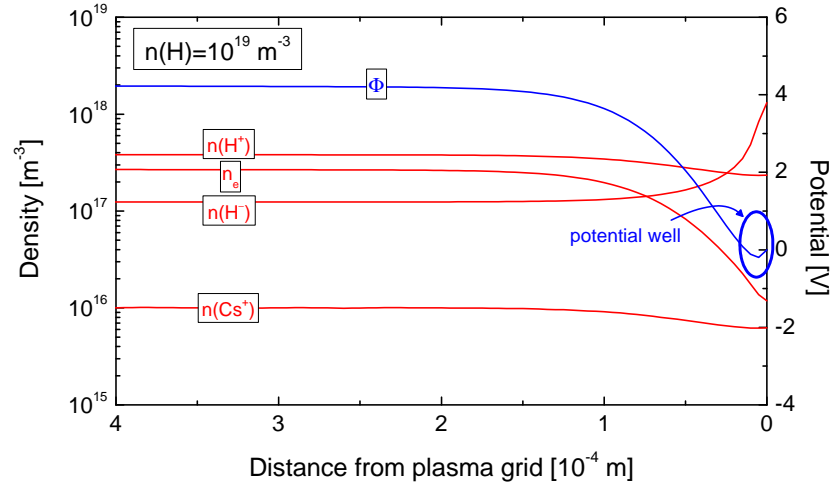
Figure 2.10: *Particle densities and the potential in the sheath close to the plasma grid at IPP prototype source conditions, including surface production of H⁻. [25]*

charge limitation occurs. In case of the latter, a further increase is only possible by an increase of the positive ion density.

2.5 Extended boundary layer

The region in the downstream side of the magnetic filter field, in front of the plasma grid with a thickness of some cm, is called extended boundary layer. The most important physics of an ion source – production of H⁻, their transport and extraction – takes place here. The layer is limited in axial direction by the magnetic filter field: H⁻ can only be present in the plasma in a significant amount at the lowered electron temperature and density, where its survival length becomes several cm [33].

Magnetic field topology and particle magnetization

The magnetic field inside the prototype ion source influences the transport of charged particles in the expansion chamber. As shown in figure 2.11 (a), the total magnetic field topology inside the extended boundary layer consists of the magnetic filter field as well as of the magnetic deflection field at axial distances below 1 cm to the plasma grid. Both fields are created by permanent magnets in the prototype source. In the setup used during this work, the magnetic filter field magnets were positioned in a frame with a distance of 9 cm in front of the plasma grid and its maximum horizontal flux density $|B_x|$ in the horizontal
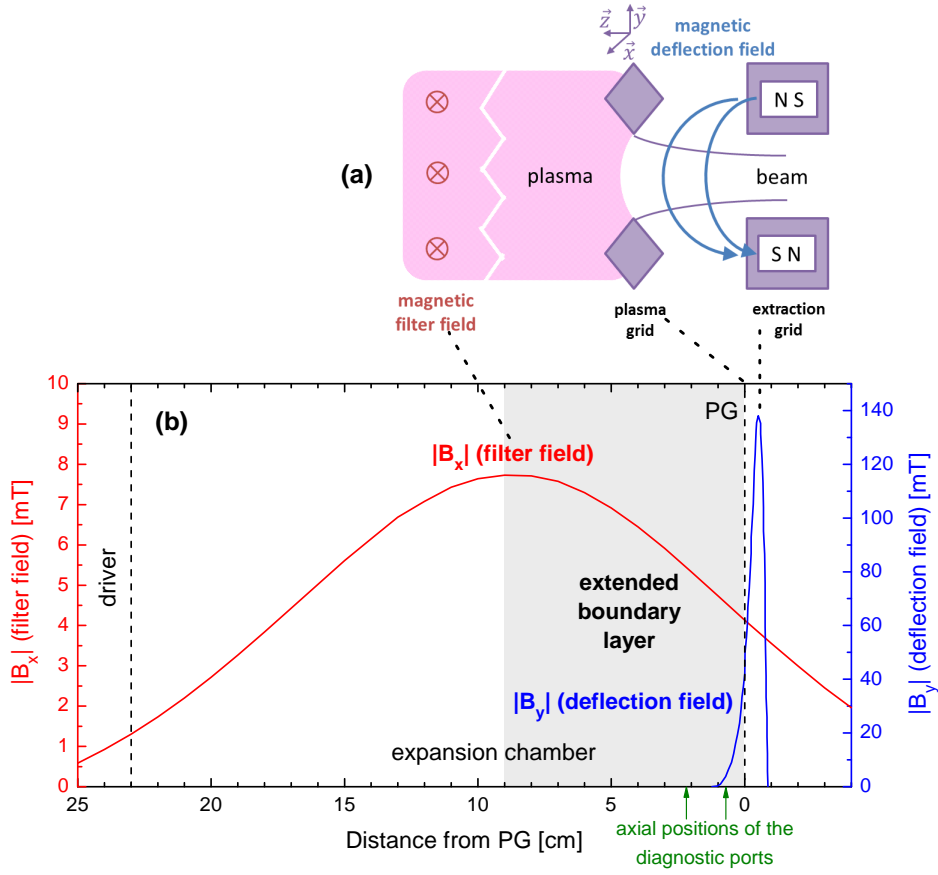
Figure 2.11: *(a): topology of the magnetic fields close to the plasma grid. (b): magnetic flux density of the filter field $|B_x|$ in the horizontal center as well as $|B_y|$ for the electron deflection field in the axial center of an extraction aperture as a function of the axial distance to the plasma grid.*

center of the source is about 8 mT. The deflection field is created by permanent magnets inside the extraction grid with alternating polarity. Thus, the axial drop of the field strength is much stronger for the deflection field, as shown in figure 2.11 (b), where the horizontal magnetic flux density $|B_x|$ of the filter field and the vertical magnetic flux density $|B_y|$ of the deflection field is plotted for varying axial distance to the plasma grid. At axial distances closer than 5 mm to the PG, $|B_y|$ of the deflection field is larger than $|B_x|$ of the filter field, resulting in a complex 3D structure of the magnetic field close to the PG.

For the discussion of particle fluxes inside the extended boundary layer, it has to be considered which particle species is magnetized. Magnetization occurs if two conditions are fulfilled:

1. The particle gyration (Larmor) radius r_L needs to be much smaller than the typical dimension of the chamber d_{source}:

$$r_L = \frac{\sqrt{2mk_BT}}{|q|B} \ll d_{source}. \tag{2.9}$$

Using parameters inside the extended boundary layer ($T_e = 1$ eV, $T_{H^+} = 0.8$ eV, $B_x = 8$ mT) yields:

$$r_{L,e^-} = 0.42 \text{ mm}, \ r_{L,H^+} = 16 \text{ mm}. \tag{2.10}$$

Thus, with a typical source dimension d_{source} of several 10 cm, condition 2.9 is well fulfilled by electrons, however only weakly fulfilled by protons.

2. The gyration frequency f_L needs to be larger compared to the collision frequency ν_{col} for the particle gyration around a magnetic field line:

$$f_L = \frac{|q|B}{2\pi m} > \nu_{col}. \tag{2.11}$$

At conditions in the expansion volume, the collision frequency is in the same order of magnitude for electrons and protons ($\approx 10^7$ Hz) [27] – coulomb collisions as well as elastic collisions with H and H_2 have been taken into account in the calculation. Because collisions of particles with the same mass do not lead to a net transport in the filter field [34], they are not included. Also inelastic collisions with H and H_2 are not taken into account due to their much lower cross section compared to elastic collisions.

However, the gyration frequency is in the order of 10^8 Hz for electrons and in the order of 10^5 Hz for protons. Thus, the condition (2.11) is fulfilled only by electrons and not by protons.

In total, only electrons are magnetized within the expansion chamber.

Plasma dynamics

A schematic view of the main particle fluxes within the source is shown in figure 2.12: from the driver side, a plasma flux consisting of electrons, positive ions (H^+, H_2^+, H_3^+, Cs^+) and neutral atoms and molecules (H, H_2, Cs) reaches the extended boundary layer. In contrary to the heavy positive ions, which are not
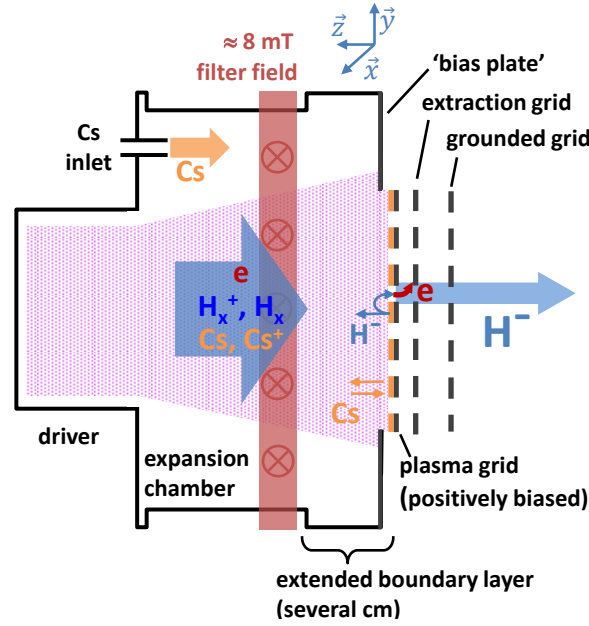
Figure 2.12: *Schematic vertical cut view of the plasma dynamics within the prototype source.*

magnetized and therefore their transport is not hindered by the magnetic filter field, electrons are magnetized. Thus, the electrons gyrate along the magnetic field lines and can only diffuse through the magnetic filter field by collisions [34]. For this reason, the velocity component towards the plasma grid is strongly decreased; the increased number of collisions with other plasma particles results in a reduction of the electron temperature [35].

Negative hydrogen ions are predominantly produced by the surface process: the H⁻ density in the extended boundary layer is increased by one order of magnitude during the caesiation process from 10^{16} m⁻³ to 10^{17} m⁻³, so volume production contributes only by 10% to the negative ions close to the plasma grid in a well conditioned source.

In front of the extraction apertures, a distinct boundary is formed which separates the extracted particle beam of negatively charged particles with the quasi-neutral plasma. Whereas at the plasma side no strong electrical fields can occur, a strong electrical field due to the high applied extraction voltage is formed at the beam side. Because of its distinct shape of a concave plasma boundary, this boundary is called meniscus. Negative particles penetrating through the meniscus are strongly accelerated and thus extracted out of the plasma. A schematic sketch of the boundary between the plasma and the extracted beam is shown in figure 2.13.
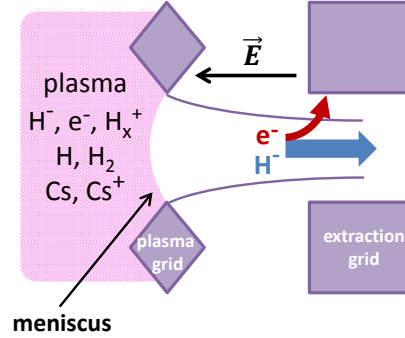
Figure 2.13: *Sketch of the boundary between the plasma and the extracted particle beam.*

As shown in the figure, the aperture collars in the plasma grid are chamfered. It has been first empirically seen that chamfering the plasma grid apertures yields an increase of the extracted negative hydrogen ion density [10]. When leaving the plasma grid, H$^-$ ions have a velocity component towards the driver, so a bending mechanism is necessary in order to extract H$^-$. A 3D negative ion trajectory calculation has been carried out in the past [33], showing that the main bending mechanism is bending by the magnetic field of the electron deflection magnets as well as due to charge exchange collisions. The extraction probability of an surface produced H$^-$ ion is increased for chamfered aperture collars due to a more beneficial starting angle.

The produced H$^-$ particles at the plasma grid repel electrons from the expanding plasma in order to sustain the required quasi-neutrality of the plasma within the extended boundary layer. However, H$^-$ particles can not penetrate through the magnetic filter towards the driver in significant amount due to the increasing destruction probability at increased electron temperature and density. This leads to a unique transition: at the driver side there is a classical hydrogen plasma produced, which dominant negatively charged particle species are electrons. However, close to the plasma grid an ion–ion plasma can be formed in the extended boundary layer, with H$^-$ becoming the dominant negatively charged particle species. The necessity of this condition – especially regarding the required low amount of co-extracted electrons – can be seen by a simple and rough estimation, where the extracted particle current densities j_{H^-}, j_e are calculated out of their flux at the edge of a homogeneous plasma with densities n_{H^-}, n_e (limiting space charge

effects are not taken into account):

$$j_{\mathrm{H}^-,\mathrm{e}} = n_{\mathrm{H}^-,\mathrm{e}} e \bar{v}_{z>0}, \tag{2.12}$$

$\bar{v}_{z>0}$ denoting the mean particle velocity towards the extraction boundary. Integration of the Maxwell–Boltzmann distribution yields (a derivation can be found e.g. in [2]):

$$\bar{v}_{z>0} = \frac{1}{4}\bar{v} = \frac{1}{4}\sqrt{\frac{8k_{\mathrm{B}}T}{\pi m}}. \tag{2.13}$$

Using the required parameters of the ITER source and typical parameters inside the extended boundary layer ($j_{\mathrm{D}^-} = j_{\mathrm{e}} = 28.5\ \mathrm{mA/cm^2}$, $T_{\mathrm{D}^-} = 0.8$ eV, $T_{\mathrm{e}} = 1$ eV), the particle densities at the plasma boundary become

$$n_{\mathrm{D}^-} = 7 \times 10^{17}\ \mathrm{m}^{-3},\ n_{\mathrm{e}} = 1 \times 10^{16}\ \mathrm{m}^{-3}. \tag{2.14}$$

The main reason for the large difference is the mass difference $\sqrt{m_{\mathrm{D}^-}/m_{\mathrm{e}}} \approx 61$. Already this rough estimation clearly shows that the electron density in front of the plasma grid is a critical parameter:

In order to suppress the amount of co-extracted electrons to a tolerable level, their density needs to be almost two orders of magnitude lower compared to the H⁻ density. Hence, especially the amount of co-extracted electrons is expected to react very sensitive on the composition of the plasma in front of the plasma grid, and therefore on the magnetic filter field strength and topology, the potential characteristics in the sheath close to the plasma grid and thus on the bias.

However, it must be mentioned that this rough approximation is only valid for isotropic particle fluxes. Especially the hindered transport of the magnetized electrons in axial direction relaxes the condition (2.14).

Plasma drift and sheath dependence on the bias

The plasma in front of the plasma grid is not symmetric along the vertical axis in front of the plasma grid inside the prototype ion source. The asymmetry appears for instance in the positive ion density [36] and the H$_\beta$ Balmer line emission [29]. The non-uniformity is generated by drifts in the plasma caused by the magnetic filter field with flux density $\vec{B}$. A force $\vec{F}$ perpendicular to a magnetic field leads
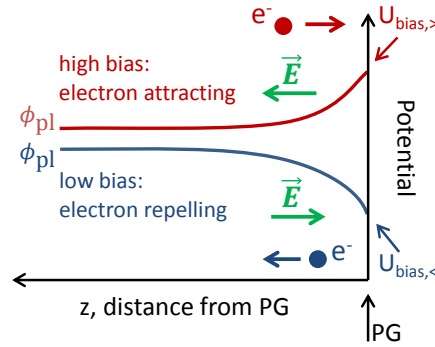
Figure 2.14: *Sketch of the potential profile close to the plasma grid for high and low applied bias voltage.*

to a drift of magnetized charged particles with the drift velocity

$$\vec{v}_\mathrm{D} = \frac{\vec{F} \times \vec{B}}{qB^2}, \tag{2.15}$$

q denoting the electric charge of the particle. Since only electrons are magnetized in the prototype ion source, only these particles can cause drifts. However, due to the required quasi-neutrality of the plasma, the resulting drift is ambipolar. The exact composition of the total drift inside the prototype ion source is not yet understood and still an open question. However, the following conclusions can be drawn out of experimental observations: firstly, the plasma is symmetric without applying the magnetic filter field. By change of the magnetic filter field direction, the vertical off-center asymmetry changes symmetrically (in the following named as 'drift up' and 'drift down' case) – for this reason, the asymmetry must be caused by plasma drifts. Secondly, the $\vec{E} \times \vec{B}$ drift – which is caused by the electric force $\vec{F} = q\vec{E}$ – plays an import role, since the plasma homogeneity can be changed by variation of the PG bias voltage, the latter influencing the plasma potential and in this way the axial electric field inside the source.

The bias voltage does not only influence the plasma symmetry by causing drifts, but it also has an effect on the particle fluxes towards the plasma grid inside the extended boundary layer. A sketch of this effect is shown in figure 2.14: without biasing or when applying a low bias voltage, a classical electron repelling sheath is formed, resulting in $U_\mathrm{bias} < \Phi_\mathrm{pl}$. Increasing the bias voltage results in the transition towards an electron attracting sheath – at a high bias voltage applied $U_\mathrm{bias} > \Phi_\mathrm{pl}$, the potential is increased from the bulk plasma towards the plasma grid and electrons are therefore attracted towards the wall. However, one has to

Table 2.3: *Plasma parameters in the extended boundary layer of the IPP prototype source for typical operational parameters.*

Parameter	Value
n_{i+}	$0.5\text{--}5 \times 10^{17}$ m^{-3}
n_{H^-}	$0.1\text{--}1.5 \times 10^{17}$ m^{-3}
$n_e = n_{i+} - n_{H^-}$	$\lesssim 5 \times 10^{17}$ m^{-3}
n_{H_2}	2×10^{19} m^{-3}
n_H/n_{H_2}	$0.2\text{--}0.4$
n_{Cs^0}	$0.5\text{--}2 \times 10^{15}$ m^{-3}
T_e	1 eV
T_{H_2}	0.1 eV
$T_H = T_{H^+} = T_{H^-}$	0.8 eV
$n_{H^+} : n_{H_2^+} : n_{H_3^+}$	$1 : 1 : 0.5$

take into account that the applied bias also influences the plasma potential in the bulk plasma in front of the grid, since the latter is disturbed due to the large area of the biased plasma grid and the subsequently large bias currents flowing to the plasma grid (several amperes).

The physical parameter describing the potential profile in the sheath and in this way the particle fluxes towards the plasma grid is the difference between the applied bias voltage and the plasma potential $U_{bias} - \Phi_{pl}$ [37]. At the typically applied bias voltage, the potential drop in the sheath is close to 0 V ($U_{bias} - \Phi_{pl} \approx 0$ V). As will be shown in chapter 5, the amount of co-extracted electrons is reduced to its minimum at this setting, whereas the extracted H⁻ current is not influenced significantly.

Plasma parameters and resulting particle fluxes

Typical plasma parameters in the extended boundary layer in front of the plasma grid, which have been determined in individual measurement campaigns at the prototype ion source, are listed in table 2.3.

The positive ion density n_{i+} as well as the electron temperature T_e have been determined by Langmuir probe measurements [38]. Measurements of the negative hydrogen ion densities have been carried out using cavity ring-down spectroscopy [39] as well as using laser photodetachment [37]. The neutral Cs density n_{Cs^0} is determined by means of Cs absorption spectroscopy [40]. The fraction of dissociated hydrogen atoms n_H/n_{H_2} as well as the H$_2$ temperature T_{H_2}, which is equal to the gas temperature, is determined by optical emission spectroscopy [41].

The temperature of hydrogen atoms and protons $T_{\mathrm{H}}, T_{\mathrm{H^+}}$ is higher than $T_{\mathrm{H_2}}$, since they gain energy during the dissociation process by dissociative excitation into the repulsive state. Subsequent collisions lead to a temperature of 0.8 eV [42].

Not exactly known is the temperature of the negative hydrogen ions $T_{\mathrm{H^-}}$. For volume-produced H$^-$ particles, a temperature similar to hydrogen atoms or protons is expected. In contrast, surface produced H$^-$ can gain energy in the sheath of some eV, depending on the bias (as discussed above). As will be shown in the results, the energy gain in the sheath is not higher than 2–3 eV, and for typically operational bias parameters close to 0 eV. Positive ions can gain or loose the same amount of energy in the sheath prior conversion. A certain amount of the particle energy can be lost by an inelastic reflection at the wall [43]. For the temperature of H$^-$ in the extended boundary layer, also the high importance of charge exchange collisions (H$^-$ + H $\longrightarrow$ H + H$^-$) for the H$^-$ trajectories have to be taken into account [33]. For these reasons, $T_{\mathrm{H^-}}$ is assumed to be $T_{\mathrm{H^-}} = T_{\mathrm{H}} = T_{\mathrm{H^+}} = 0.8$ eV.

For the distribution of the different species of positive ions of hydrogen – H$^+$, H$_2^+$, H$_3^+$ – a fraction of 40%, 40% and 20% is assumed. These values are based on extrapolation of the source pressure and RF power of measurements of the particle distribution in a positive hydrogen ion source [44].

Simultaneous determination of relevant plasma parameters is of high importance for the investigation of correlations with the extracted current densities in hydrogen and deuterium operation. For this reason, one aim of this work is the simultaneous measurement of $n_{\mathrm{i^+}}, n_{\mathrm{H^-}}, n_{\mathrm{Cs^0}}, T_{\mathrm{e}}$ in the extended boundary layer, using the diagnostics described in chapter 3, in order to determine correlations between particle fluxes in the extended boundary layer with the source performance:

$$
\begin{array}{rcccl}
\Gamma_{\mathrm{Cs_0}} \text{ towards PG} & \longleftarrow & n_{\mathrm{Cs^0}} & \overset{?}{\longleftrightarrow} & j_{\mathrm{H^-}}, j_{\mathrm{e}} \\
\Gamma_{\mathrm{H^-}} \text{ from PG} & \longrightarrow & n_{\mathrm{H^-}} & \overset{?}{\longleftrightarrow} & j_{\mathrm{H^-}} \\
\Gamma_{\mathrm{e}} \text{ towards PG} & \longleftarrow & n_{\mathrm{e}} = n_{\mathrm{i^+}} - n_{\mathrm{H^-}} & \overset{?}{\longleftrightarrow} & j_{\mathrm{e}}
\end{array}
$$

The flux of Cs^0 towards the PG correlates with $n_{\mathrm{Cs^0}}$ because Cs^0 shows an isotropic velocity distribution in the extended boundary layer what is prooved by the Doppler-broadened absorption spectra, which will be shown in section 3.1. The negative hydrogen ion density in front of the PG is dominated by the surface production, and thus correlated to the flux of H$^-$ from the PG. The flux of electrons towards the PG depends on n_{e} in the extended boundary layer; however, the reduced flux due to the magnetization has to be taken into account.

Table 2.4: *Particle fluxes in one direction in space in the extended boundary layer of the IPP prototype source using plasma parameters from table 2.3 and an isotropic distribution.*

| Particle species	Flux Γ [m^{-2}s^{-1}]
H	$1\text{--}3 \times 10^{22}$
H$^+$	$0.7\text{--}7 \times 10^{20}$
H$^-$	$0.3\text{--}5 \times 10^{20}$
e$^-$	$\lesssim 8 \times 10^{22}$
Cs^0	$0.5\text{--}2 \times 10^{17}$

Possible correlations with the source performance can help to identify the difference between hydrogen and deuterium operation – a higher co-extracted electron current density in combination with an almost identical or slightly reduced extracted negative ion current density regularly appears in deuterium compared to hydrogen operation; this higher amount of co-extracted electrons often limits the source performance in deuterium operation. In addition, a possible correlation of the source performance with the neutral Cs density could help in order to determine the optimum amount of the Cs evaporation rate.

The particle fluxes in one spatial direction ($\Gamma_i = \frac{1}{4} n_i \bar{v}_i$) are listed in table 2.4 for the particle species H, H$^+$, H$^-$, e$^-$ and Cs^0 using the parameters in the extended boundary layer listed in table 2.3. The flux of hydrogen atoms towards the plasma grid is more than one order of magnitude larger compared to the flux of protons, resulting in the already discussed dominance of the conversion of atomic hydrogen to negative ions. The flux of Cs^0, which is required to sustain a stable and low work function, is about five orders of magnitude lower compared to the flux of H as conversion particle. The flux of electrons is up two two orders of magnitude larger compared to negative hydrogen ions; however, with the assumption of isotropic fluxes, Γ_{e^-} towards the PG is overestimated.

2.6 Caesium dynamics

Understanding of the Cs dynamics is of importance for the development of large-scale H$^-$ sources: in addition to find possible correlations with the source performance, it has a direct impact on the design and position of the Cs oven and its evaporation nozzle as well as on the control of the Cs evaporation rate out of the Cs oven. The Cs dynamics has also a direct influence on the required
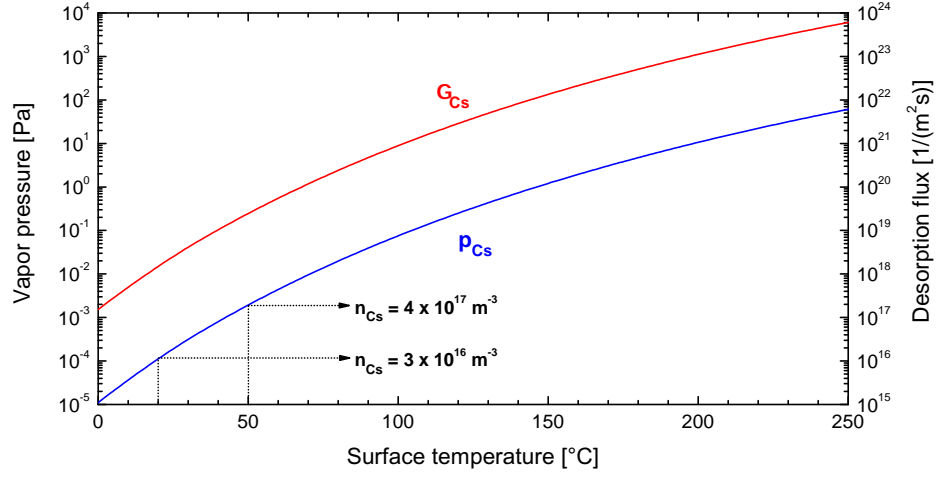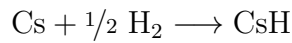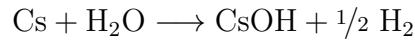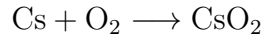
Figure 2.15: *Cs vapor pressure [45] and corresponding desorption flux as a function of the surface temperature, valid for thick (> 1 ML) Cs layers. Also indicated is the resulting Cs volume density for a temperature of* 20 °C *and* 50 °C*.*

temperature of the source walls and of the plasma grid – this is of particular interest for the design of the ITER HNB, since the electrical conductance of hot water provided to the source at a potential of −1 MV must be taken into account.

Cs is one of the most reactive chemical elements. For instance, it can form compounds with vacuum impurities as oxygen or water, but also with hydrogen gas:

$$\mathrm{Cs} + \mathrm{O_2} \longrightarrow \mathrm{CsO_2}$$

$$\mathrm{Cs} + \mathrm{H_2O} \longrightarrow \mathrm{CsOH} + {}^1\!/_2\,\mathrm{H_2}$$

$$\mathrm{Cs} + {}^1\!/_2\,\mathrm{H_2} \longrightarrow \mathrm{CsH}$$

The low melting temperature of pure Cs (28.5 °C [7]) results in a high vapor pressure p_{Cs}, which is plotted in figure 2.15 as a function of the surface temperature in combination with the resulting desorption flux $\Gamma_{\mathrm{Cs}} = \frac{1}{4} n_{\mathrm{Cs}} \bar{v}_{\mathrm{Cs}}$ using $T_{\mathrm{Cs}} = T_{\mathrm{surface}}$. These values are valid for bulk Cs and thus for thick Cs layers, which means a Cs coverage of more than one mono layer (ML), where metallic bonding dominates. At thinner Cs coverage (< 1 ML), a stronger ionic bonding is formed to the substrate, resulting in a reduced vapor pressure. In contrary, Cs compounds have a much lower vapor pressure compared to Cs and thus keep stuck at the surface (e.g. the melting temperature of CsOH is 342 °C [7]).

For the estimation of the area density of Cs atoms, the atomic radius of Cs in a metallic bonding is used, which is 2.67 Å [46]. Using full coverage, this results in
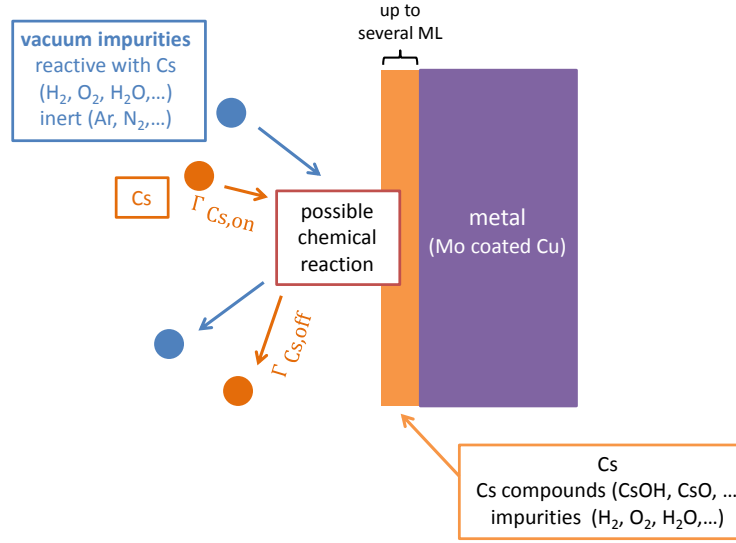
Figure 2.16: *Sketch of the particle fluxes and layer formation at the source wall during vacuum phases.*

an area density of 4.5×10^{18} atoms/m^2. Thus, the typical neutral Cs flux in the source (see table 2.4) results in 0.01–0.04 ML/s.

Since the large, pulsed-driven negative hydrogen ion sources cannot operate in ultra high vacuum conditions (the background gas pressure is typically 10^{-7}–10^{-6} mbar), a complex interplay takes place at the source walls: the density of background gas particles is 10^{15}–10^{16} m^{-3}, being one order of magnitude higher than the typical Cs density during vacuum phases of 10^{14}–10^{15} m^{-3} [47]. Although the temperature of Cs might be higher due to evaporation out of a hot oven containing a liquid or solid Cs reservoir ($T > 150$ °C), the flux of vacuum impurities towards the wall is larger than the flux of Cs atoms because of the high atomic mass of Cs (133 u). This results in a steady formation of Cs compounds at the plasma grid as well as at the source walls. A sketch of the Cs dynamics close to the wall during vacuum phases is shown in figure 2.16.

A microscopic analysis of the formed Cs layers at the wall is not possible, since a possible ex-situ analysis suffers from the change of the Cs layers under air or not sufficient clean vacuum conditions after dismounting a sample and in-situ diagnostics are not available. For this reason, the Cs dynamics must be described by usage of macroscopic quantities (e.g. the Cs volume density or the surface work function). Several effects regarding the Cs dynamics have been found empirically during operation of the prototype source:

- An elevated wall temperature of ≥ 35 °C increases the desorption flux of Cs

and avoids local thick accumulations of Cs. It was found that the elevated temperature helps to achieve high source performance (high extracted H^- current density as well as a low amount of co-extracted electrons) [48]. Under some circumstances, it was also possible to achieve high source performance at lower temperatures; however, the conditioning time until the source delivered optimum performance (a typical operational scenario will be discussed in section 2.7) is increased. For this reason, the wall temperature is controlled to a temperature of 35 °C by a water cooling/heating system. Nevertheless, the surface temperature of the wall is increased during plasma pulses (e.g. up to 10 K at BATMAN) as a result of a temperature gradient.

- The temperature of the plasma grid is a critical parameter: a temperature of the plasma grid of more than 100 °C is necessary in order to achieve a high source performance. For this reason, the plasma grid is heated to a temperature of 150 °C by usage of ohmic heating wires at the BATMAN short-pulse test facility and is temperature controlled to a similar temperature by an air or water cooling/heating system at the MANITU and ELISE long-pulse test facilities, respectively. This effect might be attributed to a reduction of impurities from the surface.

- The background gas pressure is critical for the operation: reduction from a couple of 10^{-6} mbar to a value of $< 10^{-6}$ mbar after elimination of small vacuum leaks resulted in a reduction of the required conditioning time at BATMAN. Of particular importance seems to be the amount of water as impurity: a small water leak in the cooling system of the extraction grid at BATMAN led to a small increase of the background gas pressure (2–3×10^{-6} mbar); however, it was not possible to achieve a high source performance until the extraction grid has been replaced.

Due to the high chemical reactivity in combination with the vacuum conditions in the source, a continuous flux of Cs onto the plasma grid is required during source operation in order to achieve a stable and high source performance. The Cs density during vacuum phases is in the range of 10^{14}–10^{15} m^{-3}, and by this about two orders of magnitude lower compared to the density calculated out of the vapor pressure (compare to figure 2.15) – thus, the Cs dynamics inside the source is not determined by the vapor pressure of pure Cs. Desorbing Cs fluxes play a much minor role for the Cs distribution in vacuum phases. For this reason, a macroscopic description of the Cs dynamics has been introduced [48] by usage

of the sticking coefficient S defined by

$$S = 1 - \frac{\Gamma_{\text{Cs,off}}}{\Gamma_{\text{Cs,on}}}, \qquad (2.16)$$

with $\Gamma_{\text{Cs,on}}$ denoting a Cs flux hitting a wall and $\Gamma_{\text{Cs,off}}$ the corresponding Cs flux leaving the wall. By this definition, a value of 0 means that each Cs atom reaching the wall will desorb, whereas a value of 1 would correspond to a total permanent adsorption of the incoming Cs flux.

Dedicated measurements in a lab experiment under similar vacuum and Cs conditions compared to the ion sources have been carried out, determining S to a value of 0.7–0.9 for wall temperatures between 88 °C and 26 °C [49]. Hence, most fraction of an incoming Cs flux keeps stuck at the wall and thus the distribution of Cs during vacuum phases within the source strongly depends on the position of the Cs oven in the ion source and the shape of the evaporation nozzle. The Cs density in the volume is then controlled by the evaporation out of the oven as the source term and sticking on the source wall, as a consequence of the formation of Cs compounds, as the sink and is thus mainly dependent on the Cs evaporation rate and the sticking coefficient.

During plasma phases, the Cs dynamics becomes more complex: Cs can be released out of Cs compounds due to interaction with reactive plasma particles as well as due to exposure with plasma photons of sufficient energy. Thus, a large redistribution of Cs can take place during plasma phases. However, for the Cs dynamics one has to take into account that a large fraction of Cs is ionized due to the low ionization energy of Cs (3.89 eV [7]), the total amount of Cs consisting of neutrals and ions: $n_{\text{Cs,tot}} = n_{\text{Cs}^0} + n_{\text{Cs}^+}$. Unfortunately, only neutral Cs particles are easily accessible with optical diagnostics, mainly due to the large excitation threshold of the Xe-like Cs⁺ ion: the excitation energy from the ground state 5p^6 to the lowest excited state $5\text{p}^5 6\text{s}$ is 13.3 eV [50]. For the same reason, the ionization energy of Cs⁺ is high (23.16 eV [7]) and thus the fraction of Cs²⁺ is negligible.

In order to gain a deeper insight into the redistribution processes of Cs layers inside the source during vacuum and plasma pulses, the 3D Monte Carlo code `CsFlow3D` has been developed some years ago [48]. One main result of this code was the necessity of temperature regulation of all parts of the ion source in long pulses: an experimentally observed increase of the Cs amount during long plasma pulses at MANITU could be correlated with a heat-up of the not-actively cooled
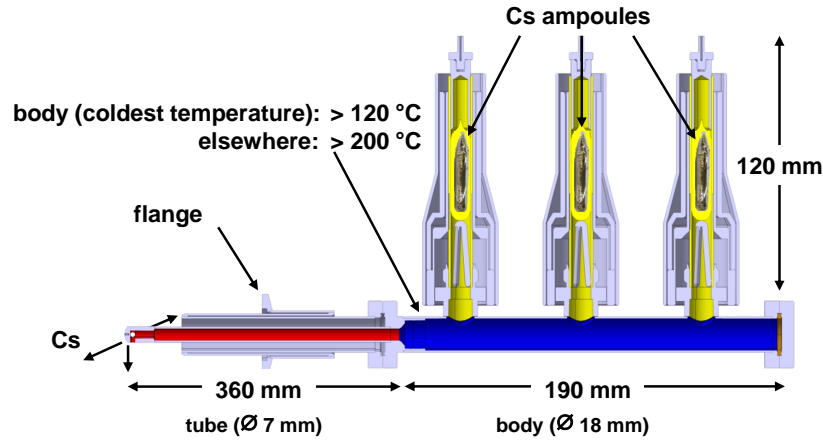
Figure 2.17: *Drawing of the Cs oven based on a liquid Cs reservoir.*

bias plate. For this reason, a temperature regulation of the bias plate has been implemented in the ELISE test facility and is also part of the design of the ITER HNB source in order to avoid an uncontrolled release of Cs. Due to the short plasma pulse length at BATMAN, there is no explicit temperature regulation of the bias plate necessary.

The importance of the plasma phase on the surface work function has been investigated in a lab experiment: the work function of a metal sample has been measured in a lab experiment for a pulsed plasma during the plasma-off phase under ion-source conditions (it is not possible to determine the work function during plasma phases, as will be discussed in chapter 3). The pulse frequency has been chosen to be 18.5 Hz with a duty cycle of 40% plasma on and 60% plasma off. Under these conditions, the work function is significantly reduced compared to vacuum operation only: 2.2 eV in contrary to 2.6 eV [51] with similar Cs evaporation rates in both cases.

Caesium ovens at the test facilities

A Cs oven is used at the test facilities and foreseen for the ITER HNB source for the evaporation of Cs into the source. The typical required Cs evaporation rate at the small prototype source is about 5–10 mg/h. Two different types of Cs ovens have been used for this purpose at the IPP test facilities in the last years:

The standard IPP Cs oven design – which is shown in figure 2.17 – is based on a liquid Cs reservoir. The liquid Cs reservoir is created out of breaking one glass ampulla containing 1 g liquid Cs under vacuum conditions. One ampulla
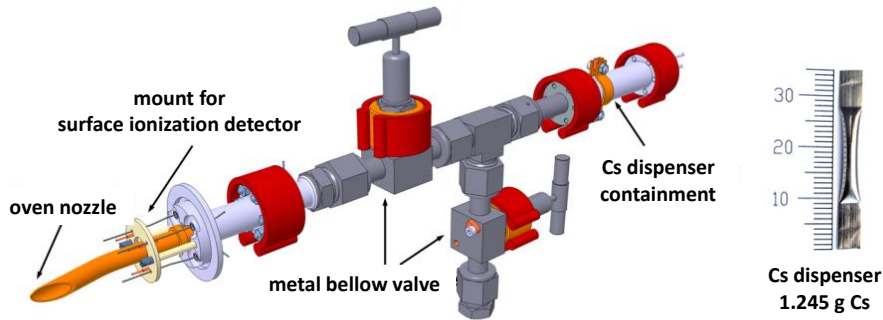
**Figure 2.18:** *Left: drawing of the Cs dispenser oven. Right: picture of a Cs dispenser.*

lasts for several weeks of operation. The oven can contain up to three ampoules to avoid the necessity of frequent venting of the ion source. The evaporation rate can be controlled by the temperature of the body (the part of the oven containing the liquid Cs reservoir), which controls the vapor pressure of Cs. To ensure precise controllability of the Cs evaporation rate, the other parts of the oven (tubes, flanges, nozzle etc) must be heated to a higher temperature that the vapor pressure is only controlled by the temperature of the body. Cs ovens based on a liquid reservoir are also used in different large-scale H⁻ sources, e.g. in Japan since several years [52].

The liquid oven has a nozzle consisting of three holes, resulting in an evaporation of Cs towards both side walls and the bottom wall of the expansion chamber. No direct evaporation towards the extraction system has been chosen due to concerns regarding Cs adsorption in the extraction system and thus the high voltage sustainment of the extraction system.

Newly in use at the IPP negative ion sources is a Cs oven based on a Cs dispenser [53], which is shown in figure 2.18. In the used dispenser[13], Cs is chemically bound in a solid compound (Bi_2Cs). The dispenser is sealed by a indium cover. During the first usage, the indium seal is melted by ohmic heating. The evaporation rate of the oven can be adjusted sensitively by change of the heating current (up to 10 A), where Cs is temperature-dependent released out of the compound. The oven structure is heated to a temperature of 280 °C to avoid Cs sticking. By means of two valves an empty dispenser can be exchanged without breaking the vacuum of the ion source.

---

[13]Alvasource AS-6-Cs-1245-S, manufacturer: alvatec, Griffen (Austria)
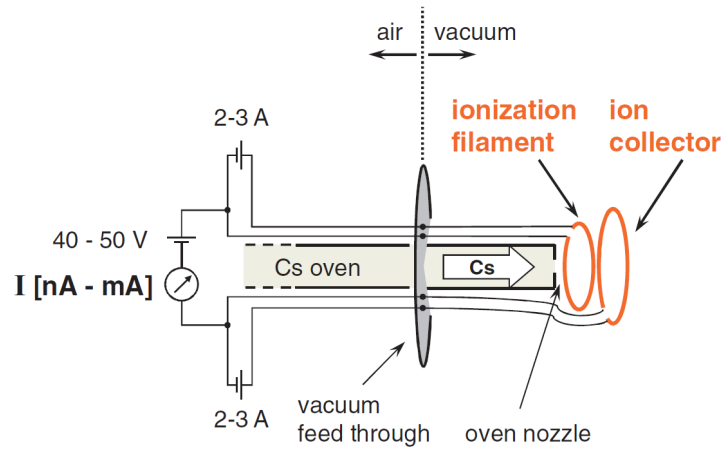
Figure 2.19: *SID mounted in front of the Cs oven nozzle [53].*

The nozzle of the dispenser oven is a slightly tilted open pipe with direct evaporation of Cs towards the plasma grid in the prototype source. The different design compared to the liquid oven has been chosen to check whether indirect Cs evaporation is necessary for HV stability as well as to compare the required Cs evaporation rate. In the first year of use at BATMAN, neither a deterioration of the high voltage sustainment of the extraction system nor a significant change of the required Cs evaporation rate has been observed.

For measuring the Cs evaporation rate, a Surface Ionization Detector (SID) is mounted in front of the oven nozzle of the dispenser oven. The SID has become a helpful tool in order to control the Cs evaporation rate.

Surface ionization detector

A sketch of a surface ionization detector mounted in front of the Cs oven nozzle is shown in figure 2.19. The setup is similar to a Bayard-Alpert ionization gauge, consisting of two tungsten filaments – however, ionization takes not place by electron collision, but by the surface effect: the work function of tungsten ($\chi_W = 4.55$ eV [54]) is larger than the ionization energy of Cs ($E_i = 3.89$ eV [7]). For this reason, a transition of the valence electron of Cs into the conduction band of tungsten is possible, resulting in an ionization of the Cs atom. With a voltage applied between both filaments, the measured current reflects the amount of ionized Cs at the first filament.

Both filaments are heated ohmically in order to avoid sticking of Cs at the filaments – the Cs coverage at the filaments should be small in order not to influence significantly the work function of the tungsten wire. If assuming that

the residence time of a Cs atom at the surface is short enough that no significant coverage of Cs is reached and long enough for the atom to get into thermal equilibrium with the surface at temperature T, the fraction of ionized particles to neutral particles Γ_+/Γ_0 leaving the surface follows the relationship [55]:

$$\frac{\Gamma_+}{\Gamma_0} \propto \exp\left(\frac{\chi - E_i}{k_B T}\right). \tag{2.17}$$

Hence, for constant temperature T the current between the two filaments corresponds to the incoming flux of Cs onto the first filament. Consequently, for a fixed geometry of the filaments in front of the oven nozzle, the current depends linearly on the Cs evaporation rate of the oven. The measured electrical current between the filaments is in the order of 5–15 μA for typical Cs evaporation rates.

Only some alkali metals fulfill the condition $E_i < \chi_W$ and can be ionized in a significant amount. Since Cs is the only alkali metal inside the ion source, only the flux of Cs is measured by the SID.

Calibration of the measured electrical current $I_{SID}(t)$ resulting in the absolute evaporation rate $\Gamma_{Cs}(t)$ [mg/h] is done after evaporation of a complete dispenser containing Cs with mass m_{Cs} and integration of the measured current:

$$m_{Cs} \hateq \int I_{SID}(t)\mathrm{d}t \implies \Gamma_{Cs}(t) = I_{SID}(t)\frac{m_{Cs}}{\int I_{SID}(t)\mathrm{d}t}. \tag{2.18}$$

Up to now, a precise calibration of the Cs dispenser oven at BATMAN was not possible due to experimental restraints – however, a rough calibration revealed an Cs evaporation rate of 10 mg/h at a measured SID current of 7 μA, which is the typical current at the used Cs evaporation rate during BATMAN operation.

2.7 Typical operational scenario

Operation of the test facilities takes place during the day with continuous evaporation of Cs into the source. No operation is done during night or weekend; during this time also the evaporation of Cs is stopped – however, the source stays under vacuum.

When beginning an experimental campaign, the source has been often vented before, resulting in a deterioration of Cs on all surfaces due to the high chemical reactivity of Cs. For this reason, operation starts with a Cs conditioning phase: for a time between usually 1 and 3 days the source is operated continuously while the performance (high extracted H⁻ current density, low co-extracted electron

current density) increases from shot to shot. At the beginning of this phase, H^- is mainly produced by volume production, whereas the fraction of surface produced H^- is increasing with lowering the work function of the plasma grid. When starting the Cs conditioning phase, the source performance is limited by the amount of co-extracted electrons, what requires the usage of limited source parameters (lowered RF power and extraction voltage). These parameters are increased stepwise during the Cs conditioning phase. The Cs evaporation rate is adjusted in order to obtain stable and high source performance, based on the experimental experience of the operator.

At the beginning of each day of operation a reconditioning is required after the long vacuum phase and decrease of the source and plasma grid temperature to room temperature during night, as the source performance is worse compared to the end of the day before. Usually a total plasma time of about 100 s (corresponding to 15 BATMAN pulses or less MANITU pulses with longer pulse time) with evaporation of Cs is required to re-achieve the same source performance [56]: the cleaning effect of the plasma pulses in combination with the redistribution of Cs is required for reconditioning the source.

3 Applied diagnostic methods and setup at the test facilities

For the investigation of the dynamics in the extended boundary layer of the prototype ion source a multitude of diagnostics is used, allowing the simultaneous determination of several parameters. These diagnostics will be introduced within this chapter as well as the diagnostic setup at the test facilities will be shown.

The source performance is determined by an electrical measurement of the extracted H^- and electron current as the current between the PG to ground and the current between the PG to the extraction grid, respectively [10]. It should be mentioned that due to poor beam optics, where the optimum perveance is not matched at each setting, a small fraction of the extracted H^- current can hit the extraction grid and thus counts to the measured co-extracted electron current. This effect has in particular to be taken into account for the case $j_e/j_{H^-} \ll 1$, in which the measured value of the co-extracted electron current density is much smaller than the extracted H^- current density in combination with a poor perveance matching.

The additionally applied source diagnostics need to work under harsh environment, i.e. a strong RF field causing noise during plasma phases and the source at high voltage during extraction. As consequence, this results in the following requirements for the diagnostics:

- If possible, optical diagnostics should be coupled via fibers to the ion source. By fiber usage, the HV separation can be realized easily and critical components of the diagnostic can be positioned at a larger distance from the source, resulting in less problems due to RF noise.

- Electrical diagnostics at the source must operate at high voltage. For this reason, their setup should be very compact and cables should be short in order to avoid strong coupling of RF noise. Careful grounding is required to avoid ground loops.

Of most interest and thus a a very desirable diagnostic would be the measurement of the work function χ of the plasma grid. As χ correlates directly with the surface production rate of H$^-$, this results in a direct correlation with the amount of extracted H$^-$ and co-extracted electron current density, when volume production of H$^-$ becomes negligible and the flux of produced H$^-$ is not space-charge limited. However, there are several issues regarding a work function measurement at the prototype ion source:

- A non-invasive method would be required in order not to disturb the caesiation or the plasma close to the convertor surface.

- Non-invasive techniques for determining the work function are based on the measurement of the photo current while exposing the material to light. Since the photo current is much lower compared to typical currents flowing in the plasma, this technique can not be applied during plasma phases – only measurements in the vacuum phases are possible.

- However, it is known that the plasma has an important effect on the work function of the converter surface, since Cs layers deteriorate during vacuum phases. As already mentioned, measurement in a lab experiment for a pulsed plasma (the photo current is measured during the plasma-off phase) showed for ion-source conditions that the work function is significantly reduced for caesiation during pulsed plasma operation compared to vacuum operation only (2.2 eV in contrary to 2.6 eV, [51]).

- The expected weak signals (photo currents in the order of nA) in combination with the harsh conditions mentioned above hamper the measurement at the prototype source.

Due to these reasons, no diagnostic for in-situ determination of the work function has been applied up to now neither at the IPP prototype ion source nor at any other H$^-$ source for fusion plasma heating. Indirect methods have to be used to gain a deeper understanding of the dynamics within the extended boundary layer, e.g. the measurement of the Cs density and thus the Cs flux towards the surface and the H$^-$ density inside the source.

Table 3.1 gives an overview about the measurement quantities and spatial resolution delivered by the source diagnostics, which have been in use during this work. The temporal resolution is 40–170 ms for the optical diagnostics and

Table 3.1: *Source diagnostics applied, their measurement quantities and spatial resolution.*

Diagnostic	Measurement quantity		Spatial resolution
Cs absorption spectroscopy	n_{Cs^0}	Cs ground state density	LOS integr.
Cavity ring-down spectroscopy	n_{H^-}	H^- particle density	LOS integr.
Langmuir probe	Φ_{pl} $n_{\mathrm{i}+}$ T_{e}	plasma potential positive ion density electron temperature	local
Optical emission spectroscopy	ϵ_i $n_{\mathrm{H}}/n_{\mathrm{H}_2}$ n_{e} T_{e} $\vdots$	molecular and atomar line emissivity dissociation ratio of hydrogen electron density electron temperature	LOS integr.

1 s for the Langmuir probes, which is sufficient for the characterization of a 6 s BATMAN or longer MANITU pulse, respectively.

The source diagnostics determine either line-of-sight averaged (optical diagnostics) or local (Langmuir probes) parameters at the available diagnostic ports with an axial distance of 0.7 cm or 2.2 cm to the plasma grid. As has been shown in figure 2.11, the resulting magnetic field has a complex 3D structure close to the plasma grid, resulting in a complex transport of electrons. Unfortunately, it is not possible to position the diagnostics closer to the plasma grid due to the following reasons:

- Optical diagnostics have a LOS diameter of typically 1 cm and thus are intrinsically averaging over a certain axial distance.

- The bias plate is positioned at an axial distance of 1 cm in front of the plasma grid and is thus blocking LOS distances closer to the plasma grid. The available diagnostic ports with their resulting lines-of-sight in vertical and horizontal direction are shown in figure 3.1 for the BATMAN test facility (similar ports and thus resulting LOS are available at MANITU): the axial distance to the plasma grid is 2.2 cm for most LOS – these LOS are at least
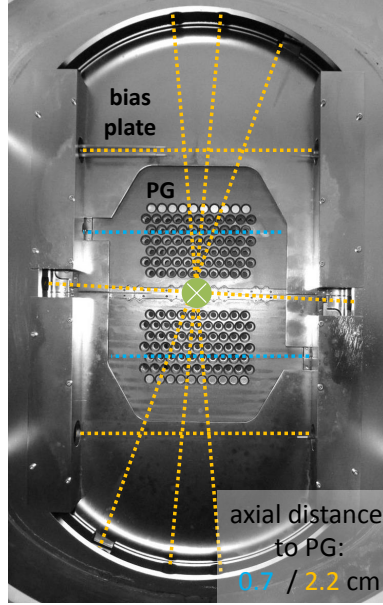
Figure 3.1: *Available lines-of-sight resulting from the existing diagnostic ports at the prototype ion source with their axial distance to the plasma grid. Shown is the view from the driver towards the plasma grid at the BATMAN test facility.*

partly positioned in front of the bias plate. Two horizontal LOS have a smaller distance of 0.7 cm to the plasma grid, since the bias plate is cut at these positions. In addition, one axially centered LOS through the driver towards the plasma grid is available for characterization of the driver plasma.

3.1 Cs absorption spectroscopy

Using absorption spectroscopy, the line-of-sight integrated particle density in the lower state k of an optical transition to an upper state i can be determined. An optical transition is called resonant if the lower state is the ground state, meaning that absorption spectroscopy at a resonant transition reveals the ground state density of a particle species.

In a homogeneously absorbing medium, the intensity of incoming light $I(\lambda, 0)$ at wavelength λ is reduced after passing a distance of length l to

$$I(\lambda, l) = I(\lambda, 0)e^{-k(\lambda)l}, \tag{3.1}$$

with $k(\lambda)$ denoting the absorption coefficient [57]. The Ladenburg equation links the absorption coefficient with the particle density n_k of the lower state:

$$\int\limits_{\lambda_1}^{\lambda_2} k(\lambda)\mathrm{d}\lambda = -n_k B_{ki}\frac{h\lambda_0}{\mathrm{c}}, \tag{3.2}$$

where integration is done over the whole absorption line between λ_1 and λ_2, B_{ki} denotes the Einstein coefficient for absorption, h the Planck constant and λ_0 the central wavelength of the optical transition. Using the Einstein coefficient for spontaneous emission A_{ik}, the line-of-sight integrated particle density becomes

$$n_k = \frac{8\pi c}{\lambda_0^4}\frac{g_k}{g_i}\frac{1}{A_{ik}l}\int\limits_{\lambda_1}^{\lambda_2} -\ln\left(\frac{I(\lambda,l)}{I(\lambda,0)}\right)\mathrm{d}\lambda, \tag{3.3}$$

with the degeneracy of the lower and upper state g_k and g_i, respectively.

For the measurement of the neutral Cs density, the resonant transition from the ground state $6^2\mathrm{S}_{1/2}$ to the excited $6^2\mathrm{P}$ state is chosen. Due to the fine structure, the $6^2\mathrm{P}$ state is split into two levels, $6^2\mathrm{P}_{3/2}$ (resulting in a transition at 852 nm) and $6^2\mathrm{P}_{1/2}$ (resulting in 894 nm). The transition at 852 nm is used because spectrometers become less sensitive in the IR and diode lasers are less available at 894 nm (see the different setups below). Due to the hyperfine structure, the ground state $6^2\mathrm{S}_{1/2}$ is split into two and the excited state $6^2\mathrm{P}_{3/2}$ into four levels. The selection rule of optical transitions results in six lines. Since in each case three lines overlap strongly due to the Doppler broadening at relevant particle temperatures (higher than room temperature), two lines can be resolved as indicated in figure 3.2 for a gas temperature of 300 K, which is the minimum temperature during vacuum phases. During plasma phases, the increased gas temperature results in an increased Doppler broadening.

Two different setups can be used for absorption spectroscopy:

- **White-light absorption spectroscopy** uses a broadband light source and a wavelength-sensitive detector – usually a spectrometer is used for this purpose.

- For the **laser absorption spectroscopy** a tunable laser serves as light source and a broadband detector is used.

Due to the limited accessibility of the ion source and for high voltage reason necessity of a fiber coupled system, the Tunable Diode Laser Absorption Spectroscopy (TDLAS) technique is applied. A single mode tunable diode laser is used as light source and a simple photo diode as detector, both connected to the
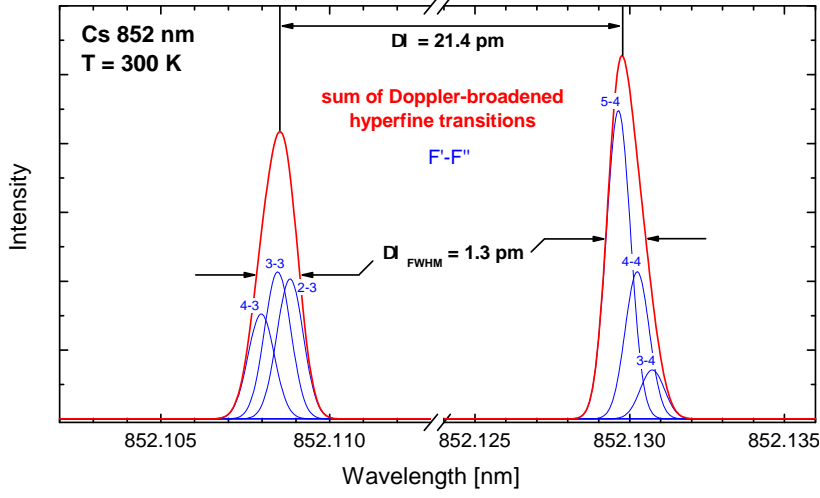
Figure 3.2: *Doppler-broadened spectrum of the Cs 852 nm transition for a gas temperature of 300 K. [47]*

source by optical fibers. Since the linewidth of the emitted light of single mode tunable diode lasers for scientific purposes is usually much more narrow (typically $\ll 0.1$ pm) compared to the spectral width of the Doppler-broadened line (> 1 pm, see figure 3.2), the Doppler-broadened absorption line can be directly resolved by TDLAS without significant additional broadening caused by the convolution of the two spectral linewidths. This is of importance since the latter could lead to an under-estimated particle density under certain circumstances [58]: although the measured, broadened absorption line $I_{\mathrm{meas}}(\lambda, l)$ yields the same value for the integral as the non-broadened absorption line $I(\lambda, l)$,

$$\int\limits_{\mathrm{line}} \left(\frac{I_{\mathrm{meas}}(\lambda, l)}{I(\lambda, 0)} \right) \mathrm{d}\lambda = \int\limits_{\mathrm{line}} \left(\frac{I(\lambda, l)}{I(\lambda, 0)} \right) \mathrm{d}\lambda,$$

the value of the integral required for the calculation of the particle density in equation (3.3) differs due to the non-linearity of the natural logarithm:

$$\int\limits_{\mathrm{line}} -\ln \left(\frac{I_{\mathrm{meas}}(\lambda, l)}{I(\lambda, 0)} \right) \mathrm{d}\lambda \neq \int\limits_{\mathrm{line}} -\ln \left(\frac{I(\lambda, l)}{I(\lambda, 0)} \right) \mathrm{d}\lambda.$$

At the IPP prototype ion source, a distributed feedback (DFB) laser[14] is used. The single mode operation of this type of diode laser is achieved by a periodic structure within the active region, leading to an optical interference filter. For tuning of the emitted wavelength, the optical length of the active

---

[14]Sacher Lasertechnik, CHEETAH DFB-852 with laser controller Pilot PC 500

region is modulated by variation of two parameters: change of the diode laser temperature (slow, large tuning range of several 100 pm), and change of the diode laser current (fast, narrow tuning range of several 10 pm). For this reason, the emission wavelength of the laser is tuned close to the absorption wavelength by temperature tuning once when the laser is switched on and tuning along the absorption peaks is done subsequently by current modulation.

Obviously, variation of the diode laser current does not only influence the output wavelength, but also the output intensity of the laser beam. For this reason, the intensity $I(\lambda, 0)$ is not constant along the absorption line. Additionally, it is observed that the shape of $I(\lambda, 0)$ changes with time, which is attributed to non-optimal grounding conditions and RF noise. Hence, $I(\lambda, 0)$ is determined newly for each measured absorption spectrum $I(\lambda, l)$ by an automated procedure: the absorption lines are searched in the spectrum, their signal is removed in order to determine the base line and a polynomial of seventh order is fitted to the remaining signal, acting as $I(\lambda, 0)$. The polynomial of seventh order has been empirically chosen because it fits the base line very well for several differently shaped base lines. The wavelength calibration of the measured spectrum is done at the two absorption peaks under assumption of a linear wavelength dependence on the laser diode current. The neutral Cs density can then be calculated by applying equation (3.3), using two Gaussian peaks fitted at the Doppler-broadened absorption signals. The individual steps for determination of the neutral Cs density out of an measured absorption signal are shown in figure 3.3. The spectrum consists of 2,000 data points leading to a robust fit of the absorption peaks. The measured Doppler-broadening of the absorption peaks proves that the flux of Cs is isotropic.

Two effects have to be taken into account for the evaluation of absolute particle densities with TDLAS:

1. Intense laser radiation can depopulate the lower state of the optical transition leading to an underestimation of the real particle density. For this reason, damping the laser light might be beneficial; however, a trade-off has to be taken between the temporal bandwidth of the setup, which is reduced for higher amplification of the detector signal, and the amount of depopulation. An absolute quantification is possible by usage of an absorption cell (vacuum cell with a small amount of Cs inside), where the Cs density can be calculated from the vapor pressure, which results from the temperature of the coldest spot of the absorption cell. The amount of underestimation can be determined in this way. However, the same laser beam shape and
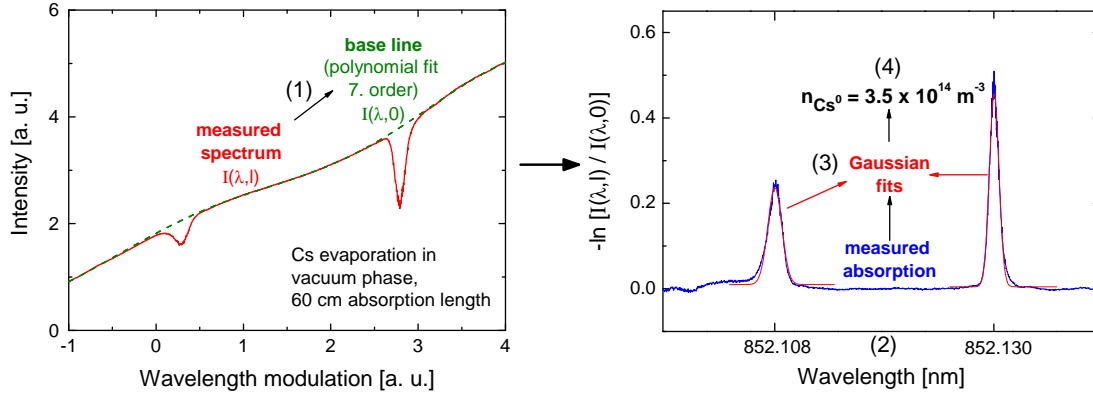
Figure 3.3: *Individual steps for determination of the neutral Cs density out of a measured absorption spectrum: (1) base line fit for determination of $I(\lambda, 0)$, (2) two point wavelength calibration, (3) Gaussian fits on the absorption signal, (4) calculation of the neutral Cs density.*

thus the same absorption length as in the experiment must be used. Due to the long absorption length (up to 60 cm at the prototype source) and the short length of available absorption cells (7.5 cm), the exact determination is not straight forward. Nevertheless, the factor of underestimation can be estimated by usage of the shorter absorption cell and neglecting effects of the different beam shape, resulting in a factor of underestimation of the Cs density between 1 and 3 for the setup used at the IPP prototype ion source. Since the exact value of underestimation is not known, all Cs densities shown within this work are not corrected and thus represent a lower limit of the real particle density. [59, 47]

2. The diode laser does not only emit radiation at its intensity peak, but also a broadband base radiation. Although this intensity is orders of magnitude lower compared to the peak intensity, it can lead to a significant offset on the measured absorption signal due to the broad wavelength emission. This can result in a flattening of the absorption peaks at strong absorption (long absorption length or high particle density) and thus in an underestimation of the real particle density. Correction is possible by fitting the real Gaussian profile at the wings of the measured absorption profile and is done automatically. [58]
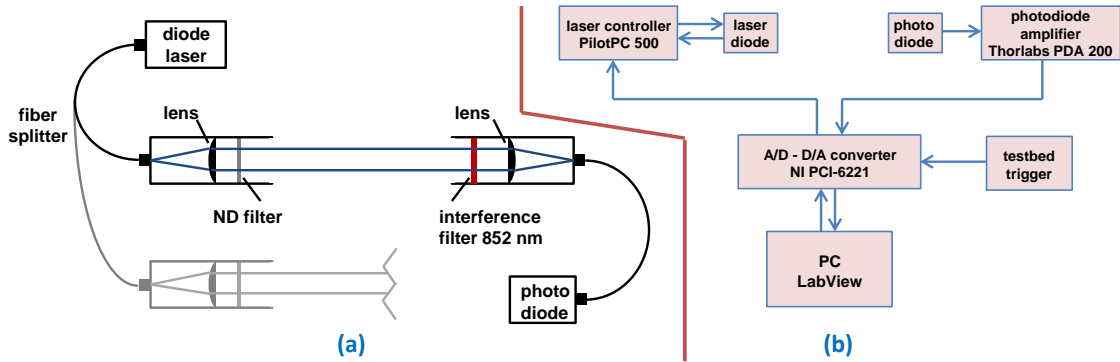
Figure 3.4: *Sketch of the Cs absorption setup: (a) optical setup, (b) schematic diagram.*

Setup at the prototype source

The setup of the Cs absorption spectroscopy (Cs-ABS) is shown in figure 3.4. The used diode laser has a single mode emission, a mode-hop free tuning range of several 100 pm and is fiber-coupled. The technical data of the laser is specified in table 3.2. At the diagnostic port of the ion source, an optical head creates a laser beam with a diameter of 12 mm by usage of a lens with a focal length of 25.4 mm. The optical head is also equipped with a neutral density filter (transmission $T = 1.8\%$ at 852 nm) in order to reduce the effect of ground-state depopulation by intense radiation. A second lens with the same focal length is used for refocusing the laser beam into an optical fiber at the opposite site of the ion source after passing the extended boundary layer as absorption medium. An interference filter ($\lambda_0 = 852$ nm, $\Delta\lambda_{\text{FWHM}} = 10$ nm) suppresses most of the plasma light during plasma operation, leading to no detectable offset on the measured signal during plasma pulses – an offset would strongly increase the effect described in the second item above. A fiber coupled photo diode[15] is used as detector; the photo current is amplified by a transimpedance amplifier[16] to a value of some volts using an amplification of 5×10^5 V/A. For simultaneous measurement at two lines of sight, the fiber between the laser and the optical head is split into two by a fiber splitter; the rest of the setup is then doubled, as indicated in figure 3.4 (a).

Shown in figure 3.4 (b) is the schematic diagram of the individual components and their controlling and measurement signals: the whole system is controlled by a PC with a combined A/D–D/A converter[17] attached, which is necessary to

---

[15]Thorlabs FDS02
[16]Thorlabs PDA200C
[17]National Instruments PCI-6221

Table 3.2: *Technical data of the CHEETAH DFB-852 diode laser.*

Parameter	Value
Tunable range	851–853 nm
Maximum output power	140 mW
Line width $\Delta\lambda_{\mathrm{FWHM}}$	0.01 pm

generate a sawtooth voltage sweep for the wavelength modulation of the laser as well as to record the amplified photo diode signal. A LabView program was created during this work which controls the diode laser current and thus its wavelength and evaluates the amplified signal of the photo diode; the length of the line of sight (0.2 m or 0.6 m, depending on the selected LOS) is taken into account. The absolute value of the neutral Cs ground state density is calculated, plotted and the data during the trigger event is stored in a data file. For data reduction, the data storage is triggered by the test facility, including 2 s pre-trigger (vacuum phase), the plasma phase and several s post-trigger (vacuum phase).

The Cs absorption system has been designed and gone into first operation using one LOS at the BATMAN test facility during the diploma thesis of the author [59, 47] and has been improved for routine operation and for operation at two LOS during this work.

Detection limit and error estimation

The detection limit of Cs-ABS is determined by an absorption which cannot be distinguished from the base line. With the automated evaluation routine explained above, the lower detection limit is about 1×10^{14} m^{-3}.

As mentioned before, a systematic underestimation of the line-of-sight averaged neutral Cs density takes place because of the depopulation of the ground state by a not exactly known factor between 1 and 3. In addition, a random error occurs due to the quality of the base line fit for the determination of $I(\lambda, 0)$, resulting in an random error of $\pm 10\%$ in the Cs^0 density.

The temporal bandwidth of the system is mainly limited by the bandwidth of the photo diode amplifier. With the used ND filter, the resulting bandwidth is 25 spectra per second or 40 ms, respectively.
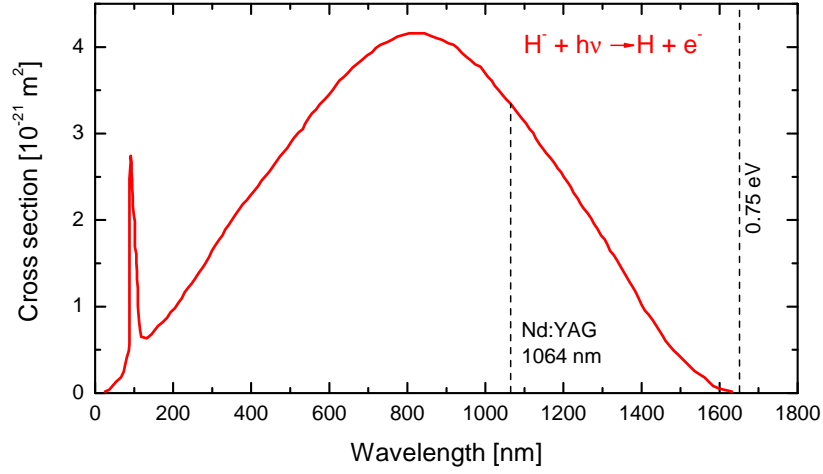
**Figure 3.5:** *Cross section for photo detachment of H^- [62] with the threshold at 0.75 eV.*

3.2 Cavity ring-down spectroscopy

The Cavity Ring-Down Spectroscopy (CRDS) is a special type of absorption spectroscopy technique. According to the Ladenburg equation (3.2), the absorption coefficient is low either at a low particle density n_k or at a transition with low absorption probability (a low Einstein coefficient for absorption B_{ki}). In these cases, almost no absorption takes place after passing the medium for one single turn. However, by using CRDS the detection limit can be lowered by several orders of magnitude. For the cavity ring-down spectroscopy, the decay time of a high-finesse optical cavity is measured after excitation with a laser. The main reason for the lowered detection limit is caused by the large number of several thousand times which the photons pass the absorption medium. CRDS has been developed in the late 1980s [60]. At the IPP prototype source it is applied for the measurement of line-of-sight integrated H^- particle densities [39, 61]. The absorption of light due to the photo detachment process is used for this purpose:

$$H^- + h\nu \longrightarrow H + e^-. \tag{3.4}$$

The cross section σ for this process is shown in figure 3.5. The photo detachment cross section is very broad along several 100 nm. When using a laser as light source with a spectral width of $\Delta\lambda \ll 1$ nm, the cross section can be set as constant in the laser wavelength range. For this reason, there is no scan along the absorption wavelength necessary and thus a CRDS system based on a short-pulse laser can be used.
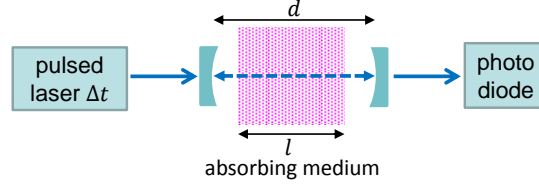
Figure 3.6: *Sketch of the setup for a pulsed CRDS system.*

A pulsed CRDS diagnostic consists of a pulsed laser, an optical cavity with the absorption medium inside and a detector. A sketch of the setup is shown in figure 3.6: a short laser pulse enters a high-finesse cavity formed out of a pair of high-reflective mirrors (typical reflectivity $R > 99.99\%$ at the laser wavelength) with distance d in between. The temporal width Δt of the laser pulse should be shorter than $\Delta t < 2d/c$, such that the laser pulse cannot interfere with itself inside the cavity avoiding the appearance of longitudinal cavity modes. For a typical cavity length (1.2 m at the IPP setup) this means that the laser pulse should be shorter than 8 ns. A photo diode detects the light escaping the optical cavity by transmission through the second mirror.

Consider a cavity formed of two identical mirrors with an effective reflectivity $R(\lambda)$, in which mirror losses and scattering effects are included. The intensity inside the cavity at wavelength λ after a number of N complete round-trips (distance $2d$) decays to

$$I(\lambda, N) = I_0(\lambda)\mathrm{e}^{-k(\lambda)l2N}R(\lambda)^{2N}, \tag{3.5}$$

with $I_0(\lambda)$ denoting the laser intensity after entering the cavity and $\mathrm{e}^{-k(\lambda)l}$ the absorption taking place within the absorption medium of length l each turn. With the approximation $\ln(R(\lambda)) \approx R(\lambda) - 1$ (fulfilled for $R(\lambda) \approx 1$) and the elapsed time $t = N \cdot 2d/c$ after the laser pulse entered the cavity, the time-dependent intensity becomes

$$I(\lambda, t) = I_0(\lambda)\exp\left(\frac{-tc}{d}\left[k(\lambda)l + (1 - R(\lambda))\right]\right). \tag{3.6}$$

The intensity within the cavity is reduced exponentially with time. By introducing a decay time $\tau(\lambda)$ via $I(\lambda, t) = I_0(\lambda)\mathrm{e}^{-t/\tau(\lambda)}$, the decay time $\tau_0(\lambda)$ without an absorbing medium ($k(\lambda) = 0$) becomes

$$\tau_0(\lambda) = \frac{d}{c\left(1 - R(\lambda)\right)}, \tag{3.7}$$

and with absorption medium

$$\tau'(\lambda) = \frac{d}{c\left[(1 - R(\lambda)) + k(\lambda)l\right]}. \tag{3.8}$$

This yields for the absorption coefficient $k(\lambda)$:

$$k(\lambda) = \frac{d}{c \cdot l}\left(\frac{1}{\tau'(\lambda)} - \frac{1}{\tau_0(\lambda)}\right). \tag{3.9}$$

Hence, the absorption coefficient can be determined by measurement of the decay time of the optical cavity with and without an absorbing medium.

As shown in figure 3.6, usually two concave mirrors are used forming a stable optical cavity. The length of the cavity d and radius of curvature of the mirrors r are chosen in a way that the stability criterion of an optical cavity is fulfilled:

$$0 \le \left(1 - \frac{d}{r}\right)^2 \le 1. \tag{3.10}$$

A standard Q-switched Nd:YAG laser is used as the pulsed light source, emitting at the fundamental wavelength of 1064 nm. For its narrow wavelength bandwidth ($\Delta\lambda \ll 1$ nm is well fulfilled for ns laser pulses), the absorption coefficient is $k(1064 \text{ nm}) = n_{H^-} \cdot \sigma(1064 \text{ nm}) = n_{H^-} \times 3.5 \times 10^{-21} \text{ m}^2$, as indicated in figure 3.5.

The necessity of using CRDS for measuring H^- particle densities instead of a single path absorption setup is derived from the following estimation: for conditions at the IPP prototype ion source, i.e. a laser wavelength of 1064 nm, $n_{H^-} = 5.5 \times 10^{16}$ m^{-3} (medium conditioned), $d = 1.2$ m, $l = 0.25$ m, one single pass yields a transmittance of $T = {}^I/_{I_0} = 0.99995$ (equation (3.1)), the absorption being hardly detectable. However, a CRDS setup starting with an intrinsic decay time of $\tau_0 = 47.4$ μs results in a reduced decay time of $\tau' = 30.2$ μs, being easily detectable – the main reason is that the absorption medium is passed 5,050 times in 30.2 μs.

A CRDS measurement for these parameters is plotted in figure 3.7. An exponential decay fits almost perfectly the measured signal. The oscillations on the signal are attributed to mode beating due to the excitation of several cavity modes.
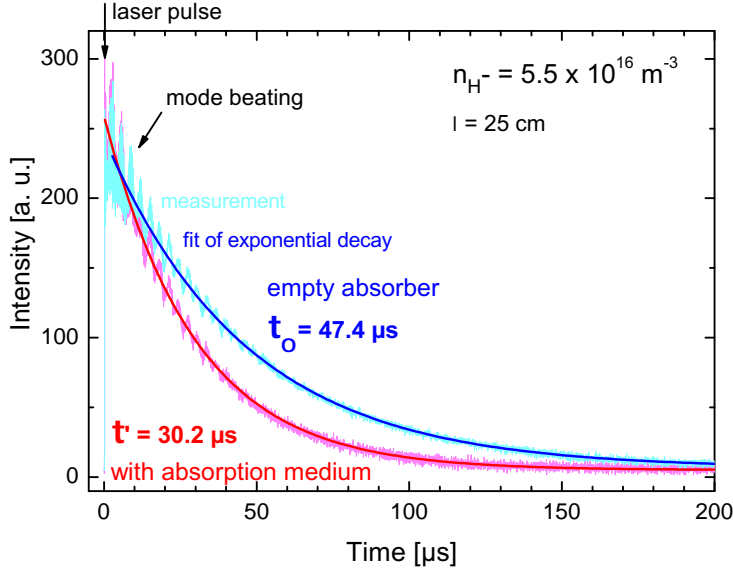
Figure 3.7: *Exponential decays of an empty (vacuum) cavity and one with a plasma containing H⁻ as absorber after excitation with a short laser pulse at BATMAN.*

Setup at the prototype source

The CRDS has been reinstalled at BATMAN during this work. The main components stayed the same as in [61]; however, some details have been improved significantly:

- The detection optics has been newly designed and shielded for laser safety issues. Additionally, the shielding resulted in a complete suppression of RF noise during plasma phases (compared to [39], figure 2).

- Improvements in the data acquisition resulted in a higher temporal resolution of 6 Hz compared to 4 Hz.

The optical setup as well as a schematic diagram of the CRDS system is shown in figure 3.8. A Q-switched Nd:YAG laser[18] is used as a pulsed light source, whose technical data are listed in table 3.3. The laser light is transmitted to the ion source by usage of several bending mirrors. At least two mirrors are required for the alignment of the laser beam to the central cavity axis. The cavity is formed out of two high reflective mirrors[19], each installed in a mirror mount. The technical data of the cavity mirrors is specified in table 3.4. An Viton ring in front of the

---

[18]Continuum Minilite II
[19]Layertec 107442
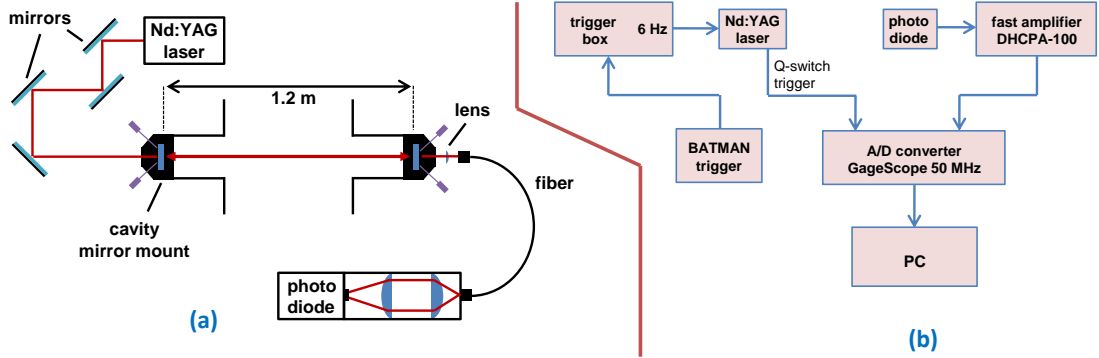
Figure 3.8: *Sketch of the CRDS setup: (a) optical setup, (b) schematic diagram.*

Table 3.3: *Technical data of the Continuum Minilite II Nd:YAG laser.*

Parameter	Value
Wavelength	1064 nm
Max. energy	50 mJ
Pulse width Δt_{FWHM}	5–7 ns
Repetition rate	1–15 Hz

high reflective mirror side determines the boundary between vacuum and normal pressure. The mirror itself can be slightly tilted by usage of three micrometer screws and subsequent squeezing the Viton ring; by this way the optical cavity can be properly aligned. A lens focuses the laser beam at the opposite site of the cavity into an optical fiber. An image of the fiber end on a photo diode[20] is produced by two lenses. The signal is amplified by a fast transimpedance amplifier[21] and recorded by a PC using an A/D converter[22]. Triggering during the plasma pulses is done by a trigger electronics, which converts the single BATMAN trigger event to multiple triggers with 6 Hz repetition frequency. The first trigger pulses are chosen to occur before plasma operation. Thus, the mean value of the cavity decay time of the first 3 trigger pulses is used as the intrinsic decay time τ_0 of the empty cavity. An automated routine calculates the time trace of the H^- density for each BATMAN pulse by fitting an individual exponential decay on each measured signal and stores it in a data file for each pulse.

---

[20]Thorlabs DET410 high speed InGaAs detector, 1 mm diameter of active area
[21]Femto DHCPA-100, bandwidth of 2.5 MHz at amplification 10^5 V/A
[22]GaGe GageScope 50

Table 3.4: *Technical data of the cavity mirrors.*

Parameter	Value
Curvature	plane-concave
Diameter	25 mm
Radius of curvature	1000 mm
Reflectivity at 1064 nm	99.994%
Transmission at 1064 nm	0.005%

For the used distance between the two high-reflective mirrors (1.2 m), the time period for one complete round trip of the light in the cavity (forward and backward) is $t_{\text{circ}} = 8$ ns. The pulse width of the laser pulse is $\Delta t_{\text{FWHM}} = 5$–$7$ ns. Although $\Delta t_{\text{FWHM}} < t_{\text{circ}}$ is fulfilled, laser intensity outside the FWHM part can interfere, resulting in some mode sensitivity of the optical cavity. Due to the appearance of longitudinal cavity modes and additionally a possible excitation of multiple transverse cavity modes, the recorded signal shows mode beating [63, 64].

Error estimation

Errors in the the measurement of n_{H^-} can only occur in the determination of τ, τ' and l.

A random error occurs due to the stability of the cavity: because the intrinsic decay time τ_0 cannot be measured at the same time as the decay time with absorber, a stable value of τ_0 must be assumed. With the used cavity mirrors, the decay time is stable with a deviation of ± 0.5 μs, resulting in an random error of $\Delta n_{\text{H}^-} = 1 \times 10^{15}$ m^{-3} at $\tau_0 = 47$ μs.

A systematic error of the line-of-sight averaged H$^-$ density occurs due to deviation of the absorber length l to the actual length. In the evaluation, the full length of the LOS between the two side walls is used.

3.3 Langmuir probes

Langmuir probes are powerful diagnostic tools for the characterization of plasmas, since they are able to deliver multiple plasma parameters as already shown in table 3.1. A Langmuir probe consists of a small electrical probe inside the plasma, on which a voltage is applied against the metallic wall and the current–voltage characteristic is measured. In order not to disturb the plasma significantly, the
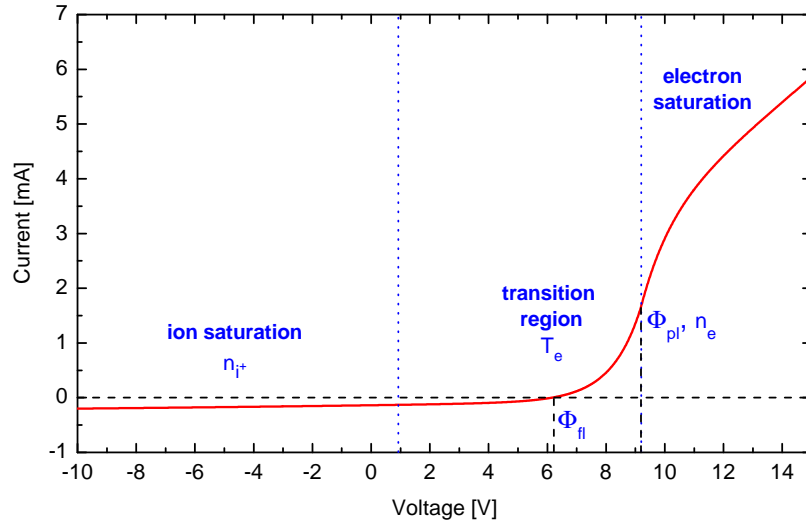
Figure 3.9: *Typical characteristic of a cylindrical probe with the different measurement regimes indicated.*

area of the probe should be that small that the resulting electrical currents are low (typically some mA). A small probe area is also required because the probe surface should limit the current at all applied voltages, meaning that the area of the wall of the experiment has to be much larger in comparison.

A typical characteristic of a cylindrical Langmuir probe is shown in figure 3.9 for a classical positive ion – electron plasma (no significant amount of negative ions). The resulting net current on the probe tip consists of the positive ion current I_+ and of the electron current I_-. Usually cylindrical probes are used, where a small tungsten wire (diameter in the order of 100 μm, length of several mm) acts as electrical probe. Several different regimes can be identified:

- The **ion saturation** regime takes place at sufficiently negative applied voltages to the probe. Almost all electrons are hindered from reaching the probe tip and thus the resulting current is dominated by positive ions: $|I_+| \gg |I_-|$. In this region, the potential of the probe is much lower than the plasma potential.

- At higher applied voltages, more and more electrons can reach the probe tip. This region is called the **transition region**. The current in this regime consists of both electrons and positive ions ($|I_+| \approx |I_-|$), where the electron part is increasing exponentially for Maxwellian distributed electron

velocities. The floating potential Φ_{fl} is defined as the potential with no net probe current.

- For applied voltages higher than the plasma potential $U > \Phi_{\mathrm{pl}}$, positive ions are repelled and **electron saturation** takes place: $|I_+| \ll |I_-|$. The electron saturation current is much higher compared to the ion saturation current, because at the same density (quasi-neutrality of the plasma) electrons create a higher particle flux due to their lower mass in combination with their typically higher temperature.

However, neither the electron nor the positive ion current saturates at typically applied voltages for cylindrical probes – although the boundary regimes are called 'saturation'. This behavior is caused by an establishing sheath around the probe tip: the effective probe area, i.e. the area around the probe, where plasma particles are collected, is larger than the area of the probe surface for $U - \Phi_{\mathrm{pl}} \neq 0$ V. This effect does not take place for an applied voltage equal to the plasma potential Φ_{pl}: the resulting current, which is called electron saturation current $I_{\mathrm{e,sat}}$, is then given by (neglecting the much smaller positive ion current)

$$I(\Phi_{\mathrm{pl}}) = A_{\mathrm{p}} e \Gamma_{\mathrm{e}} = A_{\mathrm{p}} \frac{1}{4} n_{\mathrm{e}} e \bar{v}_{\mathrm{e}} = A_{\mathrm{p}} \frac{1}{4} n_{\mathrm{e}} e \sqrt{\frac{8 k_{\mathrm{B}} T_{\mathrm{e}}}{\pi m_{\mathrm{e}}}} \equiv I_{\mathrm{e,sat}}, \qquad (3.11)$$

with the size of the probe tip A_{p}, the flux of electrons onto the probe tip Γ_{e} and the mean electron velocity $\bar{v}_{\mathrm{e}}$. The flux is reduced by $1/4$ because of the limited solid angle of particles hitting the probe tip (compare to equation (2.13)).

Using this equation, the electron density can be derived easily if the plasma potential is known. The plasma potential is given by the voltage at the maximum slope of the current:

$$U = \Phi_{\mathrm{pl}} \Leftrightarrow \frac{\mathrm{d}^2 U}{\mathrm{d} I^2} = 0. \qquad (3.12)$$

This connection can be derived since the electron current in the transition region, given by

$$I_{\mathrm{e}} = I_{\mathrm{e,sat}} \cdot \mathrm{e}^{\frac{e(U - \Phi_{\mathrm{pl}})}{k_{\mathrm{B}} T_{\mathrm{e}}}}, \ U \leq \Phi_{\mathrm{pl}} \qquad (3.13)$$

rises exponentially for voltages below the plasma potential; at higher applied voltages, additional electron current can only be drawn by an increasing sheath size, which is enlarged less than exponential for increasing voltage. Hence, the slope of the characteristic is decreased.

By usage of equation (3.13), the electron temperature T_e can be determined as the slope of the logarithmic electron current:

$$\ln I_e = \text{const.} + \frac{e(U - \Phi_{pl})}{k_B T_e}.$$ (3.14)

The ion current needs to be subtracted from the total current before equation (3.14) can be used. The determination of the ion current and thus also of the positive ion density is more challenging from the theory point of view, since information of the effective probe area at a certain applied voltage is required. Three theories are commonly used for the description of the ion collection, all of them assume a collision-less sheath:

1. The **Orbital Motion Limit (OML)** theory [65] describes ions coming from infinity and performing orbital motion in a thick sheath, much larger than the probe. In this case, not all ions hit the probe due to the possibility of orbital motion. The conservation of energy and angular momentum is considered for the initial and final state of the motion, and thus the shape of the potential distribution in the sheath is not of relevance, as long as the gradient is low enough that no absorption radius for ions occurs due to a strong electric field. The OML ion current is then [66]

$$I_{i+} = A_p n_{i+} e \frac{\sqrt{2}}{\pi} \sqrt{\frac{e(\Phi_{pl,1} - U)}{m_{i+}}},$$ (3.15)

   with $\Phi_{pl,1}$ denoting a temporary plasma potential used for fitting – this can differ slightly from the real plasma potential and should therefore not be used as such. Although the theory should be valid only in very thin plasmas combined with thin probe tips, Chen found a surprising validity of the OML theory in RF plasmas exceeding the intended range [66].

2. The **Allen–Boyd–Reynolds (ABR)** theory [67] describes the formation of a proper sheath around the probe tip by solving the Poisson equation for calculation of the potential distribution and thus the sheath size. However, this theory starts with stationary ions ($T_{i+} = 0$), so no orbital motion is considered. Thus, more ions than in reality impinge the probe tip in this theory, and therefore it often overestimates the real ion current and by this underestimates the real positive ion density. The best validity is expected for a thin sheath thickness.

3. The **Bernstein–Rabinowitz–Laframboise (BRL)** theory [68, 69] takes into account both the orbital motion of Maxwellian ions as well as the formation of a proper sheath and is for this reason the best description from the theoretical point of view. In experiments, however, the deviation can be larger compared to the other theories, in which the BRL theory often overestimates the real ion density [66, 70].

These different theoretical approaches already show that the evaluation of the ion saturation current is not as straight-forward compared to the electron density. However, the evaluation of the electron density can fail under certain circumstances:

- **Large electron current:** a large electron current can disturb the plasma, if I_e significantly influences the global particle flux distribution inside the plasma. This effect is not relevant at the IPP prototype ion source, if adequate small probe tips resulting in currents of several mA are used. In contrary, also the bias circuit acts as a probe with the large area of the plasma grid, where this condition is not fulfilled: a large bias current (in the range of A) is drawn to the plasma grid for the desired reduction of co-extracted electrons (see section 2.5).

- **Magnetic field** [71]**:** in presence of a magnetic field, the electron current onto the probe is reduced due to the magnetization of electrons and thus hindered mobility in the directions perpendicular to the magnetic field lines. The magnitude of the effect can be estimated by comparing the electron gyration (Larmor) radius $r_{L,e}$ to the probe diameter r_p: at strong magnetization of the electrons, i.e. $r_{L,e} < r_p$, they can reach the probe only from one direction. Typical values in the extended boundary layer of the prototype ion source ($T_e = 1$ eV, $B = 4$ mT) results in $r_{L,e} \approx 850$ μm, being larger then the used probe tip radii ($r_p \leq 150$ μm), so no strong effects due to the magnetic fields are expected. However, since the probes are mounted parallel to the magnetic filter field (see section 3.5) and the probe mount has a thickness of several mm, shadowing effects can still occur. In addition, due to the complex and varying magnetic field topology in the area close to the plasma grid (the axial distance of the probes to the PG is 7 mm), the magnitude of the shadowing effect can differ spatially.

- **Signal noise:** the maximum in the slope of the probe current can often not be clearly determined, e.g. due to signal noise, resulting in an error bar of the

plasma potential of some volts. Since the electron density is calculated from the probe current at the plasma potential and I_e is exponentially increasing in this regime (equations (3.11) and (3.13)), the resulting error bar of the electron density can be significant, in the order of several 10%.

- **RF oscillations:** in RF-created plasmas, the plasma potential oscillates with the RF frequency. This can lead to an erroneous shape of the probe characteristic due to averaging effects of the slower data acquisition system (in the order of kSamples/s) with the RF frequency (MHz) and by this to erroneously determined plasma parameters.

Due to these reasons as well as the influence of H^- on the probe evaluation (which will be discussed later), the electron density has not been directly determined by Langmuir probe measurements during this work. Nevertheless, the issue of RF oscillations is of particular importance, since the determination of the correct plasma potential is required in order to determine the potential profile of the PG sheath. Thus, RF oscillations must be compensated.

RF oscillations and probe compensation

Consider an oscillating plasma potential $\Phi_{pl}(t) = \Phi_{pl,0} + A\sin(2\pi f_{RF}t)$ with oscillating amplitude A at the RF frequency f_{RF} ($\simeq 1$ MHz at the prototype ion source). Since the measurement time of the probe current at each voltage set point (196 μs for the used probe electronics) is longer than the time of one oscillation ($\simeq 1$ μs), the measured characteristic is intrinsically temporally averaged for several (≈ 200) oscillations. The effect of the oscillating plasma potential on the measured probe characteristic has been calculated and is shown in figure 3.10 for an amplitude $A = 2$ V, in which additionally the undisturbed probe characteristic is plotted.

The amount of disturbance depends on the ratio $A/(\frac{k_b}{e}T_e)$, because a large electron temperature broadens the characteristic and thus a plasma potential oscillation with the same amplitude delivers less distortion [72]. No significant change of the measured characteristic takes place for $A \ll \frac{k_b}{e}T_e$, whereas for the case shown ($A/(\frac{k_b}{e}T_e) = 2$) the RF oscillations lead to significant deviations from the undisturbed characteristic: the error in the disturbed trace (green) is larger in areas, where the characteristic is strongly non-linear, this means deviations in the exponential increasing transition regime are larger compared to the ion saturation
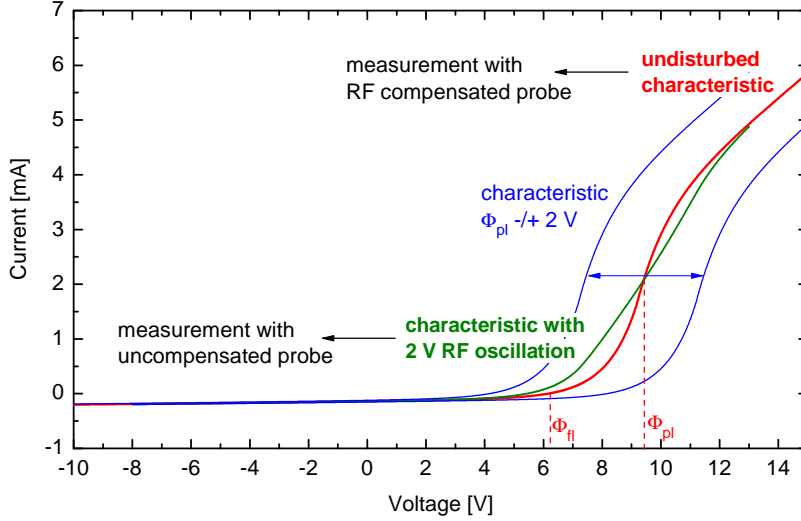
Figure 3.10: *Simulation of an erroneous probe characteristic if no RF compens-ation is done. Red: undisturbed characteristic from measurement with an RF compensated probe. Green: calculated characteristic of an uncompensated probe for an oscillating plasma potential with 2 V amplitude.*

region. As an example, the difference in the evaluation of the undisturbed and disturbed characteristic plotted in figure 3.10 is listed in table 3.5.

As expected, no deviation is found for the evaluated positive ion density $n_{i+,\text{OML}}$ (the reason, why the OML theory is used for the determination of the positive ion density will be discussed later). The error in the determination of the floating and plasma potential is 12% and 16%, respectively – the latter resulting in a large error of the determined electron density of 60%. Surprisingly, no deviation is found for the determined electron temperature – although the electron energy probability function (EEPF) is heavily disturbed in particular in the low-energy part, a fit of the higher energetic part delivers the same temperature. This is, however, only possible for strictly Maxwellian distributed electron energies.

Concluding, for determination of the plasma or floating potential, RF-compensation is necessary, if the oscillation amplitude of the plasma potential is significant compared to the electron temperature – this is the case at the prototype source, where the amplitude A has been determined to be at about 2 V in the extended boundary layer and thus $A/(\frac{k_b}{e}T_e) \approx 2$. A common used method is a passive compensation [73] by using a compensation electrode: the compensation electrode must be located close to the probe tip with an area much larger than the probe tip and is floating in the plasma. Thus, its potential is following the RF

Table 3.5: *Determined parameters from the undisturbed characteristic and the simulated characteristic containing 2 V RF oscillations (figure 3.10).*

Parameter	Characteristic with RF oscillations	Undisturbed characteristic	Difference
Φ_{fl}	5.4 V	6.2 V	12%
Φ_{pl}	10.9 V	9.4 V	16%
$n_{\text{i+,OML}}$	2.8×10^{16} m^{-3}	2.8×10^{16} m^{-3}	0%
n_{e}	4.0×10^{16} m^{-3}	2.5×10^{16} m^{-3}	60%
T_{e}	1.0 eV	1.0 eV	0%

oscillations. By passively coupling the reference electrode to the probe tip via a transformer one can achieve that the voltage difference between the applied voltage on the probe tip and the plasma potential is kept constant at each measurement point, hence the undisturbed characteristic is recorded.

Benchmark of the Langmuir probe evaluation theories

As discussed before, the positive ion density is used as a measure of the plasma density at the IPP test facilities. The evaluation of the positive ion density is especially required because not all Langmuir probes used at the IPP test facilities are RF compensated. In order to decide which ion collecting theory is to be used for the positive ion density evaluation and to determine the error of the measured density, a benchmark of the different ion collection theories is highly desirable in the relevant parameter range and has been carried out during this work.

An important parameter for the validity of each ion collection theory is the parameter $\xi \equiv r_{\text{P}}/\lambda_{\text{D}}$, defining the radius of the probe tip r_{p} in comparison to the thickness of the sheath – as mentioned in section 2.4, the typical sheath thickness is in the order of the Debye lengths λ_{D}. This value describes in theory whether particle orbiting has to be taken into account (at a thick sheath in comparison to the probe tip radius and thus small values of ξ) or not. So from theory point of view, the validity of the OML theory (taking only orbital motion into account) should be best for small values of ξ, whereas the validity of the ABR theory (neglecting orbital motion) should be best for large values of ξ.

The benchmark has been carried out in a planar ICP lab experiment (the experiment is described in detail in [74, 49]), with no magnetic field applied and by usage of an RF compensated Langmuir probe. In order to benchmark the

Table 3.6: *Parameter range used for the probe benchmark at a lab ICP experiment.*

Gas	RF power	Probe radius	Gas pressure
Ar	100 W	25 μm	4–13 Pa
He	100 W	25 μm	8–18 Pa
He	250 W	25 μm	5–18 Pa
He	100 W	150 μm	8–18 Pa
H$_2$	250 W	150 μm	5–15 Pa

theories at a large range of ξ, a multitude of discharges with several working gases, several applied RF powers, several gas pressures as well as several probe tip diameters have been used as listed in table 3.6. The most relevant case is 'H$_2$, 250 W', because the resulting value of ξ matches best the value in the prototype ion source, what will be shown in figures 3.11 and 3.12.

The result of the benchmark is shown in figure 3.11, in which as a measure for the quality of each ion collecting theory the density ratio between the positive ion density determined by each ion collecting theory and the electron density evaluated from the I–V-trace, n_{i+}/n_e, is plotted against ξ. The reason for the normalization on n_e is that a comparison of n_e measured with a Langmuir probe against an interferometric determined electron density (which reveals a line-of-sight integrated density at high accuracy) for some selected parameters showed good agreement in the same lab experiment [75]. For this reason, n_e is also used for the calculation of ξ at each measurement point. Two main observations are:

1. The quantity ξ sorts each ion collection theory to a certain curve. This is in agreement with the expected behavior, namely that the quality of agreement of each ion collection theory depends mainly only on ξ.

2. Almost all data points exceed a deviation of several 10% to the electron density, thus the error of the determined positive ion density is significant in most cases. However, the difference between the theories is much larger at low values of $\xi \lesssim 2$ (discrepancy of up to a factor of 22), compared to higher values of $\xi \gtrsim 2$ (discrepancy below a factor of two).

This leads to the conclusion that (a) for the evaluation of positive ion densities a value of $\xi \gtrsim 2$ is beneficial. Because the behavior of $\xi > 3.3$ has not been investigated and extrapolation over a large range is not reasonable, this results in
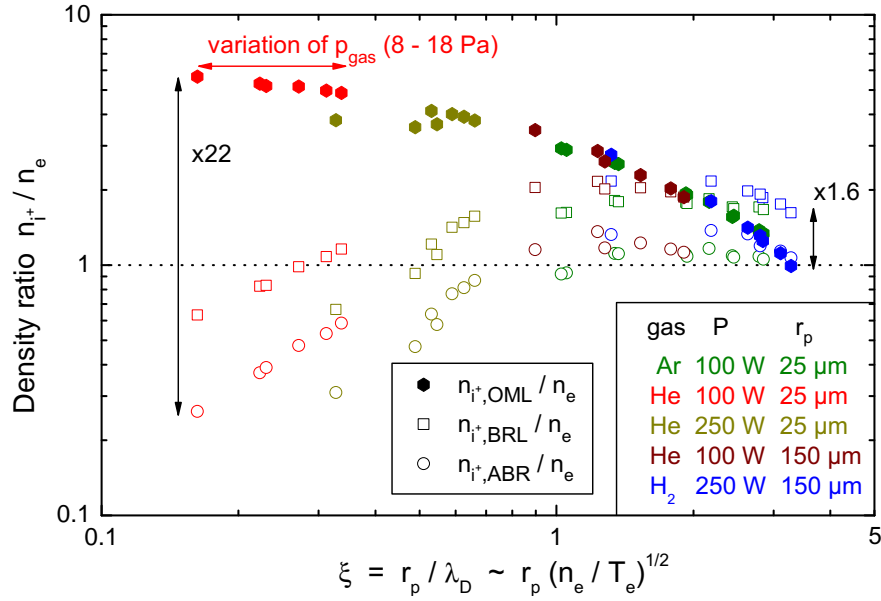
Figure 3.11: *Dependence of the ratio between the positive ion and electron density for OML, BRL and ABR ion collecting theory. Varying parameters are working gas, gas pressure, discharge power and probe tip radius.*

the estimated requirement of $2 \lesssim \xi \lesssim 5$. In addition, if positive ion densities are compared for different probes, their value of ξ should be similar (b).

Calculated values of ξ are shown in figure 3.12 for typical parameters inside the extended boundary layer of the IPP prototype source ($T_e = 1$ eV, $n_e = 0.5$–3×10^{17} m^{-3}) and two different probe tip radii typically used for the probes at the IPP test facilities. In order to fulfill the requirement (a) and (b), it is beneficial to use a thicker probe tip at a position with lower plasma density (close to the side wall), whereas more inside a thinner tip diameter should be used in order to achieve a beneficial value of ξ.

For the determination of the positive ion density during this work, the OML theory has been chosen because it agrees well with the electron density in the required range of ξ and additionally the electron temperature is not required in the calculation, leading to a more robust evaluation.

Influence of negative hydrogen ions

So far, only electrons have been considered as negatively charged particle species, but also H$^-$ has to be taken into account at the prototype ion source. The influence of H$^-$ particles on the measured characteristic strongly depends on the
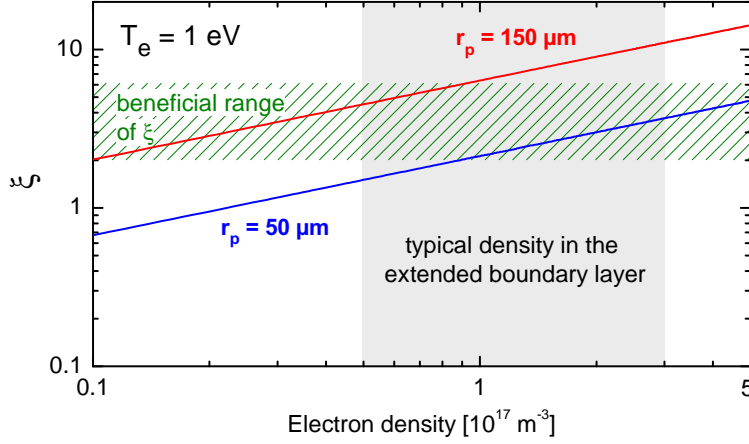
Figure 3.12: *Value of ξ inside the extended boundary layer for two different probe tip radii as a function of the electron density.*

amount of the H^- particle density compared to the electron density n_{H^-}/n_e. The current on the probe tip at the plasma potential, where no sheath establishes, is

$$I(\Phi_{pl}) = A_p e \left(\Gamma_e + \Gamma_{H^-} - \Gamma_{i+}\right). \tag{3.16}$$

Since $\Gamma_j \propto n_j \sqrt{T_j/m_j}$ for species j, the flux of the much heavier negative ions compared to the electron flux has only to be taken into account, if

$$\begin{aligned}
n_{H^-}/n_e &\gtrsim \sqrt{m_{H^-}/m_e} \approx 43, \\
n_{D^-}/n_e &\gtrsim \sqrt{m_{D^-}/m_e} \approx 61,
\end{aligned} \tag{3.17}$$

for similar particle temperatures. However, one should keep in mind that due to the quasi-neutrality, the electron density is reduced for an increasing H^- fraction at constant positive ion density, leading to a reduced electron current onto the probe, even if the condition (3.17) is not fulfilled. Due to the similar temperature of H^- and electrons in the extended boundary layer (see table 2.3), two cases can be defined:

1. $n_{H^-}/n_e \ll 43$ or $n_{D^-}/n_e \ll 61$, respectively:
   the current on the probe tip is dominated by the electrons and is decreasing for increasing H^- fraction in order to sustain quasi-neutrality. The I–V-trace of the Langmuir probe shows its classical shape.

2. $n_{H^-}/n_e \gg 43$ or $n_{D^-}/n_e \gg 61$, respectively:
   the electron current gets negligible, an ion–ion plasma is formed. Due

to the similar mass of positive and negative hydrogen ions, the measured characteristic becomes symmetric [76, 77] and the net current onto the probe at the plasma potential is almost zero. This means, a symmetric characteristic is a strong hint for negative hydrogen ions being the dominant negatively charged particle species in the extended boundary layer of the prototype source [78, 79].

In the IPP prototype source, a change from the first case to the second case happens during the Cs conditioning process, in which a transition from volume to surface dominated production of H$^-$ takes place: while at the beginning of the conditioning process, the amount of surface produced H$^-$ particles is low and thus electrons dominate the particle fluxes onto the probe, the increasing fraction of H$^-$ particles leads to transition to the second case – however, as will be shown in section 5.3, this transition is only to be seen in the extended boundary layer close to the side wall, where the positive ion density is lower (typically $n_{i+} \lesssim 10^{17}$ m^{-3}) compared to the center plasma (typically $n_{i+} \approx$ 3–5 $\times 10^{17}$ m^{-3}) at an axial distance of 0.7 cm to the plasma grid.

Applied probe evaluation

To summarize, the following method has been chosen for the probe evaluation and has been implemented in an automatic routine in a LabView program created during this work – a screenshot is shown in figure 3.13:

1. The potentials Φ_{fl} and Φ_{pl} are determined. For this purpose, the characteristic is smoothed by a Savitzky–Golay filter to reduce signal noise.

2. For the determination of the positive ion density, a fit of the OML theory (equation (3.15)) is performed. The fitting range is chosen from the most negative applied voltage (-30 V) to some volts (typically 10 V) below the floating potential.

3. The ion current determined in step 2 is then subtracted from the total measured current. A linear fit of the logarithmized electron starting current (equation (3.14)) in the voltage range with sufficient signal-to-noise ratio yields the electron temperature.

For the determination of the electron temperature it is of importance whether the electron energy distribution is strictly Maxwellian (in this case the determined
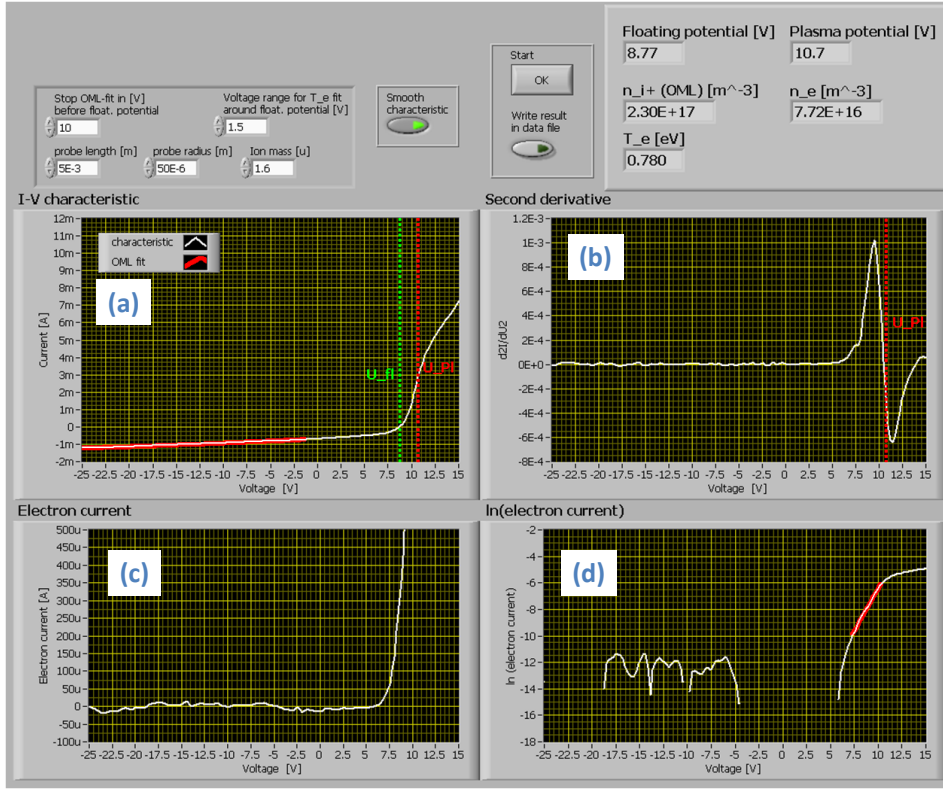
Figure 3.13: *Screenshot of the LabView program for the probe characteristic evaluation: (a) measured characteristic and OML ion current fit, (b) second derivative for determination of the plasma potential, (c) electron current and (d) natural logarithm of the electron current for electron temperature determination.*

electron temperature is valid for all electrons) or whether there are deviations from a Maxwellian distribution. Deviations can develop as example if strong loss channels in a certain energy range exist – e.g. vibrational excitation of H_2 leads to an underpopulation of electrons in the energy range of about 2–4 eV and a subsequent overpopulation of electrons with energy < 1 eV. Since electrons are repelled from the probe tip for applied voltages below the plasma potential, the electron current is linked to the electron energy probability function of electrons. As shown in figure 3.13 (d), the linear fit of the logarithmized electron current is possible in the energy range 1 eV $\lesssim E \lesssim$ 4 eV – being in the regime, where a underpopulation can take place. Obviously, vibrational excitation energies are dependent on the nucleus mass, leading to an isotope difference between H_2 and D_2. For this reason, small deviations in the determined electron temperature between hydrogen and deuterium can be caused by this 'vibrational dip' in the energy distribution and must not necessarily attributed to the electron energy distribution of the total ensemble.

Influence of the effective positive ion mass

Since the plasma consists of several positive ion species, the OML ion current (equation (3.15)) is a sum of the current of each species j:

$$I_{i+} = \sum_j \left(A_p n_{i+,j} e \frac{\sqrt{2}}{\pi} \sqrt{\frac{e(\Phi_{pl,1} - U)}{m_{i+,,j}}} \right) \equiv A_p n_{i+} e \frac{\sqrt{2}}{\pi} \sqrt{\frac{e(\Phi_{pl,1} - U)}{m_{i+,\text{eff}}}}, \quad (3.18)$$

with the mass of each positive ion species $m_{i+,j}$ and the effective positive ion mass $m_{i+,\text{eff}}$, defined as

$$\frac{1}{\sqrt{m_{i+,\text{eff}}}} = \sum_j f_j \frac{1}{\sqrt{m_{i+,j}}}, \quad (3.19)$$

f_j denoting the fraction of each positive ion species. As already discussed in section 2.5, the positive hydrogen ion distribution is assumed to be 40% H^+, 40% H_2^+ and 20% H_3^+, leading to an effective mass of 1.6 u in H_2 and 3.1 u in D_2 operation.

Additionally, also positive caesium ions contribute to the effective ion mass. Hence, for the determination of the total positive ion density, the amount of Cs^+ is required. A factor of roughly 30 times larger Cs^+ density compared to Cs^0 is estimated in [41] by comparison of emission from Cs atoms and ions. Calculation with a typical Cs^0 density of 1×10^{15} m^{-3} results in $n_{Cs+} \approx 3 \times 10^{16}$ m^{-3}, which is about 10% of the positive ion density in the extended boundary layer in front of the plasma grid (compare to section 2.5). The effective mass is then slightly increased to a value of 1.9 in H_2 and 3.7 in D_2. The difference in the resulting positive ion densities is small (below 10%) due to the small difference of the effective ion mass as well as the ion current being only weakly dependent on $(m_{i+,\text{eff}})^{-1/2}$. Thus, the influence of Cs^+ ions is neglected in the evaluation further on.

Setup at the prototype source

Two Langmuir probes have been installed at BATMAN, as shown in figure 3.14: one horizontally moveable, passively RF-compensated probe and one non-compensated probe at a fixed position. The movement of the probe is realized by usage of a stepper motor.

The mechanical design of the moveable probe as well as the applied
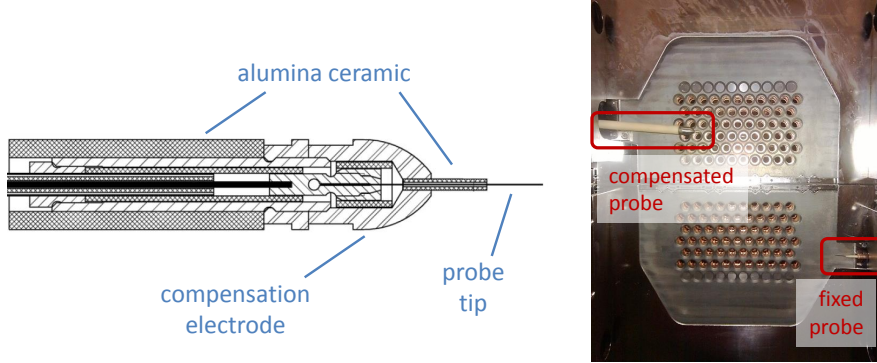
Figure 3.14: *Left: drawing of the moveable, compensated Langmuir probe. Right: picture of both probes installed at BATMAN.*

PlasmaMeter[23] control and data acquisition system is described in detail in [38]. Since the fixed probe is located close to the side wall, where the plasma density is lower compared to the center, it is equipped with a thicker and longer probe tip (150 μm radius, 1 cm length) in order to enlarge the drawn electrical current and to use a beneficial value of ξ, as was shown in figure 3.12. For the compensated probe a tip with 5 mm length and a radius of 50 μm is used.

Error estimation

The error range of each determined quantity is estimated as follows:

- n_{i+}: systematic errors in the determination occur due to an uncertainty in the probe area ($\pm 10\%$) as well as in the effective ion mass ($\pm 20\%$), leading to a total error of $\pm 20\%$. In addition, the applicability of the OML theory has to be taken into account – as shown in figure 3.11, the error of the evaluated positive ion density can be large even in the range of $2 \lesssim \xi \lesssim 5$. However, for parameter studies, measurements at the same position are compared. Since the electron temperature T_e is almost constant (as long as the magnetic filter field is not changed, which has not been done during this work) and because $\xi \propto 1/\lambda_D \propto \sqrt{n_e/T_e}$ is only weakly dependent on n_e, the relative error in comparison studies is lower compared to the absolute deviation.

- T_e: the error of the evaluated electron temperature depends on the quality of the linear fit of the logarithmized exponential electron starting current

---

[23]PlasmaMeter version 5.3, developed at the School of Physics and Technology of the Kharkov National University, Ukraine

and is estimated to be $\pm 20\%$. As previously discussed, also the electron energy range in which the determination of T_e is possible has to be taken into account.

- Φ_{pl}: the error range of the plasma potential is chosen as the potential difference between the maximum and the minimum of the second derivative of the measured current. This results in ± 1 V for the RF compensated probe and ± 2 V for the non RF compensated probe.

3.4 Optical emission spectroscopy

By means of Optical Emission Spectroscopy (OES) the line-of-sight integrated light emission out of the plasma is investigated. Although no detailed evaluation of OES measurements has been carried our during this work, a brief overview is given within this section since measurement results from this work will be compared to former OES measurements from [35].

Spectrometers, optics and a detector with an accessible wavelength range of the extended visible light (e.g. 250–900 nm) are used for a wavelength resolved measurement of the plasma emission. There are two modes of operation at the IPP prototype source:

- As a routine diagnostic, OES is used for monitoring the plasma stability or for the identification of impurities. For this purpose, no information of the absolute light emission is necessary. In addition to a spectroscopic system, also photo diodes are used with a faster temporal resolution of several 100 Hz after amplification. An interference filter in front of the photo diodes narrows the detected wavelength range at the desired transition (e.g. a filter with central wavelength of 852 nm and $\Delta\lambda_{FWHM} = 10$ nm is used to monitor the Cs 852 nm emission).

- OES is also used for the evaluation of plasma parameters of selected pulses. For this purpose, the measurement setup (window, optical head, fibers and the spectrometer itself) has to be absolutely calibrated what is done at the IPP test facilities by means of a calibrated Ulbricht sphere, which produces perfect diffuse light at known wavelength-dependent intensity.

The line emissivity ϵ_{ik} [photons $\cdot$ m^{-3}s^{-1}] of an optical transition from an excited upper state i to a lower state k can then be derived out of the measured absolute

intensity $I(\lambda)$ by

$$\epsilon_{ik} = \int_{\lambda_1}^{\lambda_2} I(\lambda)\mathrm{d}\lambda. \tag{3.20}$$

The transition probability (Einstein coefficient for spontaneous emission A_{ik}) yields the particle density n_i in the upper state i:

$$\epsilon_{ik} = n_i A_{ik}. \tag{3.21}$$

For the evaluation of the density in the ground state or plasma parameters as the electron density or temperature, models have to be applied which determine the population and depopulation of the upper states in sufficient precision as a function of the plasma parameters. A state can be populated or depopulated by many different excitation or de-excitation processes, e.g. by collisions with electrons, by photon absorption or emission, dissociative excitation for molecules and many more. Also ionization and recombination processes have to be considered; beside volume recombination the recombination at the wall can play an important role. Three cases can be classified in dependence of the electron density:

- $n_e \gtrsim 10^{24}$ m^{-3} :
  At high electron densities, a local thermal equilibrium establishes, where each excitation process is in equilibrium with its de-excitation process – with the exception of processes in which photons are involved, since photons can have long mean free paths. The population of excited states follows the Boltzmann distribution in this case – in contrary, Planck's law for the description of the emitted radiation is usually not fulfilled.

- $n_e \lesssim 10^{16}$ m^{-3} :
  For low electron densities, a so-called corona model can be applied, if excitation processes by heavy particle collisions are neglegible: due to the low density, excited states are solely excited by electron collision from the ground state and de-excited solely by spontaneous emission. Balancing of these two processes yields the rate equation:

$$n_0 n_e X_{0i}(T_e) = n_i \sum_{k<i} A_{ik}, \tag{3.22}$$

with n_0 denoting the ground state density (which is equal to the particle density of the species in this case) and $X_{0i}(T_e)$ the excitation rate coefficient for electron collision excitation from the ground state 0 to the excited state i.

- 10^{16} m$^{-3} \lesssim n_e \lesssim 10^{24}$ m^{-3}:

  The electron density in the IPP prototype source is in between the validity of these two models; in this regime so called collisional radiative models need to be applied. In a collisional radiative model, the relevant excitation and de-excitation processes are included for the relevant particle species.

  A collisional radiative model for H and H$_2$ based on the flexible solver `Yacora` [80] is applied at the IPP neutral beam test facilities for quantitative evaluation of OES measurements [81], giving access to a multitude of plasma parameters. An overview is given in [41].

The lines of sight at the prototype ion source have a diameter of 1 cm, which is defined by the collimator optics in combination with the used optical fiber. The optical fibers have an enhanced UV transmission, enabling also measurements at low wavelengths in the near UV. At the LOS in the extended boundary layer, which will be shown in figure 3.15, either a photo diode with interference filter is attached, or a survey spectrometer[24] is used, which creates automatically a time trace of several emission lines for each pulse with a temporal resolution of 150 ms. In this work, only the emissivity of certain emission lines will be shown for comparison with other diagnostics in the extended boundary layer. In general, the measured emissivity ϵ_{ik} is linked to the density of the particular particle species, electron density and effective emission rate coefficient $X_{ik,\text{eff}}^{\text{em}}(T_e, n_e, ...)$:

$$\epsilon_{ik} = n_0 n_e X_{ik,\text{eff}}^{\text{em}}(T_e, n_e, ...). \tag{3.23}$$

Thus, the Cs line emission at 852 nm scales with the Cs density. In the same way, the Balmer line emission of hydrogen atoms, as H$_\beta$ (486 nm for H) or H$_\gamma$ (434 nm for H) scales with n_H. The emission of the Fulcher system of hydrogen molecules (between 590 nm and 650 nm), which consists of multiple lines based on a electronic transition split by their vibrational and rotational levels, scales with n_{H_2}. Hence, the ratio between the H$_\beta$ or H$_\gamma$ emission and the Fulcher emission scales with the density ratio n_H/n_{H_2} for constant plasma parameters.

---

[24]PLASUS EmiCon system, wavelength range 200–870 nm, wavelength resolution 400 pm per pixel

For the production of negative hydrogen ions in the IPP prototype source, the flux of dissociated hydrogen ions and atoms towards the plasma grid is an important parameter, since the flux of surface produced H^- into the plasma directly depends on it, as long as no limitation due to space charge effects occurs (see section 2.4). As the dissociation mainly takes place in the driver, a detailed characterization of the driver plasma including the determination of the density ratio n_H/n_{H_2} is desirable. This has been carried out at an axial LOS through the driver towards the plasma grid in the past [35]. Due to the higher plasma density and temperature, the line-of-sight integrated emission of this LOS is dominated by the driver emission.

3.5 Measurement positions and timing at BATMAN

Most measurements during this work have been carried out at the BATMAN short-pulse test facility. At the MANITU long-pulse testbed, Cs dynamics measurements have been performed for long pulse studies. The experimental setup at BATMAN is introduced in this section, followed by the setup at MANITU in section 3.6. As already shown in figure 3.1, a limited amount of diagnostic ports is available at the prototype ion sources.

Two different diagnostic setups have been used at BATMAN, both are shown in figure 3.15: setup (a) consists of multiple diagnostics for simultaneous measurement of several parameters inside the extended boundary layer. The measurement quantities and their position are listed in table 3.7.

For Cs-ABS, a vertical LOS has been chosen for determination of the Cs^0 density averaged over a long (60 cm) LOS, beneficial for comparison with the extracted currents, which are averaged over the large area of all extraction apertures. For comparison, a similar vertical LOS is used for the measurement of the Cs 852 nm emission during plasma phases using a photo diode with an interference filter.

For the CRDS, a vertically centered, horizontal line of sight is used in contrary to previous measurements [61, 37], where the CRDS has been installed at a horizontal LOS in the top part of the source. Since the vertical centered LOS is located in front of the plasma grid (axial distance 2.2 cm) in contrary to the position in front of the bias plate of the top LOS, a more direct correlation to the source performance is expected at this position – although no extraction apertures exist in the vertical center of the source. The same length of the LOS as in the
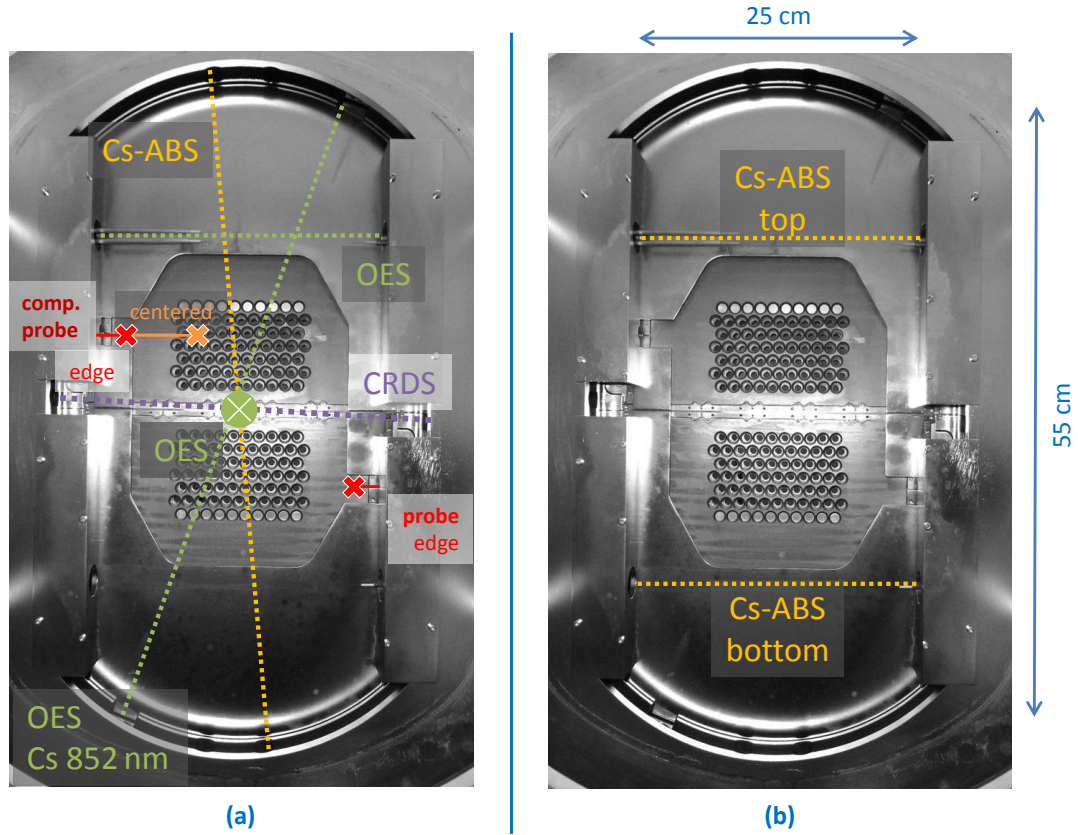
Figure 3.15: *Sketch of the two used diagnostic setups at BATMAN (view from the driver onto the plasma grid): (a) for simultaneous measurement of multiple parameters inside the extended boundary layer, (b) for determination of the Cs^0 density at two LOS.*

Table 3.7: *Measurement quantities and measurement position at BATMAN for the setup shown in figure 3.15 (a).*

Measurement quantity	Measurement position	Ax. dist. to PG	Temporal resolution	Diagnostic
n_{Cs^0}	vertical LOS	2.2 cm	40 Hz	Cs-ABS
$\epsilon_{Cs852nm}$	vertical LOS	2.2 cm	1 kHz	OES
n_{H^-}	centr. horizontal LOS	2.2 cm	6 Hz	CRDS
Φ_{pl}, n_{i^+}, T_e	top edge & centered, bottom edge	0.7 cm	one measurement per pulse	Langmuir probe
ϵ_{H_β}	top horizontal LOS	2.2 cm	7 Hz	OES
$n_H/n_{H_2}, T_e, n_e$ from [35]	centered axial LOS	n.a.	one measurement per pulse	OES

past (25 cm) is considered in the calculation of the H^- particle density due to the slight vertical tilting of the LOS and to be comparable with former CRDS measurements.

Two Langmuir probes are installed at horizontal ports with an axial distance of 0.7 cm to the plasma grid. The moveable probe is configured to measure at two positions during each BATMAN pulse: the edge position uses the same horizontal distance to the center as the fixed probe and is chosen in order to determine the vertical plasma symmetry. At the centered position, plasma parameters more relevant to the source performance in front of the plasma grid apertures are determined.

For additional determination of the vertical plasma symmetry, one horizontal LOS (20 cm plasma length) in the top part is used for the OES, at which the emissivity of H_β is measured. Since only one horizontal LOS is used, the vertical symmetry can only be determined by change of the magnetic filter field direction (as mentioned in section 2.5, change of the filter field direction changes symmetrically the vertical plasma distribution in the source). Comparison is then possible with the plasma symmetry measured by the Langmuir probes.

One centered, axial LOS has been used for the optical emission spectroscopy in the past [35] in order to characterize the plasma inside the driver. Regularly, also a photo diode with interference filter is attached to this LOS for measurement of the H_α emission and thus for monitoring the plasma stability with a high temporal resolution (200 Hz).

In contrary to the possibility of a detailed plasma characterization in setup 3.15 (a), setup (b) offers the possibility of determining the Cs^0 density with some vertical resolution at two horizontal LOS (axial distance to PG: 2.2 cm) in the top and bottom part of the source. The vertical resolution is of particular interest since the source has an intrinsic Cs inhomogeneity with the Cs oven mounted in the top part.

Timing of a BATMAN pulse

As already mentioned, BATMAN is a pulsed test facility with typically a plasma time of 6 s, including 4 s beam extraction, and a vacuum phase of 200 s between two pulses. The temporal characteristic of a pulse is plotted in figure 3.16, showing the applied RF power and source pressure (a), the applied extraction voltage and the extracted currents (b), the emission of H_α in the driver (c), the H^- particle density (d) and the Cs^0 density (e).
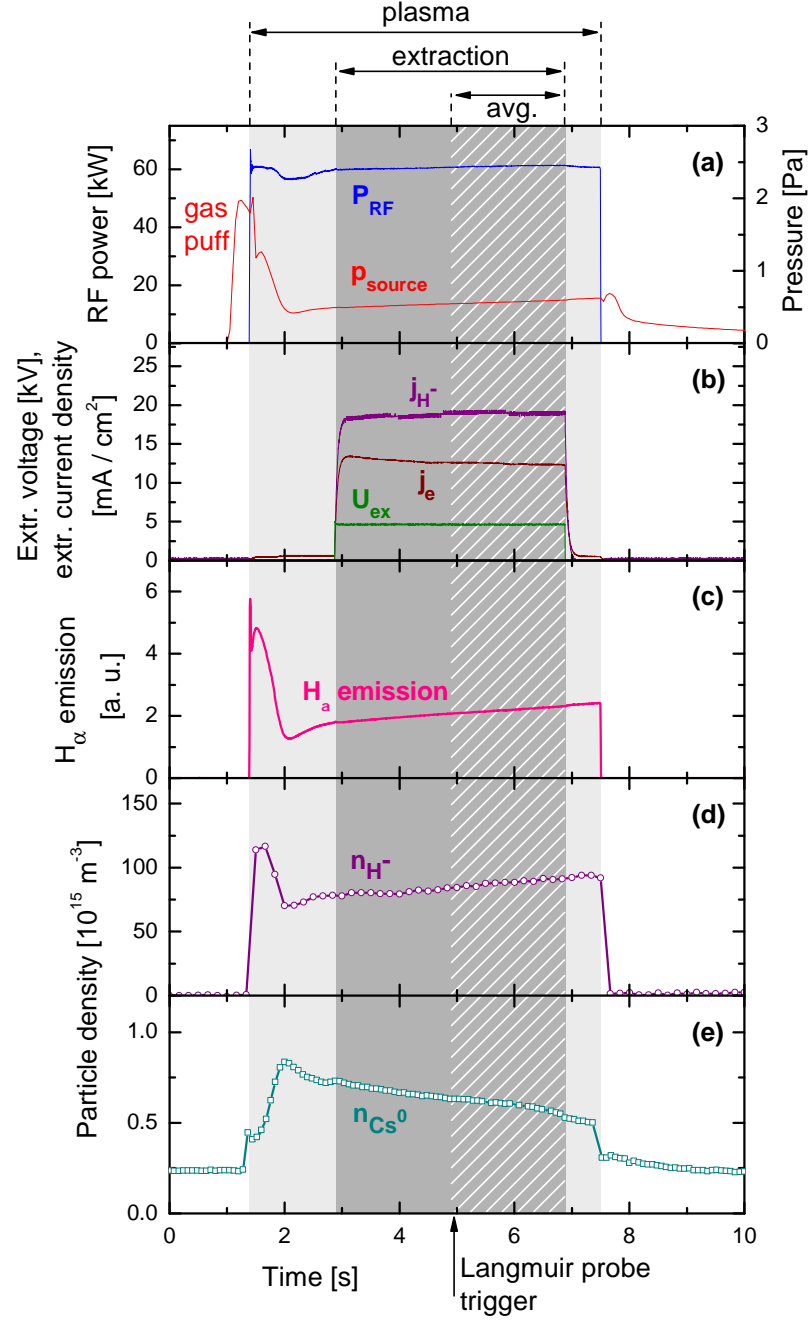
Figure 3.16: *Temporal characteristics of a BATMAN pulse: (a) applied RF power and source pressure, (b) applied extraction voltage and extracted H^- and electron current density, (c) H_α emission in the driver, (d) H^- density and (e) neutral Cs density.*

The main trigger event for most diagnostics occurs by definition at $t = 0$ s. A hydrogen gas puff is required for plasma ignition, for this reason the gas valve is opened after several 100 ms. The RF generator is turned on at the time close to the maximum of the gas puff. The gas flow is reduced after plasma ignition to a value at which the desired source pressure establishes. High voltage for extraction is applied after a plasma time of 1.5 s, where the discharge parameters are stable, for a duration of 4 s. After the extraction phase, the RF generator is turned off after an additional time period of 0.6 s – this additional plasma time is useful for investigating the influence of the extraction phase. The gas flow is stopped 0.2 s after the end of the plasma phase; the source pressure is then decreasing in the following seconds to the vacuum level (about 1×10^{-6} mbar).

Since the pulses are short, the operational parameters (RF power, bias voltage etc.) are kept constant during one pulse. This means that for parameter comparison studies, several pulses have to be compared. For this reason, averaging of the time traces is done for each shot. The time period of the second half of the extraction phase is chosen for the averaging, because the source operates usually stable during this phase – beside effects based on the slightly increasing source pressure.

The Langmuir probes are triggered one time each shot in the middle of the extraction phase. The fixed probe records then one characteristic, whereas the moveable probe moves from its parking position outside of the expansion chamber to the edge position where one characteristic is recorded. Afterward it moves to the centered position, where again one characteristic is recorded. At the end, it moves back to the parking position outside the chamber. The whole procedure takes about 1 s, thus all measurements take place within the second half of the extraction phase.

3.6 Measurement positions at MANITU

The MANITU long pulse test facility has been in operation during the first months of this thesis work and was shut down in favor of the construction of ELISE in summer 2011. MANITU was capable for plasma and beam pulses with a length of up to one hour; however, the typical pulse length has been in the range of 20–200 s. The vacuum phase between two pulses had the same length compared to BATMAN (typically 200 s).
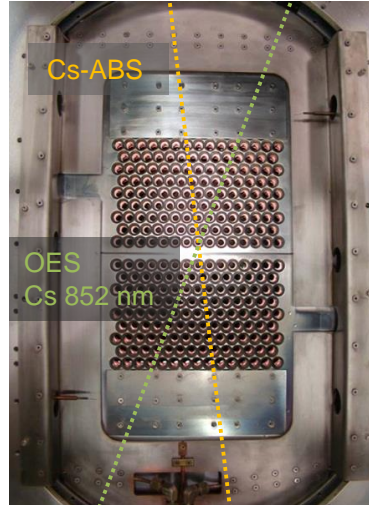
Figure 3.17: *Diagnostic setup for the measurement of the Cs dynamics at MAN-ITU.*

Cs dynamics measurements have been carried out at MANITU using Cs-ABS, since the comparison of short to long pulses is of high relevance for the development of the ITER H$^-$ source. However, the Cs absorption spectroscopy has been only available at one LOS during this time. Due to the limited available time for measurements at MANITU until its shutdown and due to severe problems with RF noise disturbing the Cs-ABS, measurements have been possible only at a very limited amount of operational days. The same vertical LOS as in the BATMAN setup (figure 3.15 (a)) with a length of 60 cm and a distance of 2.2 cm to the plasma grid has been used, as shown in figure 3.17. For comparison with OES, the same LOS as in BATMAN (length 60 cm, distance to PG 2.2 cm) was equipped with a photo diode and an interference filter for determination of the Cs 852 nm emission.

4 Experimental investigation of the Cs dynamics

Beside the experimental experience, the present understanding of the Cs dynamics and its influence on the operation of the source has been discussed in section 2.6. Three main questions, which are significant for the operation of the large-scale ITER H$^-$ source, have been experimentally addressed during this work:

- Does the source performance correlate with the measured Cs density and what controls the optimum Cs evaporation rate into the source?

- Is homogeneous evaporation of Cs into the source required?

- How is the Cs dynamics affected by the duty cycle between plasma and vacuum pulses?

The Cs dynamics has been investigated during short and long pulse operation at BATMAN and MANITU. Due to the large influence of the plasma phases on the Cs redistribution, a different behavior is expected for different plasma/vacuum duty cycles. The main diagnostic method for the investigation of the Cs dynamics is the Cs absorption spectroscopy, being capable of determining the neutral Cs density during vacuum and plasma phases. The measurements have been accompanied by OES, at which the Cs emission is recorded by a photo diode due to the higher temporal resolution. The plasma stability has been monitored by the H$_\beta$ emission – the latter is not shown in this chapter.

4.1 BATMAN: Cs dynamics in short pulse operation

The investigations at BATMAN mainly concentrate on the basic understanding of the Cs dynamics during vacuum and plasma phases and consequently the first two items mentioned above are addressed.

4.1.1 Determination of Cs evaporation using optical diagnostics

As mentioned in chapter 2.6, the liquid Cs oven is not equipped with a Surface Ionization Detector (SID), so the evaporation rate of the oven can not be directly measured – although a rough calibration of the evaporation rate dependent on the oven body temperature has been carried out in the past [48, 82]. However, the determination of Cs evaporation at all as well as the evaporation rate is very desirable for the control and operation of the oven, especially if specific events, such as a run-out of the liquid Cs reservoir or a burst in the Cs evaporation rate, happen.

Shown in figure 4.1 is a comparison of Cs^0 signals for one day of operation, at which the liquid Cs reservoir inside the oven depleted. Plotted in the top part is the neutral Cs density measured by Cs-ABS during plasma phases as well as the Cs 852 nm emission, both diagnostics attached to similar vertical lines of sight (each data point refers to one plasma pulse). In the bottom part the neutral Cs density in the vacuum phase, 1 s before a plasma pulse, is shown in combination with the body temperature of the Cs oven. During this day, the position and direction of the magnetic filter field has been changed several times, which has also an effect on the Cs density during plasma phases due to changes in the plasma distribution within the expansion chamber (the effect of the latter on the Cs distribution will be shown later in figure 5.12). Furthermore, as will be shown in section 4.1.3, the Cs density in the plasma phase is not dominated by the particular Cs evaporation rate, but by redistribution processes of Cs within the expansion volume.

The Cs 852 nm emission agrees well with the Cs^0 density measured by absorption. Slight deviations occur since the Cs 852 nm emission is not only dependent on the Cs density, but also on the plasma parameters (compare to equation (3.23)), which change with varying magnetic filter field topology.

A strong de-coupling of the Cs signals during plasma phases to the vacuum Cs density takes place: the Cs density during vacuum phases is dominated by the Cs evaporation rate in combination with sticking of Cs at the source wall. The density is stable until 13:30. Because the temperature of the Cs oven has not been changed, the Cs evaporation rate is expected to be stable. Afterwards, a run-out of the Cs oven can be clearly seen by a instantaneous fast decrease of the vacuum Cs density below the detection threshold, which is about 1×10^{14} m^{-3}. In contrast, no clear trend is seen in the plasma signals. This behavior shows that
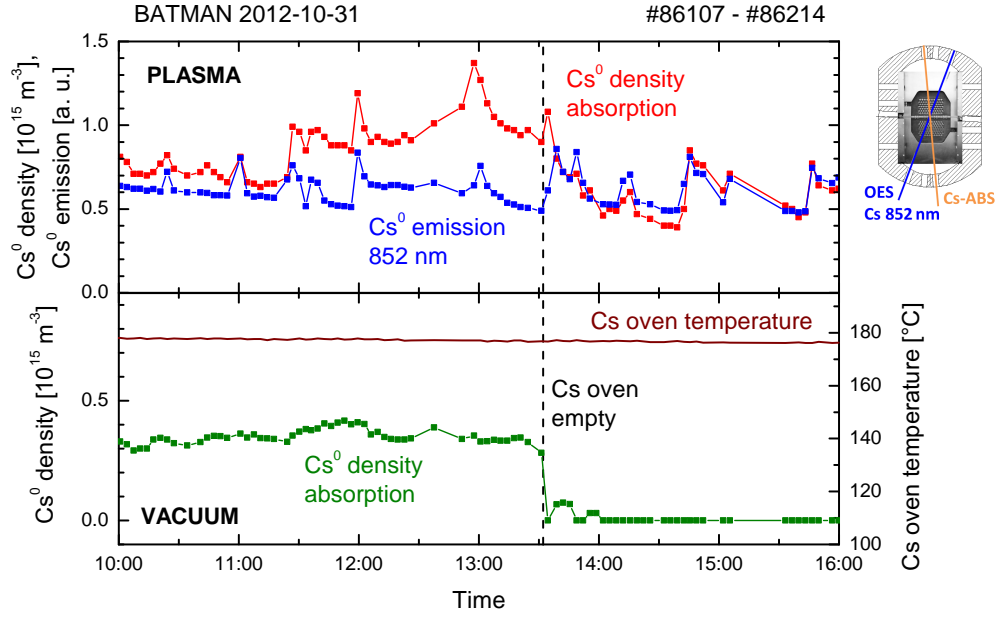
Figure 4.1: *Cs signals for one day of operation at which the Cs reservoir inside the oven depleted. Top: Cs^0 density as well as Cs 852 nm emission during plasma phases. Bottom: Cs^0 density in the vacuum phase (1 s before each pulse) and Cs oven temperature.*

monitoring of the Cs evaporation rate is possible by determination of the vacuum Cs density – however, not by plasma signals, because redistribution of Cs from reservoirs at the source wall takes place during plasma phases, which superpose the flux of Cs evaporated out of the oven. A direct comparison of the vacuum Cs density on the Cs evaporation rate of the oven will be shown in figure 4.6.

4.1.2 Correlation of the Cs density with the source performance

During the Cs conditioning phase, a certain Cs flux onto the plasma grid is required in order to achieve and sustain a stable Cs layer on the plasma grid and by this a stable and low work function (see section 2.6). Because the measured Cs absorption spectra are clearly Doppler-broadened (compare to figures 3.2 and 3.3), Cs atoms are Maxwellian distributed and fluxes are thus isotropic in the measured LOS. Hence, the flux of Cs onto the plasma grid is determined by the Cs density in front of the plasma grid for a constant particle velocity distribution due to a constant particle temperature.
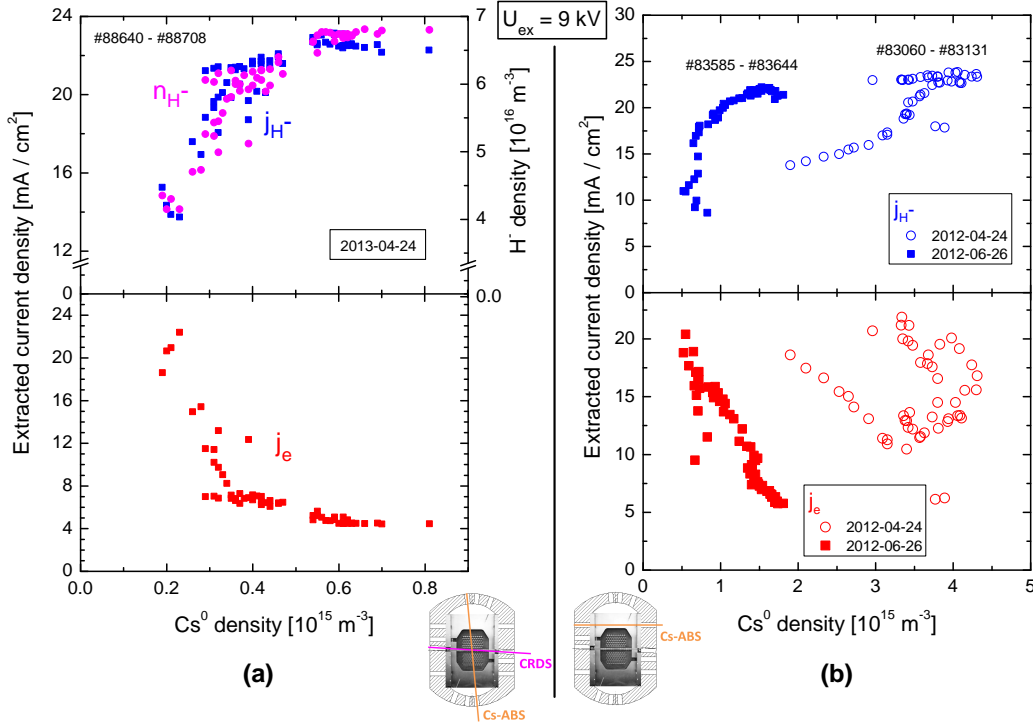
Figure 4.2: *Dependence of the source performance on the neutral Cs density in the plasma phase: (a) during one day of operation with additionally plotted H⁻ density measured by CRDS, (b) comparison of two days in different campaigns.*

The Cs absorption spectroscopy gives directly access to the neutral Cs particle density. However, during plasma phases a large fraction of Cs is ionized. Important for the work function is the total flux of Cs onto the plasma grid (ions and neutrals). In contrary to neutrals, the flux of Cs ions onto the plasma grid is dependent on the sheath potential profile at the plasma grid. However, as the density of ionized Cs is not accessible, only the dependence on the Cs^0 density can be investigated.

The dependence of the source performance (extracted H^- current density and co-extracted electron current density) on the neutral Cs density in the plasma phase for different days of operation during the Cs conditioning phase of different experimental campaigns is shown in figure 4.2. Whereas the source has been completely dismounted and cleaned, and only a little amount of Cs has been evaporated before starting the measurement campaign in (a), no cleaning was done before the campaigns shown in (b). Additionally, the different LOS of the Cs-ABS must be taken into account, with a vertical LOS in (a) and a horizontal LOS in (b).

Figure 4.2 (a) shows the dependence for one day, in combination with the H^- density determined by CRDS. The source performance (high j_{H^-}, low j_e) correlates

clearly with the Cs^0 density. In addition, n_{H^-} in the extended boundary layer in front of the plasma grid shows the same behavior as j_{H^-} (this dependency will be discussed in detail in section 5.1). However, this clear correlation does not hold at longer timescales: during the days in different experimental campaigns shown in (b), the required Cs flux for achieving high source performance differs strongly. Especially the correlation of j_e on n_{Cs^0} is much weaker pronounced at 2012-04-24.

This behavior leads to the conclusion that the present understanding that a certain flux of Cs onto the plasma grid is required for the conditioning of the source is true – however, the required amount of Cs^0 density changes at long term, making it impossible to adjust the optimum Cs evaporation rate by just measuring the neutral Cs density. In addition, the required flux of Cs seems to be lower when starting the campaign with an almost clean source. This behavior can be based on several reasons:

- For the work function of the plasma grid, the balance of incoming and desorbing Cs flux in combination with chemical reactions is of importance. However, the desorption flux of Cs from the plasma grid is not taken into account because it is not accessible with diagnostics.

- The required Cs flux may change due to a different amount of impurities inside the source. Their amount can change in different experimental campaigns due to changes in the source setup.

- The homogeneity of the Cs coverage on the plasma grid and by this the homogeneity of the Cs distribution in the source must be taken into account.

- The amount of Cs^+ is not considered. The fraction of the flux of Cs^+ reaching the plasma grid depends on the potential profile within the sheath, the latter being very sensitive on the bias setting (see section 5.2).

Nevertheless, already the short-term correlation between the Cs density during plasma phases and the source performance clearly shows that the Cs density during plasma phases, and thus the redistribution of Cs inside the source is a key parameter for maintaining a stable and low work function at the plasma grid.

The sensitivity of the source performance on the neutral Cs density changes when the source is well conditioned. The dependence of the source performance on the Cs^0 density is shown in figure 4.3 for one whole experimental campaign, corresponding to one month of operation. Two clear trends can be seen: firstly, the source performance is high at higher Cs^0 densities and subsequently higher
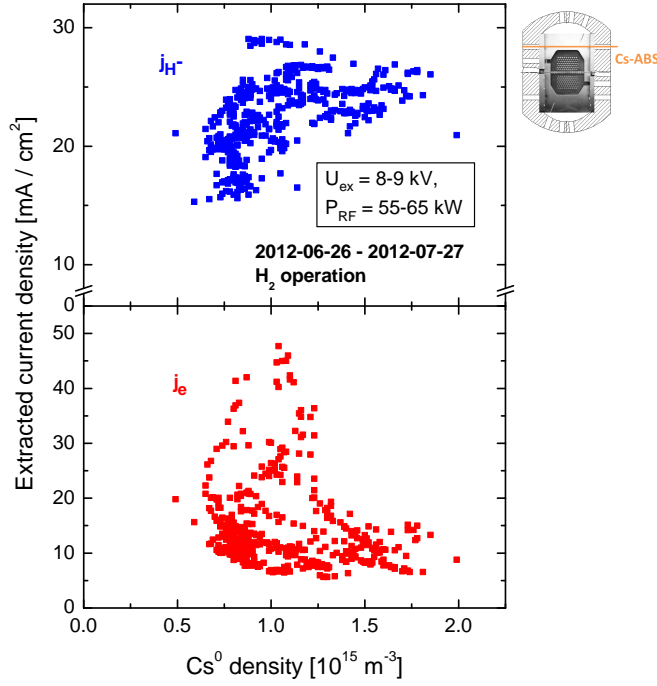
Figure 4.3: *Dependence of the source performance on the neutral Cs density during one experimental campaign, corresponding to one month of operation.*

fluxes of Cs towards the plasma grid; however, an increase of the Cs density over a certain amount ($n_{Cs^0} \gtrsim 1.3 \times 10^{15}$ m^{-3}) does not lead to a further increase of the source performance. Secondly, at lower Cs densities ($n_{Cs^0} \lesssim 1.0 \times 10^{15}$ m^{-3}) the source performance shows a wide spread.

This behavior is explained as follows: the source performance depends on the work function of the plasma grid. At higher Cs densities, the flux of Cs towards the PG is sufficiently high to achieve a homogeneous, stable and low work function – a further increase of the Cs flux may lead to a thicker Cs coverage of the PG, however to no change of the work function. For this reason, the source performance can be also high at lower Cs densities and subsequently lower fluxes of Cs towards the PG, if the source is well conditioned: at sufficient high Cs coverage of the PG, the work function and thus the source performance is less or even not dependent on the Cs flux towards the PG. However, this status cannot be maintained for a long time period; hence, a certain Cs flux is required to sustain the low work function of Cs in equilibrium with its chemical reactions at long term.

The behavior that the source performance does not significantly change at elevated Cs densities is a hint that the prototype ion source operates with the work function of bulk Cs (2.14 eV) when being good conditioned and not at

the possible lower work function for a Cs coverage below one mono layer (see section 2.2). Thus, this behavior is in good agreement with the work function measurement of a sample in a lab experiment under pulsed-plasma exposure at prototype source conditions, where the work function has been determined to be 2.2 eV [51].

4.1.3 Cs dynamics

In order to investigate the Cs dynamics in the pulsed-driven source in more detail, first a look is taken into the dynamics during a plasma pulse and the previous and following vacuum phases.

Cs dynamics during a plasma pulse

The strong difference of the Cs dynamics during vacuum and plasma phases is illustrated in figure 4.4, in which the temporal dependence of the neutral Cs density before, during and after a typical BATMAN pulse is shown in deuterium operation. Plotted is the density at two lines of sight (setup of figure 3.15 (b)) and the vertical symmetry, which is defined in this work by

$$S = \frac{n_{\text{top}} - n_{\text{bot}}}{\min(n_{\text{top}}, n_{\text{bot}})}, \tag{4.1}$$

with the Cs density at the top LOS n_{top} and at the bottom LOS n_{bot}, respectively. By this definition, $S = 0$ reflects symmetric Cs distribution whereas $S = 1$ would refer to twice the density at the top LOS.

In the vacuum phase before the pulse, the Cs density at both LOS is constant in time, with doubled density at the top LOS. As discussed earlier, the equilibrium Cs density in vacuum phases is determined by the Cs evaporation rate, the sticking on the source walls and the position of the Cs oven as well as of the measurement lines of sight – thus the Cs density is larger at the top line of sight, being closer to the Cs oven. The Cs density during vacuum phases is typically in the order of 10^{14}–10^{15} m^{-3}.

The Cs density increases after deuterium gas is injected into the source. This so called 'H$_2$ effect', which can take place in hydrogen and deuterium gas, has been also observed in a lab experiment under similar vacuum and gas conditions [83], where an unknown chemical interaction of hydrogen gas with Cs compounds resulting in a release of pure Cs is suggested. In [83], an increase of the volume Cs density of up to two orders of magnitude has been observed with some pressure
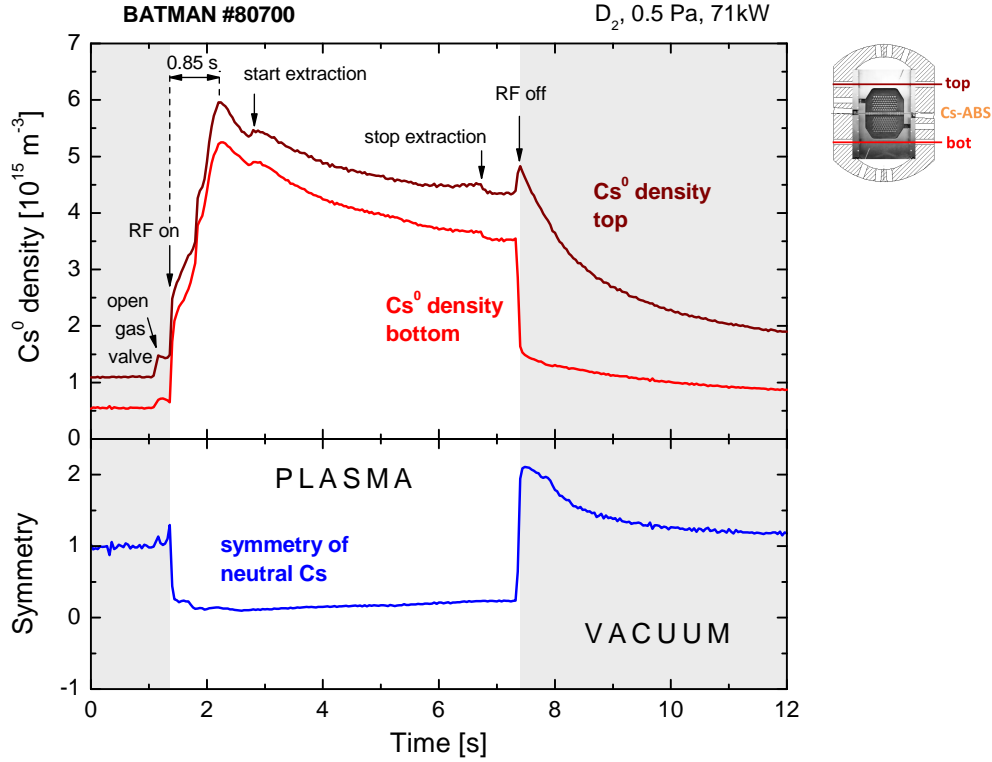
Figure 4.4: *Temporal dependence of the Cs^0 density at two LOS and its vertical symmetry for a typical pulse.*

dependence of the hydrogen gas – the maximum increase was observed at a pressure of ≈ 5 Pa. The effect is weaker pronounced at the prototype ion source, where usually a maximum increase of about 50% is observed. It should be mentioned, that – also not shown here – also the contrary effect is sometimes observed at BATMAN: a decrease of n_{Cs^0} takes place after opening the hydrogen gas valve – possible chemical reactions might cause a decrease. However, the process behind this effect is not yet identified.

During the plasma phase, a fast increase of the neutral Cs density within one measurement point (40 ms) occurs, followed by a slower, further increase of the neutral Cs density to a value of a couple of 10^{15} m^{-3} at both LOS – although a large fraction of Cs is ionized ($> 90\%$ estimated in [84]). This means that the total Cs density – consisting of neutrals and ions – is increased by more than one order of magnitude during the plasma phase to a value of a couple of 10^{16} m^{-3}, what is explained by a release of Cs out of Cs compounds from layers at the source wall by interacting with reactive plasma particles and plasma radiation. Due to these plasma-induced redistribution processes, the vertical asymmetry of the Cs distribution is lowered to a value of 0.1–0.2 during the plasma phase and

thus Cs is distributed in almost perfect symmetry. Hence, the effective sticking of Cs is lowered in plasma phases due to the release of Cs out of compounds. This result is in good agreement with the simulation of the Cs coverage of the PG by a transport code, showing a more homogeneous coverage during plasma phases [48].

The Cs^0 density is decreasing after the first second of the plasma phase at both lines of sight during the rest of the plasma phase. However, during the beam extraction phase, the Cs^0 density is slightly increased. A more pronounced increase of the Cs 852 nm emission during extraction phases has been observed at MANITU, depending on the applied extraction voltage [41]. The reason for this increase are back-streaming positive ions from the acceleration system: positive ions are created in the extraction system due to collision of extracted particles with background gas particles and subsequently are accelerated in counter direction towards the back plate of the source, resulting in a release of Cs from layers at the wall. This effect is only weakly pronounced at BATMAN, because back-streaming ions hit solely the back plate of the driver due to the small size of the extraction area (in contrary, at MANITU back-streaming ions also impinge the back plate of the expansion chamber). Due to the dense and hot driver plasma, no thick layers of Cs and Cs compounds can develop there.

To point up the importance of Cs redistribution during the plasma phase, the Cs^0 and Cs^+ density as well as the resulting Cs^0 and Cs^+ flux towards the plasma grid are listed in table 4.1 for the top LOS shown in figure 4.4. The previously mentioned estimation of $\gtrsim 90\%$ for the fraction of ionized Cs is used. The flux of neutral Cs is increased by one order of magnitude during the plasma phase. Depending on the sheath potential profile, also Cs ions can reach the PG during plasma phases – the total flux of Cs towards the plasma grid is then increased by two orders of magnitude compared to the previous vacuum phase. Neglecting chemical reactions as well as desorbing Cs fluxes, a Cs coverage of 2.4 monolayers is obtained during the 200 s vacuum phase, whereas the neutral Cs flux would result in a coverage of 0.72 monolayers during the 6 s plasma phase. Cs ions can increase the coverage to more than 7.2 monolayers during the plasma phase. Consequently, much higher Cs fluxes during the plasma phase compared to the vacuum phase are required in order to obtain a stable and low work function.

After the end of the plasma phase, the Cs dynamics often differs strongly between the two LOS: in the pulse shown in figure 4.4, an increase of neutral Cs is followed by a decrease to the initial equilibrium level within some seconds at the top LOS, whereas at the bottom LOS a much faster decrease to the initial

Table 4.1: *Cs^0 and Cs^+ density as well as Cs^0 and Cs^+ fluxes towards the PG during the vacuum and plasma phase at the top LOS of BATMAN #80700 (figure 4.4) using a gas temperature of 35 °C during vacuum phase and 0.1 eV during plasma phase.*

	n_{Cs^0}	n_{Cs^+}	Γ_{Cs^0}	Γ_{Cs^+}
Vacuum	1×10^{15} m^{-3}	0	5.6×10^{16} m^{-2}s^{-1} 0.012 ML/s	0
Plasma	5×10^{15} m^{-3}	$\gtrsim 5 \times 10^{16}$ m^{-3}	5.4×10^{17} m^{-2}s^{-1} 0.12 ML/s	$\gtrsim 5.4 \times 10^{18}$ m^{-2}s^{-1} $\gtrsim 1.2$ ML/s

level takes place. This dependence changes during one day of operation: plotted in figure 4.5 is the seventh and 130. pulse of one operational day. In the seventh pulse, a fast decrease of the neutral Cs density below the detection limit happens at both LOS after the end of the plasma phase, whereas after the 130. plasma pulse the neutral Cs density is strongly increased at both LOS. In contrary to the pulse shown in figure 4.4, the pulses in figure 4.5 have been operated in hydrogen instead of deuterium gas. However, the Cs dynamics shows no significant difference between both isotopes.

An increased Cs^0 density short time after the end of the pulse can be based on the following reasons:

- Recombination of Cs^+. Cs ions are recombining with electrons after the end of the plasma phase in the volume and at the source walls. However, with the thermal velocity of Cs atoms of more than 200 m/s at temperatures of at least 35 °C (minimum value of the wall temperature), a typical source dimension of 0.5 m and a sticking probability of 0.7–0.9, an increased Cs density would decay to the equilibrium within the time of some ms.

- Cs desorption from source walls. The surface temperature of the source wall is heated up during a plasma pulse by up to 10 K. This could lead to an additional desorption flux of Cs from the source wall. The time constant of the decay with some seconds fits to thermal effects.

- Lowered sticking coefficient at the walls. The sticking value is reduced in the plasma phase and might remain reduced after the end of the plasma pulse (in comparison to the vacuum phase before the plasma pulse) due to plasma cleaning effects for a certain time. The sensitivity of the volume density of Cs on the sticking value can be estimated rather simply:
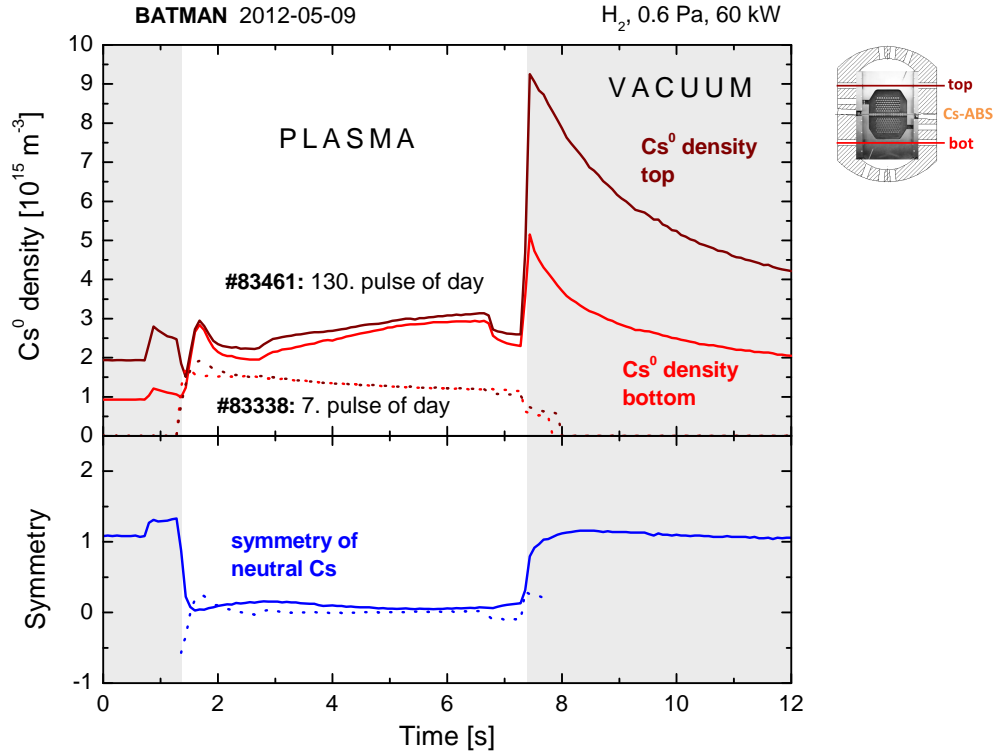
Figure 4.5: *Temporal dependence of the Cs^0 density at two LOS and its vertical symmetry for the seventh and 130. pulse of an operational day.*

The Cs density is determined by the evaporation of Cs out of the oven as a source term and sticking at the source wall as a sink term. If assuming a one-dimensional model without particle collisions (two walls with a distance of 0.5 m), this yields for the number of Cs atoms N between the two walls

$$\frac{\mathrm{d}N}{\mathrm{d}t} = X_{\mathrm{ev}} - \frac{NS}{\bar{t}}, \tag{4.2}$$

with the Cs evaporation rate X_{ev}, the sticking coefficient S and the time between two wall contacts $\bar{t}$. In equilibrium ($\mathrm{d}N/\mathrm{d}t = 0$) this yields a Cs particle number N of

$$N = X_{\mathrm{ev}}\bar{t}S^{-1}. \tag{4.3}$$

Thus, a five times increased neutral Cs density – as observed in figure 4.5 – would require a sticking factor which is temporary five times lower. Due to the lack of available data of the influence of plasma cleaning effects on the sticking at the source wall, no statement can be made whether this reduction is feasible or not.

To check the quality of this simple model, a typical Cs evaporation rate of

$X_{\mathrm{ev}} = 5$ mg/h $= 6 \times 10^{15} \; s^{-1}$ and a sticking factor of 0.8 in the vacuum case (no collisions, $\bar{t} = l/\bar{v}, l = 0.5$ m) is used. This yields $N = 1.8 \times 10^{13}$. If calculating a density out of this simple 1D model by dividing by the volume of the expansion chamber ($32 \times 59 \times 23$ cm^3), the Cs density becomes 4×10^{14} m^{-3}, which is in the order of magnitude of typically measured Cs densities at BATMAN during vacuum phases.

Most likely the dynamics in this phase is not solely determined by one of these reasons, but by a combination of them. These effects cannot be separated by the available diagnostics, which allow only the determination of the Cs volume density as a result of Cs fluxes. However, the often seen strong difference in the dynamics between the two lines of sight after the end of the plasma pulse clearly show that the effects listed above can differ locally inside the source, and that varying sticking plays an important role for the Cs dynamics.

Investigation of the sticking

A more detailed investigation of the sticking was possible by using the Cs dispenser oven, which has a SID mounted in front of its nozzle capable for determination of the relative evaporation rate (see section 2.6). The dependence of the Cs density in the vacuum phase measured by the absorption spectroscopy at the vertical line of sight on the evaporation rate is shown in figure 4.6. The data points refer to the first pulses of a day of operation; the vacuum Cs density as well as the SID current, which corresponds to the relative Cs evaporation rate, is measured at the beginning of the BATMAN pulse trigger in the vacuum phase before the plasma pulse – as shown in figures 4.4 and 4.5, a stable equilibrium is established at this time.

During the first five pulses shown, the evaporation rate of the oven is steadily increased, whereas the Cs density is below the measurement threshold. A further increase of the evaporation rate leads to an increase of the Cs density, which becomes detectable. The Cs evaporation rate has been kept constant from the eights pulse onwards at about 8 μA SID current for several pulses with constant operational parameters; however, the Cs density is steadily increasing from pulse to pulse. A decrease of the Cs evaporation rate after several pulses leads to a decrease in the Cs density, but the density is higher than during the increase phase of the Cs evaporation. Cs reservoirs at the source wall have been built up due to the continuous evaporation of Cs.
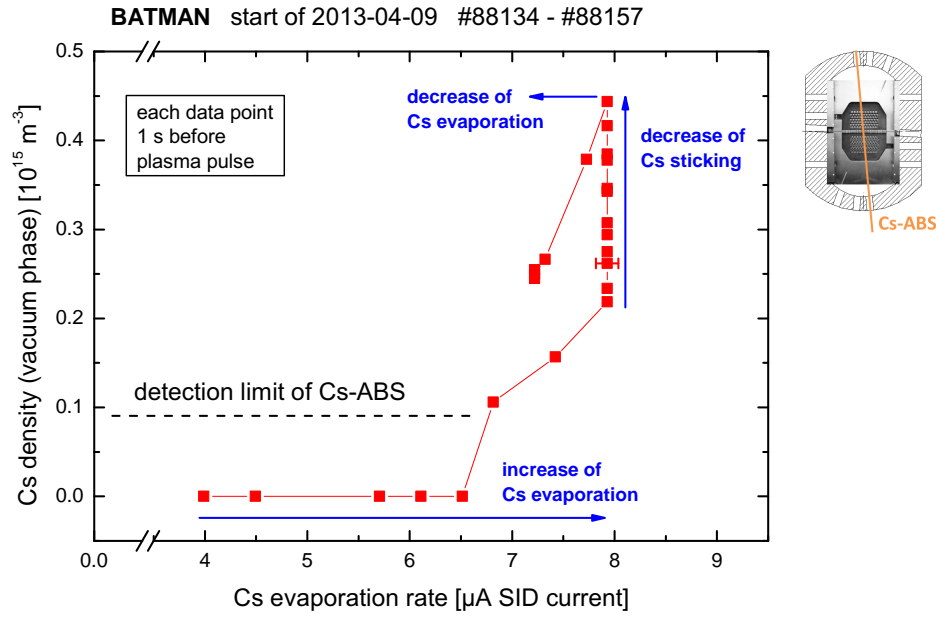
Figure 4.6: *Dependence of the Cs density in the vacuum phase on the Cs evaporation rate out of the oven.*

From the increasing vacuum Cs density at constant Cs evaporation rate follows that the sticking of Cs at the walls is reduced during constant Cs evaporation combined with pulsed plasma operation, which is attributed to the build up of Cs reservoirs as well as a cleaning effect of Cs layers at the source wall. Thus, the sticking value is not constant during one day of operation. In the simple model explained above, the measured increase of the vacuum Cs density from 0.22×10^{15} m^{-3} to 0.44×10^{15} m^{-3} refers to a reduction of the sticking by a factor of two (see equation (4.3)).

Concluding, continuous operation of the ion source with plasma pulses combined with continuous Cs evaporation reduces the sticking of Cs at the source wall. A lowered sticking is beneficial to achieve a homogeneous Cs distribution during vacuum phases. However, one should also keep in mind the symmetrizing effect of the plasma-induced redistribution of Cs during plasma phases.

Comparison of the Cs symmetry in vacuum and plasma phases

Whereas in the figures 4.4 and 4.5 the vertical symmetry of the Cs distribution measured by Cs-ABS has been compared for individual pulses during plasma and vacuum phases, a comparison is done in the following statistically for several months of BATMAN operation with hydrogen and deuterium as working gas. Figure 4.7 (a) shows the vertical symmetry during plasma and vacuum (1 s before
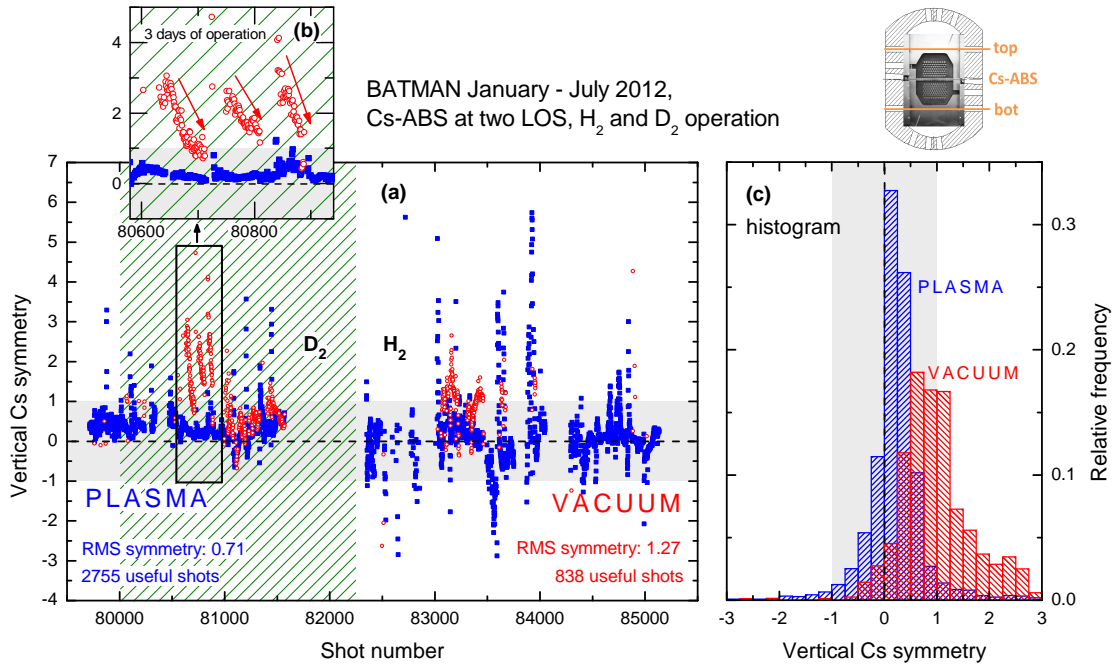
Figure 4.7: *Comparison of the vertical Cs symmetry during plasma and vacuum phases for several month of BATMAN operation in hydrogen and deuterium: (a) shown are all useful shots, (b) cut view for three consecutive days and (c) histogram of the data.*

plasma pulse) phases for the whole measurement campaign between January and July 2012, (b) is a cut view of (a) for three consecutive days of operation and a histogram in (c) shows the relative frequency of the vertical Cs symmetry in steps of 0.25 for plasma and vacuum phases. No data is available between the shots #81600–#82300, where the Cs-ABS has not been in operation due to defects of components in the setup.

The number of useful shots (with a density above the detection threshold at both LOS) is much higher for plasma phases (2755) compared to vacuum phases (838). The reason for this difference is that during low Cs evaporation rates the density is often below the detection threshold in vacuum phases, whereas Cs redistribution processes lead to a higher Cs density during plasma phases. Several observations can be made:

- The Cs symmetry in vacuum phases is often increased during one day of operation. This effect can be identified clearly e.g. for the pulses 80640–80880, where three days of operation can be separated, each starting at a higher Cs vacuum asymmetry, which is steadily decreased during one day of operation (see cut view in figure 4.7 (b)). The increase of the vacuum

symmetry is explained by a decrease of the sticking during one operational day, as was shown before.

- The Cs symmetry is not stable (neither in vacuum, nor in plasma phases) at long term. The homogeneity of neutral Cs is better during plasma phases (92% of the shots are in the symmetry range between -1 and $+1$, whereas only 56% of the vacuum pulses are in the same range). This is also indicated by the root mean square (RMS) value of the symmetry, whose value is 0.71 for all plasma pulses and 1.27 for all vacuum pulses – thus, Cs is distributed more symmetric in plasma phases.

- As can be identified in the histogram (figure 4.7 (c)), Cs is distributed vertically symmetric inside the source during most plasma pulses – the highest relative frequency is in the range of the vertical symmetry between 0 and $+0.25$. In contrary, the Cs symmetry during vacuum phases shows a clear trend to the top part of the source, where the Cs oven is mounted – the relative frequency shows a broader maximum in the range of $+0.5$ and $+1.25$.

In order to identify a possible isotope effect between hydrogen and deuterium operation on the vertical Cs symmetry, a histogram of the relative frequency of the vertical Cs symmetry – separated for the hydrogen and deuterium pulses plotted in figure 4.7 – is shown in figure 4.8 (a) in the vacuum phase and (b) during plasma operation. The general statements from above – more asymmetric distribution in vacuum phases and almost symmetric distribution during plasma phases – are valid for both isotopes. During vacuum phases, the distribution shows a narrower profile in hydrogen, whereas in plasma phases the profile is broader and slightly more symmetric in hydrogen compared to deuterium.

The deviation between the isotopes in the vacuum phase can be simply caused by the limited and differing number of counts for the statistical comparison, which is 540 for deuterium and 288 for hydrogen operation. As mentioned above, the number of counts is much higher for plasma operation: 1122 for deuterium and 1633 for hydrogen operation; for this reason, more precise statistical statements can be made. The slightly shifted vertical Cs symmetry to the top part in deuterium can be caused by a higher evaporation rate out of the oven in the top part, which is required for achieving optimum source performance in deuterium. The reason for the slightly broader distribution during plasma phases in hydrogen compared to deuterium might be caused by differences in the plasma homogeneity: the vertical
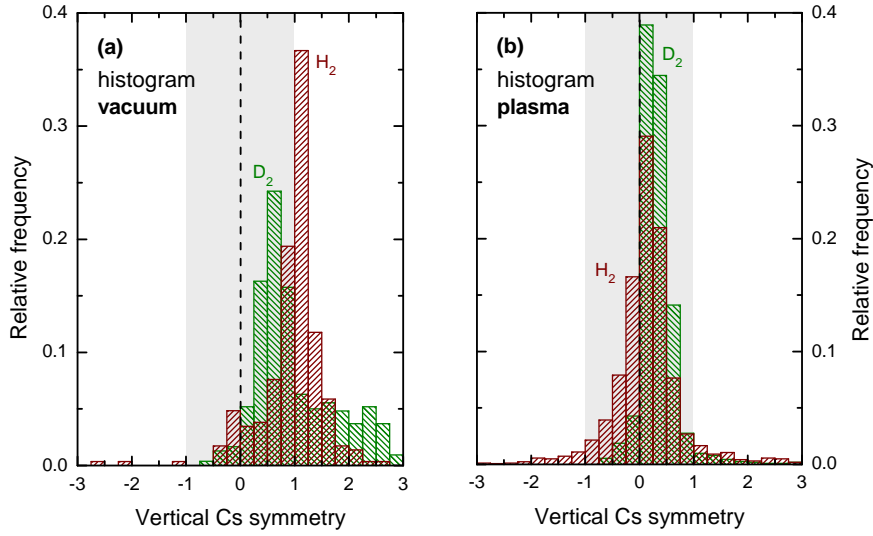
Figure 4.8: *Histograms showing the relative frequency of the vertical Cs symmetry, compared for hydrogen and deuterium operation in vacuum (a) and plasma (b) phases.*

plasma drift inside the source has an influence on the vertical Cs distribution, which will be shown later in figure 5.12. Differences in the plasma symmetry between hydrogen and deuterium operation will be discussed in section 5.4. Concluding, there is no significant isotope effect on the vertical Cs distribution in the source.

4.1.4 Conclusion

The results show that a strong de-coupling of the Cs dynamics regarding the amount of Cs as well as the vertical distribution takes place between plasma and vacuum phases at BATMAN: the density in vacuum phases is determined by the Cs evaporation rate, the sticking of Cs at the source wall and the position of the Cs oven as well as of the measurement LOS. The sticking factor of Cs during vacuum phases is usually reduced during one day of operation, resulting in a more symmetric distribution of Cs inside the source. In plasma phases, a large amount of Cs is released from the source wall leading to a fast and large increase of the total amount of Cs in the volume. Due to these redistribution processes, Cs is distributed more homogeneously inside the source. The inhomogeneity of Cs evaporation shows no drawback in order to achieve a stable coverage of Cs at the plasma grid. This gives also a hint for the design of the upcoming, larger H^- ion sources that homogeneous evaporation of Cs is not mandatory, since the Cs dynamics is mainly determined by plasma-induced redistribution processes.

A correlation between the Cs density during the plasma phase with the source performance is usually seen at short term (during one day of operation) in the Cs conditioning phase; however, not at long term in different campaigns. Possible reasons for this behavior can be a varying required flux of Cs onto the plasma grid due to a slightly changing amount of impurities or the importance of the Cs^+ flux towards the PG, which is not accessible for diagnostics at the moment. However, the flux of Cs^+ to the PG is very sensitive on the sheath potential profile and thus the plasma potential in front of the plasma grid – the varying sheath potential profile will be discussed in section 5.2. Thus, there is unfortunately no long-term control of the Cs evaporation rate possible by simply adjusting to a certain neutral Cs density – the hope of a possible feedback loop for the control of the Cs evaporation rate has been one aim for the usage of dedicated Cs diagnostic tools. Nevertheless, the neutral Cs density during plasma phases needs to be in the order of 10^{15} m^{-3} for achieving high source performance

4.2 MANITU: Cs dynamics in long pulse operation

As seen at BATMAN, plasma phases cause a strong redistribution of Cs inside the IPP prototype ion source. The investigation of the Cs dynamics in longer plasma pulses is thus desirable.

4.2.1 Redistribution of Cs in longer pulses

Time traces of the neutral Cs density as well as of the Cs 852 nm emission for a series of consecutive pulses with a plasma-on time between 25 and 35 seconds are shown in figure 4.9, during which the evaporation rate of the Cs oven has been increased from shot to shot by a temperature increase of the standard IPP Cs oven. The increase of the Cs evaporation rate results in an increase of the Cs density in the vacuum phase before the plasma pulse (rising from 2.8×10^{14} m^{-3} to 2.2×10^{15} m^{-3}). Although the evaporation rate is not measured at the standard oven, the magnitude of the increase can be estimated: in the simple model discussed before, the increase of the neutral Cs density during vacuum phase of a factor of 7.9 would be based on the same increase of the Cs evaporation rate, if constant sticking is assumed (equations (4.2) and (4.3)). However, because the
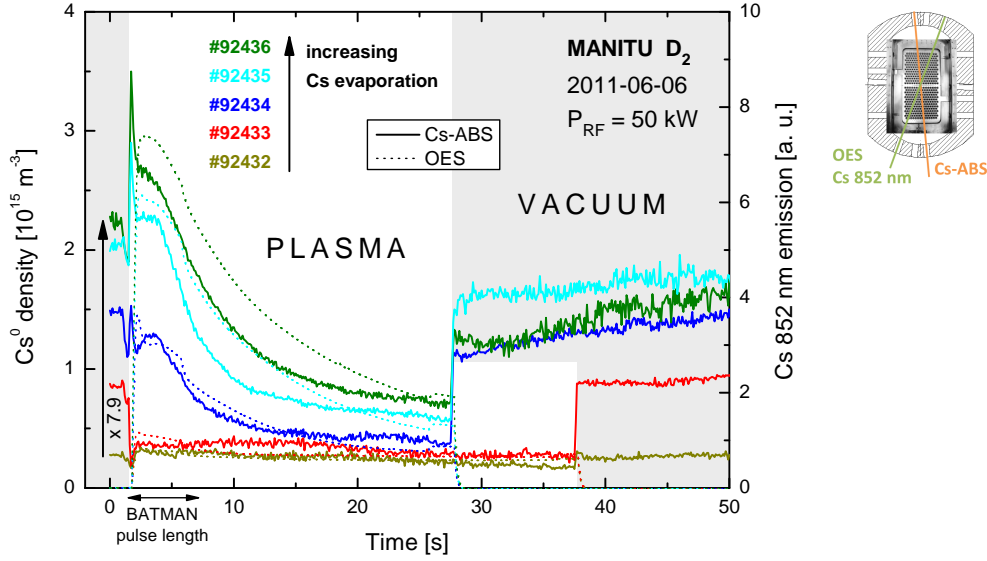
Figure 4.9: *Neutral Cs density (solid line) and Cs 852 nm emission (dots) for five consecutive MANITU pulses with increasing Cs evaporation rate.*

sticking is decreased during an operational day as was shown in figure 4.6, the actual increase of the Cs evaporation rate is somewhat lower.

Before the plasma pulse, the neutral Cs density is decreased during the deuterium gas puff – the effect of the gas puff on the Cs density has been already discussed before. The dynamics during the plasma phase differs for the shown pulses: whereas for the first two pulses the neutral Cs density is stable at a low amount, the following pulses show a peak of the Cs^0 density at the beginning of the plasma phase followed by a slow decrease – resulting in a neutral Cs density, which is up to a factor of four lower compared to the vacuum phase. The Cs 852 nm emission shows the same trend as the Cs-ABS during all plasma pulses. Possible reasons for the slightly differing behavior have been already discussed in section 4.1.1.

The dynamics during the longer plasma phase is explained as follows: as in short pulses at BATMAN, the Cs density during plasma phases is determined by plasma-induced redistribution processes. Due to the expanding plasma inside the expansion chamber, the plasma-wall interaction differs locally. In longer pulses, Cs is redistributed in large amount towards surfaces with less plasma interaction, i.e. positions with a high sticking – the Cs density is then not stable during the longer pulses. The loss of Cs through the extraction apertures is not significant, because the large fraction of ionized Cs is reflected by the extraction potential during the beam extraction phase. In addition, no significant amount of Cs is found behind the plasma grid after venting the test facility – in contrary, thick

layers of Cs compounds are formed in the source.

The redistribution towards surfaces with less plasma interaction is of particular importance, if only small Cs reservoirs have been built up in the source: the dynamics during the pulse is then very sensitive on the amount of evaporated Cs in the vacuum phase before the pulse. The de-coupling between the Cs^0 density during vacuum and plasma phases is much less pronounced for an increasing plasma/vacuum duty cycle.

After the end of the plasma phase, no peak in the Cs^0 density appears. As discussed earlier, this behavior is attributed to a high sticking of Cs and is seen also regularly at BATMAN at the start of an experimental day during the re-conditioning phase (compare to figure 4.5).

4.2.2 Indication of Cs depletion during long pulses

It is known that especially the heat-up of the not actively cooled bias plate, where Cs is accumulated during vacuum phases, results in a release of Cs during long pulses ($t \geq 100$ s) and thus plays an important role for the Cs dynamics at MANITU [48]. The subsequent redistribution of Cs can lead to a strong reduction of the Cs^0 density in the volume during long pulses and thus to a reduction of the Cs flux towards the plasma grid, if not sufficient Cs reservoirs at the source walls are available; i.e. if not a sufficient amount of Cs has been evaporated in the past. This effect is shown in figure 4.10, where the neutral Cs density during three consecutive pulses with a pulse length of 72, 198 and 99 seconds are shown in combination with the extracted H^- and co-extracted electron current density. These pulses were done at the second day of an experimental campaign; this means that not a large amount of Cs has been yet evaporated into the source. The operational parameters were kept constant.

In the plasma phase of the first shown pulse (#91772), the neutral Cs density is strongly decreasing during the first 10 s from 2×10^{15} m^{-3} to 0.8×10^{15} m^{-3} – the same trend as observed in the shorter pulses shown in figure 4.9. During the rest of the plasma pulse, the Cs density is slightly increasing, which is caused by the heat-up of the bias plate. Obviously, the heat-up results in a release of Cs.

In the following plasma pulse (#91773), the neutral Cs density decays within the first 10 s to an elevated Cs density of 1.1×10^{15} m^{-3}. The reason for the higher level at the beginning of the pulse is that the vacuum phase before the pulse has been longer than usual (400 s instead of 200 s), so a larger amount of Cs has been evaporated into the source in the vacuum phase before. An increase of
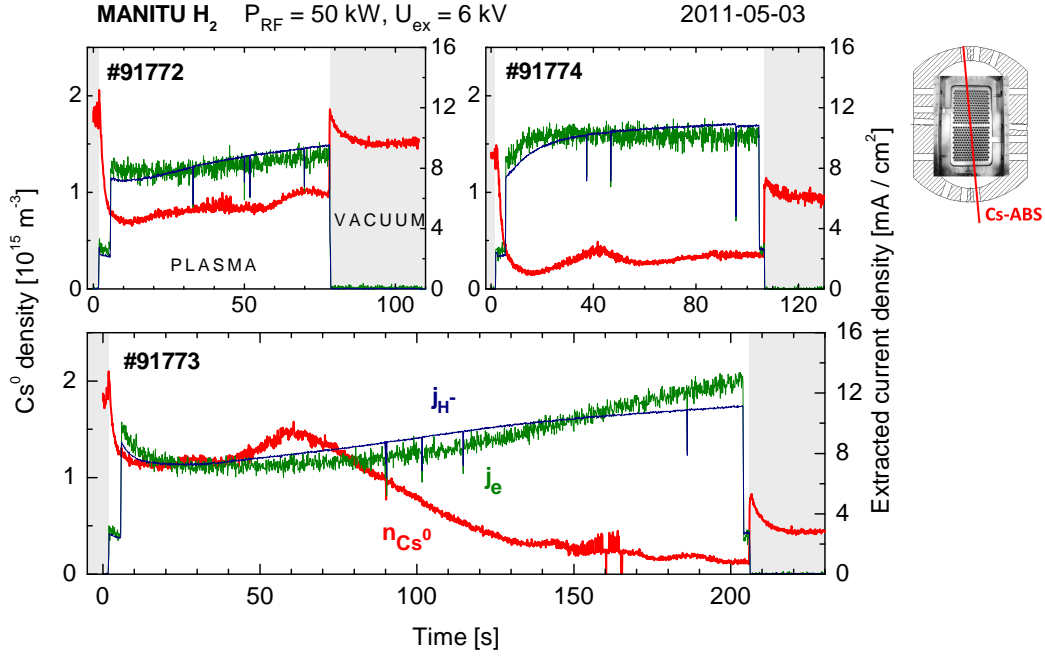
Figure 4.10: *Neutral Cs density and extracted current densities for three consecutive pulses at MANITU. The vacuum phase between #91772 and #91773 lasted 400 s in contrary to 200 s before #91772 and #91774.*

the Cs density between $t = 10$ s and $t = 60$ s is followed by a decrease of Cs. The increase is attributed again to a heat-up of the bias plate. The neutral Cs density is afterward decreased within one minute to a value of 0.2×10^{15} m^{-3} – the Cs reservoirs at the source wall in contact with the plasma as well as on the bias plate have been almost depleted. In addition, the vacuum Cs density a couple of seconds after the plasma pulse (0.5×10^{15} m^{-3}) is lowered compared to the level before the plasma pulse (1.8×10^{15} m^{-3}): the depletion of the Cs reservoirs at the source walls and bias plate during the plasma pulse results in an increased sticking of Cs.

Within the vacuum phase between the pulses #91773 and #91774, the Cs density almost recovers to a value of 1.4×10^{15} m^{-3} – however, during the plasma pulse, the amount of Cs is lowered (0.3×10^{15} m^{-3}) compared to the first shown pulse: the Cs reservoirs that have been depleted during the pulse #91773 are not yet recovered.

The influence of the Cs dynamics on the source performance is seen from the plotted time traces of the extracted H$^-$ and co-extracted electron current density: during the depletion of Cs in #91773, the co-extracted electron current density starts rising – however, also the extracted H$^-$ current density is increasing during

the plasma pulse. Both extracted current densities keep also increased in #91774 compared to #91772. Thus, the correlation of the Cs volume density on the source performance is less pronounced. However, the dynamics of the co-extracted electron current density is slightly stronger pronounced compared to the extracted H^- current density during the depletion of Cs in pulse #91773, this might cause problems for long-term source operation. Hence, it can be stated that in order to reach a stable source performance, the Cs density should be kept stable during the pulses leading to stable fluxes of Cs towards the plasma grid. Obviously, sufficient Cs reservoirs at the source walls are required for this aim – the amount of Cs evaporation during vacuum phases and the total amount of evaporated Cs during the experimental campaign is of much higher importance compared to short pulse operation. Achieving stable Cs conditions during a one hour plasma pulse is one of the most demanding challenges for the large scale ITER source.

4.2.3 Conclusion

The Cs dynamics differs at the small-scale prototype source in longer plasma pulses in comparison to short pulses: the vacuum phase before the pulse as well as the total amount of evaporated Cs during a campaign and thus the Cs reservoirs at the source wall play a much more important role in order to avoid a depletion of caesium. A comparison of the neutral Cs density during plasma and vacuum phases has been possible using the Cs-ABS: due to the depletion of Cs reservoirs, the neutral Cs density during the plasma phase can be decreased to a value of almost one order of magnitude lower compared to the vacuum phases. Even when taking the large fraction of ionized Cs into account, total Cs fluxes in the plasma phase can then decrease to a similar amount compared to vacuum phases. However, at MANITU, the Cs dynamics is not only controlled by the interplay of plasma with Cs reservoirs at the temperature-controlled source walls, but also by the heat-up of the bias plate. Thus, ELISE will be the first test facility in which the long pulse Cs dynamics can be investigated at ITER relevant conditions with a temperature-controlled bias plate, what is a desirable task for the future. Nevertheless, it has been clearly seen that achieving optimum Cs conditions for long plasma pulses is much more challenging compared to short pulses.

5 Plasma characteristics and dynamics in the boundary layer

For the characterization of the plasma in the extended boundary layer, the setup shown in figure 3.15 (a) has been used. A comprehensive comparison between the correlation of the extracted H$^-$ current density on the density of H$^-$ in the volume in hydrogen and deuterium operation will be shown, which has been possible with the CRDS being installed as a routine diagnostic. A qualitative comparison of the plasma and H$^-$ homogeneity is followed.

A detailed characterization of the plasma dynamics is presented for varying source pressure in both, deuterium and hydrogen gas, in particular to find correlations of the plasma parameters with the co-extracted electron density. Since the amount of co-extracted electrons reacts very sensitive on the potential profile in the sheath close to the plasma grid and thus on the bias current (see section 2.5), the comparison is carried out for varying bias voltage. However, variation of the bias voltage does not only influence the potential profile in the sheath, but also the vertical homogeneity of the plasma distribution in the expansion chamber – hence, the effect of the bias on the plasma parameters and source performance is shown before.

5.1 Dependence of the extracted H$^-$ current density on the H$^-$ density

The dependence of the source performance on n_{H^-} is plotted in figure 5.1 for one day of operation during the Cs conditioning phase at constant operational parameters. Both the extracted electron and ion current density correlate rather well with the H$^-$ density in an axial distance of 2.2 cm to the PG: the extracted H$^-$ current density depends almost linearly on the H$^-$ density; the influence on
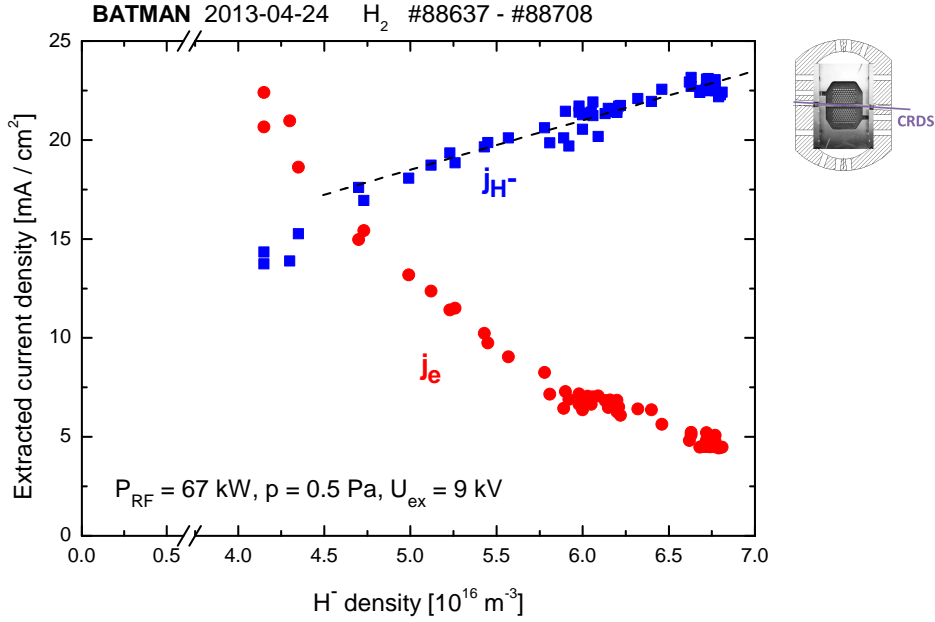
Figure 5.1: *Dependence of the source performance on the negative hydrogen ion density during one day of operation with constant operational parameters.*

the amount of co-extracted electron current density is stronger pronounced with a steep decrease for increasing H^- densities. This clear correlation experimentally proves that a link of plasma parameters in an axial distance of several cm in front of the PG inside the extended boundary layer to the source performance exists.

The correlation of the source performance with the H^- density is also valid at long term, if shots with the same operational parameters (in particular extraction voltage and source pressure) are compared – in contrary to the correlation of the source performance with the neutral Cs density that does not hold at long term (see chapter 4.1). This long-term dependency is shown in figure 5.2 (a): the extracted H^- current density correlates almost linearly on the H^- density even when comparing different days in different experimental campaigns; however, the slightly varying source pressure strongly influences this dependence.

The dependence of the extracted H^- current density and of the H^- density in the volume on the source pressure is shown in figure 5.2 (b). A clear increase of n_{H-} by a factor of 1.5 happens in the pressure range of 0.44–0.74 Pa, whereas j_{H-} is almost constant or rather slightly decreasing at higher source pressure. The small reduction of j_{H-} can be a consequence of stripping losses of H^- particles in the extraction system. Stripping losses depend linearly on the gas density in the extraction system, in which an increase of the fraction of stripped particles from 3% at 0.4 Pa to 7% at 0.8 Pa has been experimentally determined at BATMAN
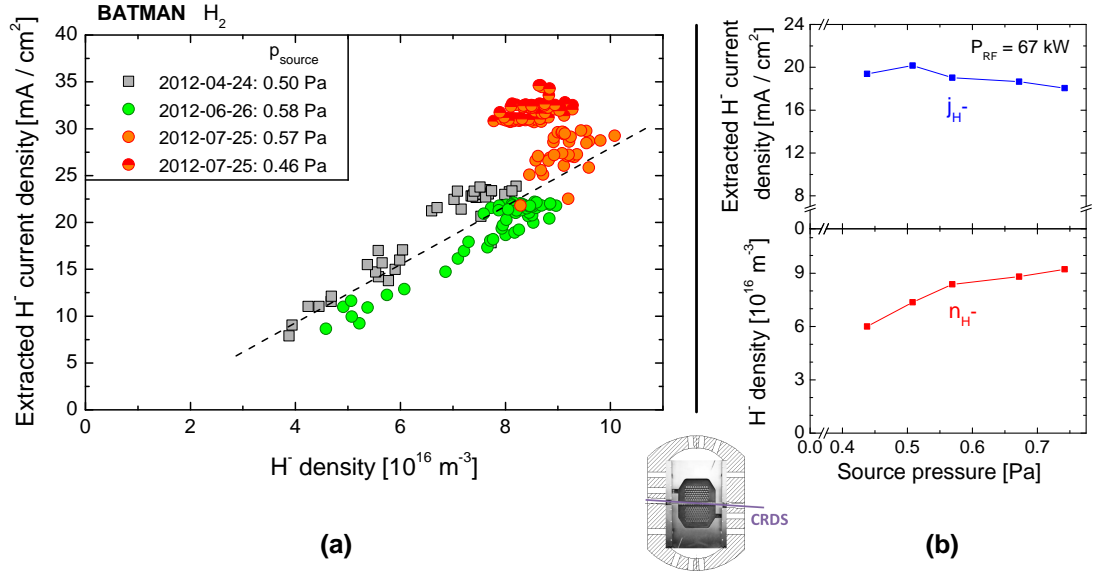
Figure 5.2: *(a): long-term dependence of j_{H^-} on n_{H^-}. (b): dependence of j_{H^-} and n_{H^-} on the source pressure.*

[85]. Recent investigations showed that the total fraction of stripped particles might be higher by a factor of up to two [86], which is in good agreement with the measured reduction of j_{H^-} for increasing source pressure by 10%.

At first glance, the increase of n_{H^-} at higher source pressure can be attributed to a hindered diffusion of surface produced H^-: an increased number of non-destructive particle collisions hinders the diffusion of locally produced H^- particles and thus changes the axial profile of n_{H^-}. According to Fick's first law of diffusion, the density gradient in axial direction is

$$\frac{\mathrm{d}n_{H^-}}{\mathrm{d}z} = -\frac{\Gamma_{H^-,z}}{D},\tag{5.1}$$

with the diffusion constant D. The assumption of a free diffusion is taken, because the diffusion of H^- from the plasma grid into the plasma volume takes place in counter direction compared to the expanding plasma out of the driver. For the diffusion constant D, in addition to Coulomb and elastic collisions also the bending of H^- in the magnetic field and destructive inelastic collisions must be taken into account. If the variation of n_{H^-} with varying source pressure is dedicated to changes of the diffusion, an adequate small value of D would be expected in order to yield a significant axial gradient of the H^- density. However, an axially resolved measurement of the H^- density in a similar surface-production H^- source revealed no significant difference of the H^- density in 2 mm and 24 mm distance to the
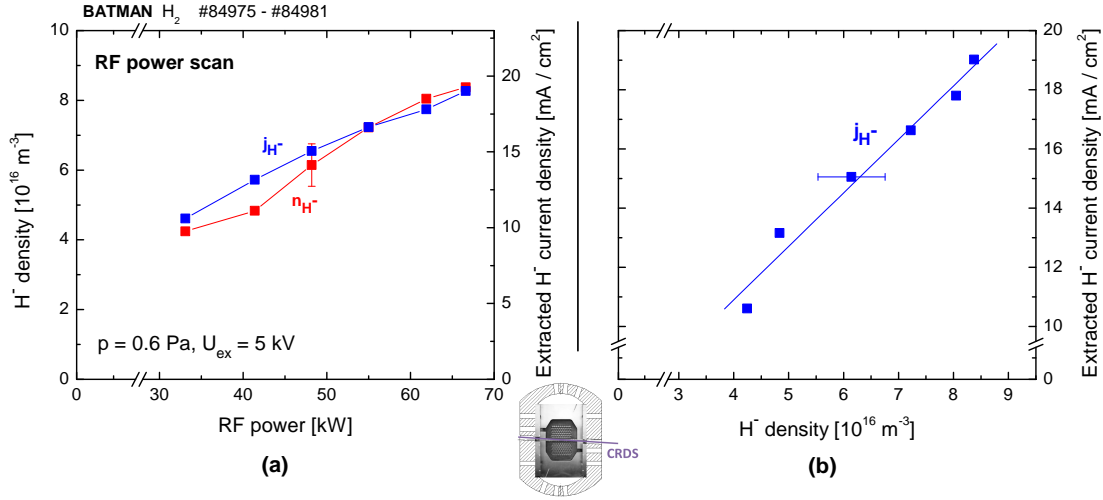
Figure 5.3: *(a): j_{H^-} and n_{H^-} as a function of the RF power, (b) dependence of j_{H^-} on n_{H^-} for the same pulses.*

PG [87] – thus, the axial density gradient is determined to be small and for this reason the diffusion constant D much larger compared to the discussion above. Hence, the density gradient and thus n_{H^-} is not very sensitive on variations of D and consequently not sensitive on the source pressure in this regime.

Thus, the process behind the pressure dependence of n_{H^-} is not yet identified. Indications can only be gained by modeling, in which the relevant physics must be implemented, what is a task of present and future work.

The dependence of the extracted H^- current density and H^- density on the applied RF power is plotted in figure 5.3 (a) in the range of $P_{RF} = 33$–67 kW at constant source pressure of 0.6 Pa and constant extraction voltage of 5 kV. Both quantities increase for higher RF power and show an almost linear dependence on each other, as shown in figure 5.3 (b). The increase of n_{H^-} and j_{H^-} for higher RF powers is attributed to an increased dissociation degree of hydrogen molecules [35], leading to an increased flux of conversion particles towards the PG and thus to an increased production rate of H^-.

Dependence on the ion mass

The comparison between hydrogen and deuterium operation regarding the negative ion density and the extracted negative ion current density is first done statistically by averaging over a couple of operational days. The reason for this approach is that although constant operational parameters of the source can be chosen, the conditioning of the source must not necessarily constant based on the Cs
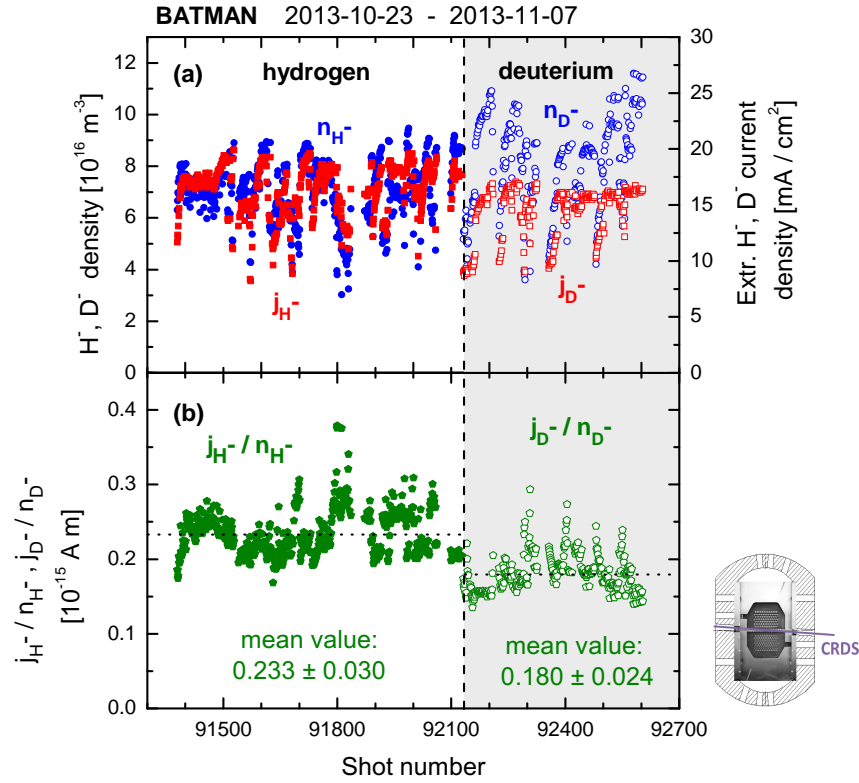
Figure 5.4: *Comparison of (a) n_{H^-}, n_{D^-} with j_{H^-}, j_{D^-}, and (b) the ratio j_{H^-}/n_{H^-} with j_{D^-}/n_{D^-} for pulses in hydrogen and deuterium operation with a similar experimental program.*

conditioning at long term. A direct comparison of individual pulses with the same parameters will be shown later in section 5.4.

Plotted in figure 5.4 (a) is the negative hydrogen and deuterium ion density as well as the corresponding extracted negative ion current density for 898 pulses in hydrogen and deuterium operation. The experimental program contained in addition to Cs conditioning and reconditioning phases several parameter scans (variation of the source pressure, RF power and bias voltage), influencing both quantities. The dependencies of n_{H^-} and j_{H^-} on the source pressure and RF power have been already discussed in the figures 5.2 (b) and 5.3; the influence of the bias will be shown in section 5.2. However, the experimental program has been similar in hydrogen and deuterium operation, so certain statistic statements can be made. A separation of the data points appears in figure 5.4 (a): in deuterium operation n_{D^-} is increased whereas j_{D^-} is slightly decreased compared to hydrogen operation.

To be less dependent on the particular Cs conditioning status and varying RF power, figure 5.4 (b) shows the ratio j_{H^-}/n_{H^-} and j_{D^-}/n_{D^-}, respectively for the

same pulses. Because $j = nev \propto \sqrt{m^{-1}}$, a constant value is expected for each isotope, with a difference of $\sqrt{2} = 1.41$ between hydrogen and deuterium. The ratio between the mean value of both isotopes is 1.29 ± 0.20 and thus agrees within its error bar to the expected value. This proves experimentally that the physics of ion production and extraction is basically the same for both isotopes.

5.2 Influence of biasing the plasma grid

The dependencies of the source performance, the plasma sheath potential profile, the bias current and of the vertical plasma symmetry on the applied bias voltage are shown within this section for the present magnetic filter field setup. For the different standard magnetic filter field setup at BATMAN, the basic dependencies have been investigated earlier [37].

Bias current–voltage characteristic

A typical bias current–voltage characteristic is shown in figure 5.5. The bias power supply only allows current flowing in the positive direction, what means that the lowest possible potential at which the plasma grid can be biased in respect to the source body is its floating potential, where no net current is flowing. As discussed in section 2.4, the electrically conductive source wall in combination with the strong gradients of the plasma parameters due to the magnetic filter lead to locally non-ambipolar particle fluxes. For this reason, the floating potential of the plasma grid differs to the ground potential of the source wall by almost 15 V. For larger applied bias voltages the bias current increases. The typical bias current is in the order of 10 A and thus one order of magnitude larger than the extracted electron current for the present magnetic filter field setup. Taking into account the increased area of the PG without the extraction apertures (426 cm^2) compared to the extraction area (63 cm^2), the electron flux is similar in both cases. However, as will be discussed later in detail, the contribution of positive ions impinging the PG and thus counting to the bias current must not be neglected due to the hindered transport of the magnetized electrons in axial direction.

The large bias current significantly influences the particle fluxes towards the wall and thus the local plasma potential distribution. The resulting electrical field in the plasma is large: since the distance between the bias plate and the PG is 1 cm, an applied bias voltage of 25 V results in a mean electrical field strength of 2.5 kV/m at the edge of the bias plate.
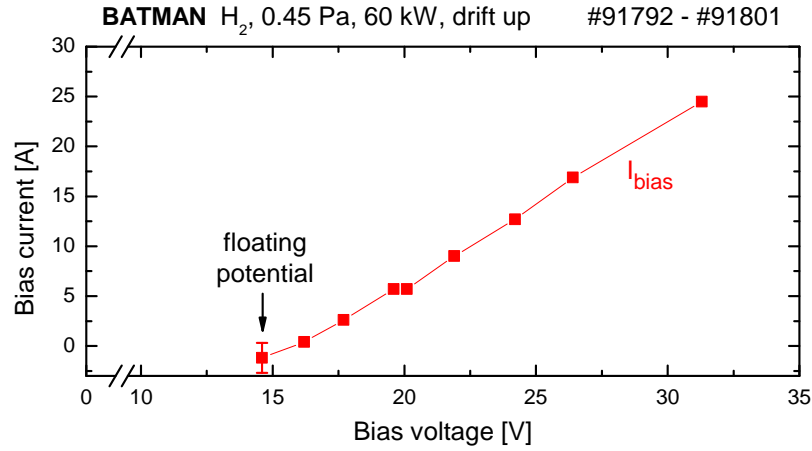
Figure 5.5: *Bias current–voltage characteristic.*

In standard operation, the drawn bias current is kept constant during a pulse at a fixed value which is between 10–20 A. However, for the physical analysis, the value of the bias voltage is of higher importance, since it is necessary to determine the potential profile $U_{\text{bias}} - \Phi_{\text{pl}}$, and thus the influence on the particle fluxes in the sheath close to the PG.

Influence on the plasma potential

The influence of the applied bias voltage on the plasma potential measured by the Langmuir probes is shown in figure 5.6. The plasma potential is measured at three positions: the top probe at the centered position in front of the extraction apertures, the top probe at the edge position close to the sidewall as well as at the vertical symmetric edge position of the bottom probe.

At all positions, the plasma potential is increased for larger applied bias voltages. The plasma potential is higher at the centered position of the probe, which is the relevant position in front of the extraction apertures for the physics linked to the source performance. At this position, a distinct transition takes place in the applied bias voltage range: at low bias voltages ($\lesssim$ 24 V), the plasma potential is larger in respect to the PG potential (= bias voltage). A classical plasma sheath is established: positive ions are accelerated onto the plasma grid, whereas negatively charged particles from the volume are repelled from reaching the grid. For increasing bias voltages, less electrons are repelled in the sheath and thus more electrons impinge the PG. At high bias voltages ($\gtrsim$ 24 V), the sheath is inverted: since the plasma potential is lower than the plasma grid potential, negatively charged particles are attracted onto the plasma grid.
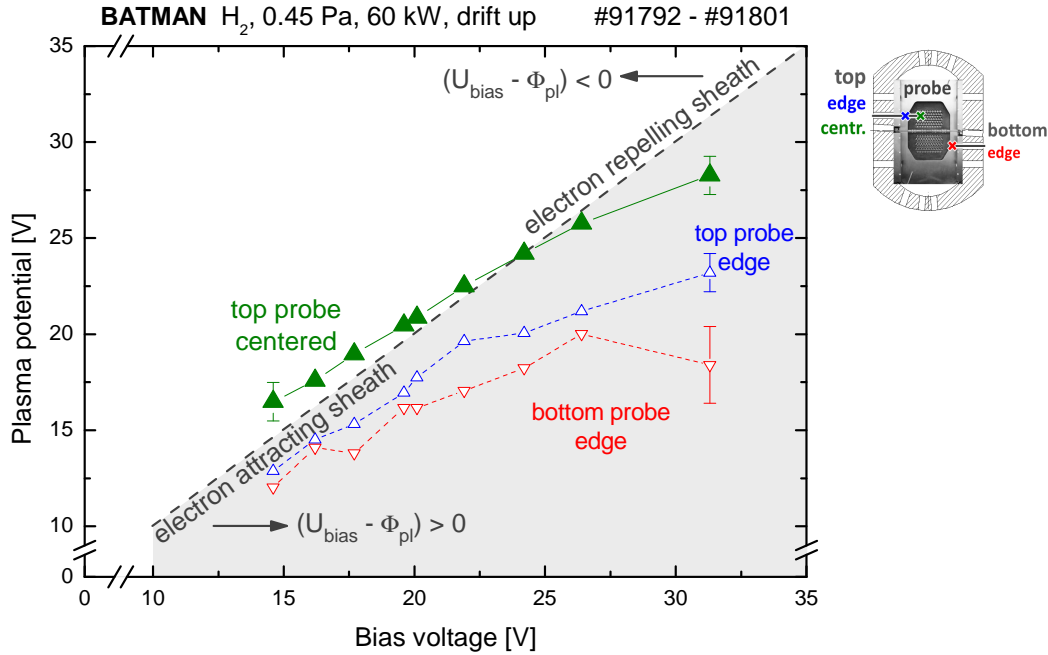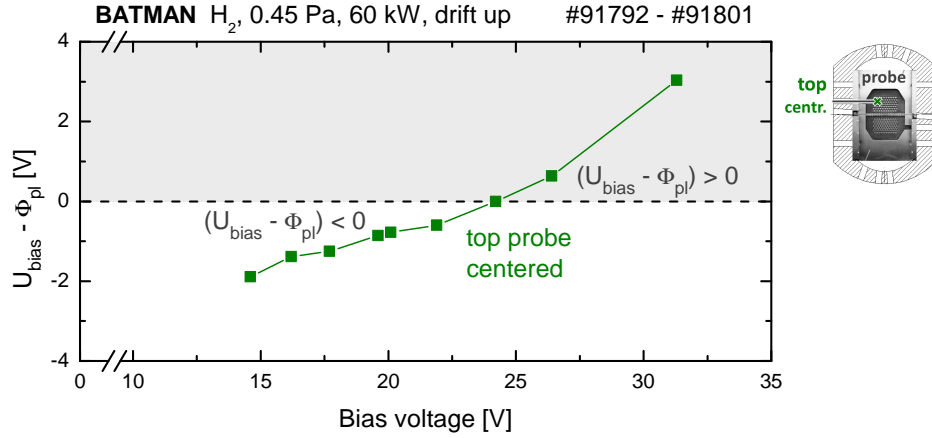
Figure 5.6: *Influence of the applied bias voltage on the plasma potential at three positions.*

The plasma potential is not only influenced by the bias voltage, but also by the plasma parameters – in particular by the amount of H^- as well as by the electron density and temperature. These quantities are influenced by the operational parameters as the source pressure, the RF power and the working gas. Hence, for comparison of the bias dependence for different source parameters neither the plasma potential nor the bias voltage is an advantageous quantity for usage as the controlling parameter. However, the difference between these two quantities $U_{bias} - \Phi_{pl}$ describes the character of the sheath independent on the plasma parameters and is thus the preferable parameter for comparing bias dependencies. The value of $U_{bias} - \Phi_{pl}$ is naturally controlled by the bias voltage as set parameter – this dependence is shown in figure 5.7: by variation of the bias voltage in a range between 15–31 V, $U_{bias} - \Phi_{pl}$ is only slightly changed from -2 V to $+3$ V at the top centered position – thus, determination of the plasma potential in good precision is needed, requiring the RF compensated Langmuir probe.

Influence on the source performance

The influence of the sheath potential profile on the source performance and on the H^- density is shown in figure 5.8 (a); the corresponding bias current density

Figure 5.7: *Influence of the bias voltage on the the sheath potential profile at the top centered probe position.*

is plotted in (b), where the area of the PG without the extraction apertures (426 cm^2) is taken into account. A strong variation takes place for the co-extracted electron current density: as long as the sheath is electron repelling, increasing the sheath potential profile (by increasing the bias voltage) leads to an increased bias current density, what results in a large reduction of the co-extracted electron current density of more than a factor of 3 in total. A further increase of the sheath potential profile in case of an electron attracting sheath shows no significant effect on the amount of co-extracted electrons; in contrary, the bias current density is not yet in saturation.

The influence on the extracted H$^-$ current density is much less pronounced: there is almost no change in the electron repelling case, whereas a slight decrease happens in the electron attracting case. The H$^-$ density shows a similar dependence as j_{H^-}; however, the influence of the sheath potential profile is stronger pronounced, particularly a stronger decrease of n_{H^-} at high values of the sheath potential profile compared to j_{H^-}.

The dependence of the co-extracted electrons shows the behavior which is expected by the sheath physics: starting at negative values of the sheath potential profile $U_{bias} - \Phi_{pl} < 0$ V, more electrons can be removed through the sheath for increasing values. Saturation takes place at $U_{bias} - \Phi_{pl} \geq 0$ V; however, electrons out of the volume penetrating directly through the plasma meniscus before reaching the plasma sheath of the PG are still extracted – for this reason, the co-extracted electron density saturates at a certain amount.

With the planar PG geometry also a strong saturation of the bias current would be expected for a bias voltage higher than the plasma potential, since the sheath
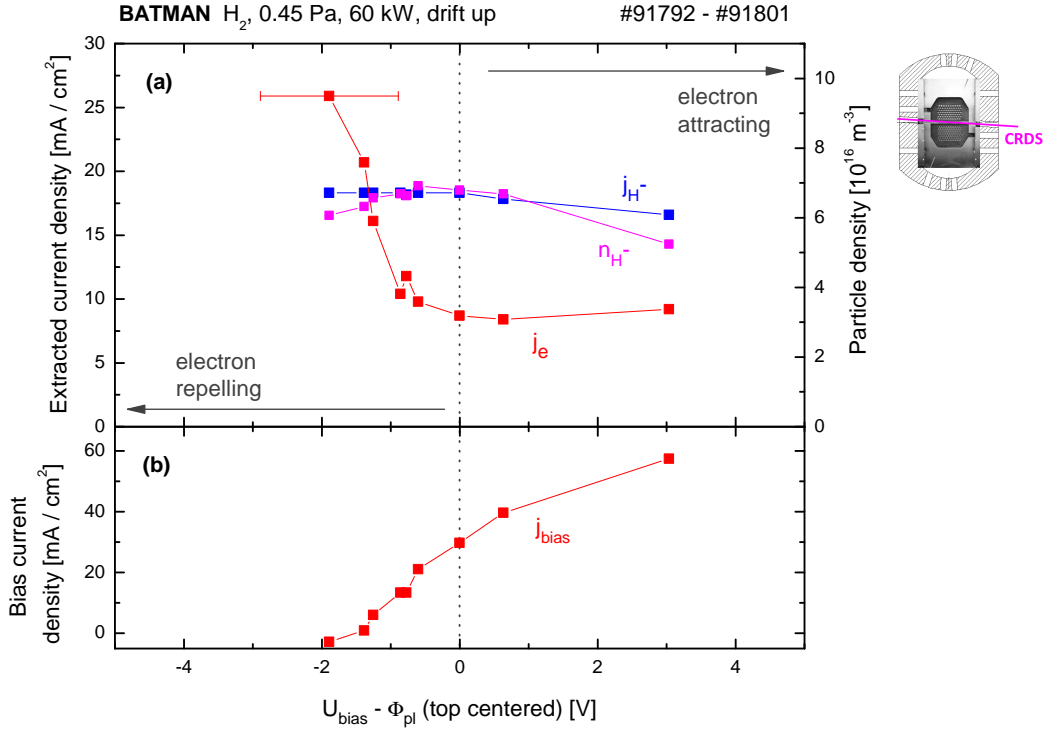
Figure 5.8: *Influence of the sheath potential profile on (a) the source performance and H⁻ density as well as (b) on the bias current density.*

area is not significantly enlarged at planar geometry in contrary to cylindrical Langmuir probes. However, this expected behavior is only valid in a classical electron–positive ion plasma, in which the flux of positive ions is much lower compared to electrons. Since the flux of negatively charged particles is reduced due to a hindered transport of electrons in the magnetic field and the presence of negative ions, the flux of positive ions to the PG is not negligible. However, positive ions are repelled for large positive values of $U_{bias} - \Phi_{pl}$, leading to a saturation of the bias current density.

Thus, the electron density at the sheath edge can be estimated by equation 2.12 for the maximum drawn bias current density ($j_{bias} = 60$ mA/cm^2), where the flux of positive ions becomes small and the bias current is subsequently dominated by electrons. This results in $n_e = 2.2 \times 10^{16}$ m^{-3}. Comparison with the experimentally determined electron density and a subsequent discussion will follow later in section 5.4.

The slight decrease of j_{H-} and n_{H-} in case of the electron attracting sheath is explained by the dominant production of H⁻ on the plasma grid: the main fraction of H⁻ is formed by conversion of neutral hydrogen atoms reaching the plasma grid with a thermal velocity of $T = 0.8$ eV (see section 2.2). If the potential of

the plasma grid is higher than the plasma potential, the transport of H$^-$ from the surface into the plasma is hindered. Since the sheath potential profile defines the energy gain or loss for surface produced H$^-$ particles, it influences the extraction probability of H$^-$ particles [33] as well as the transport inside the plasma – thus the correlation between $j_{\mathrm{H-}}$ and $n_{\mathrm{H-}}$ is not linear for varying bias voltage.

The optimum point of operation at the present magnetic filter field setup is with a bias applied leading to $U_{\mathrm{bias}} - \Phi_{\mathrm{pl}} \approx 0$ V: the amount of co-extracted electrons is reduced almost to its minimum whereas the extracted H$^-$ current density is not significantly reduced. The bias current at this favorable working point is about 13 A for the used operational parameters.

Influence on the vertical plasma asymmetry

A change of $U_{\mathrm{bias}} - \Phi_{\mathrm{pl}}$ leads to a variation of the electric field in axial direction, and thus has a direct effect on the vertical plasma drift, which is dominated by the $\vec{E} \times \vec{B}$ drift (see section 2.5). The dependence of the positive ion density at the three probe positions on the sheath potential profile is shown in figure 5.9, in which for the calculation of $U_{\mathrm{bias}} - \Phi_{\mathrm{pl}}$ the local plasma potential at each probe position is used. The positive ion density is about a factor of 3 higher at the top centered position compared to the top edge position and is slightly increased for higher values of the sheath potential profile at the top centered position, in contrast no significant change happens at the top edge position. The positive ion density decreases at the bottom edge position for higher values of the sheath potential profile. Hence, by comparison of the vertically symmetric edge positions, the plasma symmetry (which is defined in this work as the symmetry of the positive ion density) is slightly decreased for higher values of the sheath potential profile.

No direct determination of the vertical plasma asymmetry is possible at the centered position with the present setup, since only one probe is capable for centered measurements. However, it is known that the drift changes symmetrically by turning the magnetic filter field direction [36]. This means that the plasma at the top probe with drift down setting is the same as it would be at the bottom position with drift up setting, as long as similar source conditions (caesiation and operational parameters) are used for comparison. The present magnetic filter field setup allows turning the field direction in short time (10 minutes), thus the assumption of similar source conditions is valid. The resulting positive ion density for both drift directions is shown in figure 5.10: the plasma is almost
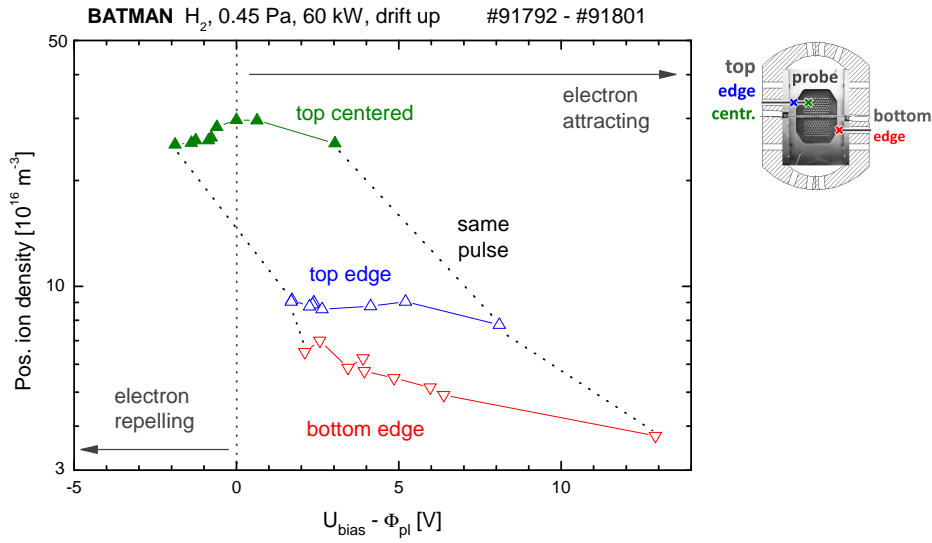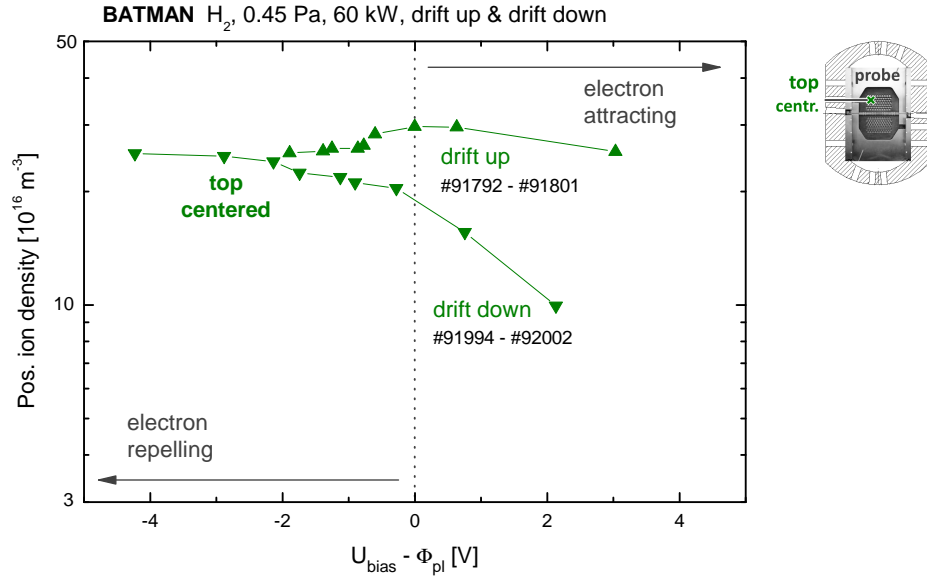
Figure 5.9: *Influence of the sheath potential profile on the positive ion density at the three probe positions.*

vertically symmetric for low values of the sheath potential profile, whereas the drift is enhanced for larger, positive values. The ratio of the positive ion densities becomes larger than two for $U_{\mathrm{bias}} - \Phi_{\mathrm{pl}} > 0$ V.

The comparison of the H_β line emissivity measured with the optical emission spectroscopy show similar trends of the vertical symmetry. Plotted in figure 5.11 is the emissivity at the top OES line of sight in dependence of the bias voltage, again for drift up and drift down setting. The vertical asymmetry of the emissivity is enhanced for higher bias values. For comparison with the Langmuir probe measurements, the following items have to be taken into account:

- Since the line-of-sight of the OES is not positioned in front of the plasma grid, but in front of the bias plate (which is at ground potential of the source, 0 V), the potential difference of the plasma to the bias plate is directly the plasma potential, which is – however – measured at a different position in front of the PG. For this reason, the bias potential is directly used as quantity for the horizontal axis.

- The LOS of the OES is less vertically centered compared to the Langmuir probe measurement positions, which means that a vertical drift is stronger pronounced at the LOS of the OES.

- The H_β emission scales with the electron density, whereas the positive ion density is measured by the Langmuir probes. Nevertheless, qualitative

Figure 5.10: *Influence of the sheath potential profile on the positive ion density at the top centered probe position in case of plasma drift up and down. The drift up and drift down case refer to different pulses with reversed magnetic filter field direction.*
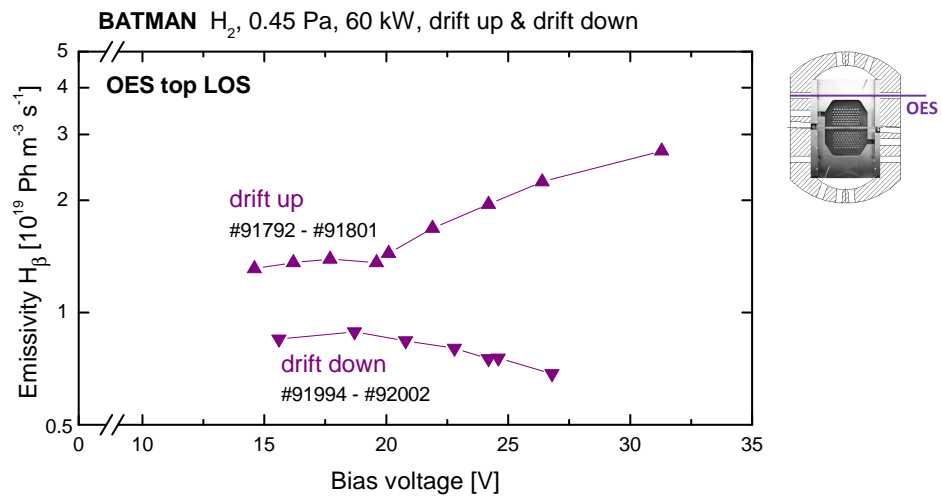
Figure 5.11: *Influence of the applied bias voltage on the H_β emissivity measured by OES for the same pulses as in figure 5.10.*

trends should be similar because H^- is distributed much more homogeneously compared to the plasma, as will be shown in section 5.3.

To summarize, the plasma shows a vertical asymmetry in the extended boundary layer of the prototype ion source. This asymmetry has to be taken into account for comparison of local measurements or LOS-averaged measurement of plasma parameters at a horizontal line-of-sight with the source performance, since the extracted currents are drawn from the large extraction area of the plasma grid. In addition, the vertical plasma asymmetry depends on the axial electric field, hence on the sheath potential profile and thus on the applied bias voltage.

Influence on the Cs distribution

Changes of the vertical plasma drift do not only influence the vertical plasma symmetry, but also as a second-order effect the symmetry of neutral Cs, if the PG bias is set to values differing from the standard, optimum value: the change of the Cs symmetry (defined in equation (4.1)) measured by the Cs absorption spectroscopy is shown in figure 5.12 as function of the bias voltage. For this measurement, the setup shown in figure 3.15 (b) has been in use, allowing the determination of the Cs^0 density at two horizontal LOS. Whereas at low bias voltages up to the standard operational point of the source neutral Cs is distributed almost symmetrically, the Cs^0 symmetry is clearly affected by the plasma drift at high bias values, where the neutral Cs density is up to 80% higher at the top LOS (which is in the plasma drift direction in this case). The reason for this behavior is that with increasing plasma asymmetry Cs is released from vertically less centered Cs reservoirs from the wall. Hence, after operation of several plasma pulses at a high bias voltage, an increasing Cs symmetry would be expected due to the redistribution in plasma phases – this behavior has not yet been investigated and is thus a task for future work.

Consequence for the investigation of plasma dynamics

It was shown that the plasma grid bias influences the plasma homogeneity in the extended boundary layer due to a change of the axial electric field and subsequently a change of the $\vec{E} \times \vec{B}$ drift. Regarding the effect of the bias on the source performance, the difference $U_{\text{bias}} - \Phi_{\text{pl}}$ is the driving parameter, describing the potential profile in the sheath.
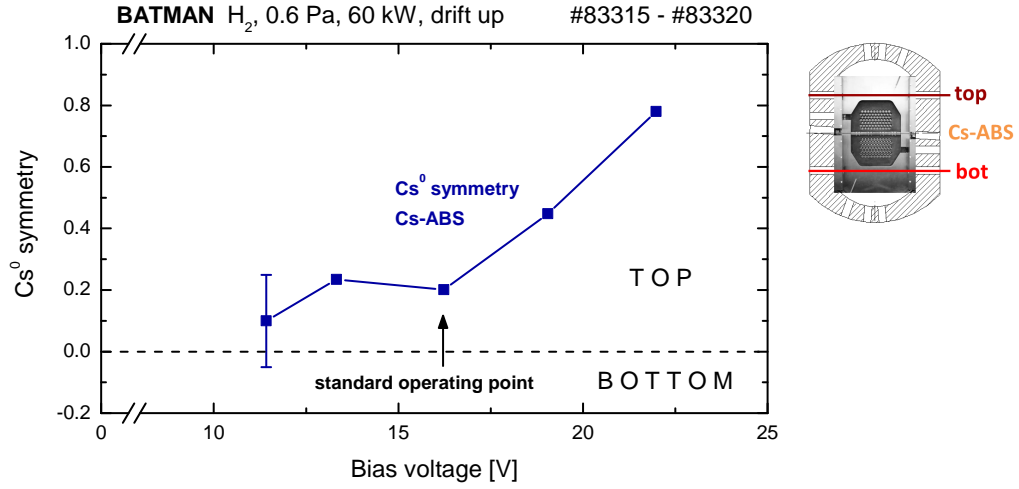
Figure 5.12: *Influence of the applied bias voltage on the vertical asymmetry of neutral Cs. Indicated is the favorable operating point with high source performance (not shown here) at the corresponding operational parameters and source condition.*

Since this value does only change by some volts for typically applied bias values, accurate measurement of the plasma potential Φ_{pl} at a relevant position in front of the plasma grid is of high importance. For this reason, the usage of the compensated probe is mandatory, since the non-compensated probe leads to a wrongly determined plasma potential due to the influence of RF oscillations (see section 3.3).

5.3 Qualitative comparison of the plasma and H⁻ homogeneity

Important for the source operation is to extract a homogeneous ion beam out of the ion source. Thus, a homogeneous distribution of H⁻ inside the source is required.

By comparison of the symmetry of the probe characteristic at different positions, qualitative statements regarding the homogeneity of the plasma and H⁻ can be made, as the shape of a Langmuir probe characteristic depends on the fraction of the negative ion density in respect to the electron density $n_{\mathrm{H^-}}/n_{\mathrm{e}}$. A symmetric characteristic indicates that H⁻ is the dominant negatively charged particle ($n_{\mathrm{H^-}}/n_{\mathrm{e}} \gg 43$ or $n_{\mathrm{D^-}}/n_{\mathrm{e}} \gg 61$, respectively), whereas a classical characteristic is formed with electrons being the dominant negatively charged particle ($n_{\mathrm{H^-}}/n_{\mathrm{e}} \ll 43$ or $n_{\mathrm{D^-}}/n_{\mathrm{e}} \ll 61$, respectively).
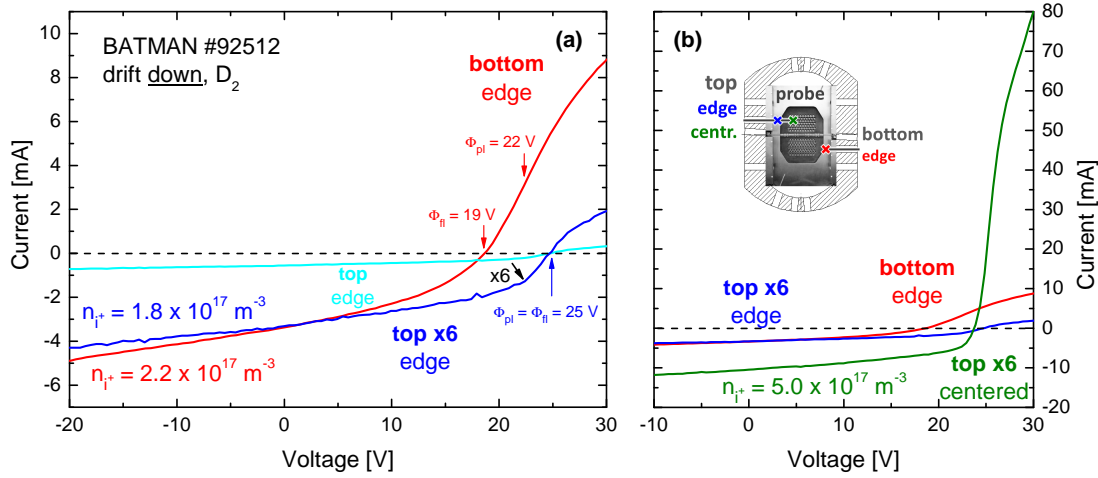
Figure 5.13: *Comparison of Langmuir probe characteristics for one pulse with plasma drift down: (a) for the probes (top and bottom) at the vertical symmetric edge position and (b) showing additionally the top probe at the centered position.*

Shown in figure 5.13 are Langmuir probe characteristics at the three measurement positions in the source. The characteristics have been recorded at a well conditioned source during deuterium operation. Similar measurements leading to the same result are also available for hydrogen operation (but not shown in this work). The magnetic filter field was arranged to a resulting downward vertical plasma drift. The current of the top probe is shown additionally scaled by a factor of six in order to compensate the smaller probe tip area compared to the bottom probe (the tip radius is three times smaller, the length is two times smaller) – this scaling has no effect on the determination of the plasma parameters, but simplifies the qualitative comparison.

Figure 5.13 (a) shows the characteristics at the vertical symmetric edge positions. Whereas the positive ion part differs only little with a slightly higher drawn positive ion current of 'bottom' compared to 'top x6', the characteristics differ strongly for positive applied voltages: 'top x6' is almost symmetric (the symmetry point at the plasma potential is shifted to positive voltages due to the applied bias voltage of 25 V), whereas 'bottom' shows a higher drawn electron current. The slightly higher positive ion density at the bottom position (2.2×10^{17} m^{-3}) compared to the top position (1.8×10^{17} m^{-3}) is a result of the downward plasma drift.

This simple qualitative observation leads to the conclusion that the ratio $n_{\mathrm{D}^-}/n_\mathrm{e}$ must be larger at the top position (contrary direction to the plasma drift) compared to the bottom position and thus that H$^-$ must be vertically distributed either more homogeneously or inhomogeneous in counter direction

($n_{\mathrm{H-}}$ higher in the top part compared to the bottom part) to the plasma density – measured at an axial distance of 7 mm to the plasma grid. This result agrees well with modeling results showing that the main fraction of H$^-$ is converted out of neutral H atoms [25]. Since atoms are mainly created in the hot driver plasma, they are not affected by the plasma drift inside the expansion region. However, an inhomogeneous distribution of negative hydrogen ions can take place if either the surface production is space-charge limited due to a too low amount of positive charges for space charge compensation (see section 2.4), or if the destruction processes with plasma particles become relevant in the extended boundary layer. Also an inhomogeneous work function of the plasma grid due to insufficient Cs coverage would result in an inhomogeneous H$^-$ distribution. However, measurements of the beam homogeneity at MANITU showed no clear correlation with the plasma homogeneity in the source, with the beam instead being more homogeneous compared to the plasma [88]. Thus, the measurements shown here are in good agreement.

The absolute number of $n_{\mathrm{D-}}$ can be derived from the symmetric characteristic at the top edge position, where $n_{\mathrm{D-}} \approx n_{\mathrm{i+}} = 1.8 \times 10^{17}$ m^{-3}. This agrees well to the CRDS measurement of $n_{\mathrm{D-}} = 1.0 \times 10^{17}$ m^{-3} during the same pulse, when taking into account the uncertainty in the absolute evaluation of the positive ion density discussed earlier.

The observations discussed up to now are carried out at the edge position close to the sidewall. More centered, in front of the plasma grid, the flux of negatively charged particle is – due to the higher positive ion density of 5.0×10^{17} m^{-3} – dominated by electrons. Comparison of the edge and centered position (figure 5.13 (b)) shows that H$^-$ is distributed also horizontally more homogeneous compared to the positive ion density (symmetric curve at the edge position, asymmetric at the centered position).

Although not shown within this work, it should be mentioned that the shape of the Langmuir probe characteristic differs not only at different locations, but changes also during the Cs conditioning process, starting with a classical, asymmetric shape, which becomes more and more symmetric at not-centered positions [78]. This effect is attributed to the increasing fraction of negative hydrogen ions during the Cs conditioning process.

# 5.4 Influence of the source pressure and isotope

Bias scans have been carried out for two different source pressures (0.45 Pa and 0.6 Pa) in hydrogen and deuterium. Because changes of the plasma parameters lead to changes in the plasma potential, a constant value of the bias voltage is not necessarily sufficient for a comparison, since the latter is only reasonable at the same sheath characteristics close to the plasma grid, i.e. at the same value of $U_{\mathrm{bias}} - \Phi_{\mathrm{pl}}$.

For all shown parameter scans, the Cs evaporation rate out of the oven has been chosen in order to achieve the optimum performance of the source. The source performance was stable before and after each parameter scan. Hence, a constant work function of the plasma grid is expected during each scan.

Dependence on the source pressure

The influence of the sheath potential profile on several source quantities, i.e. (a) the extracted current densities, (b) the bias current, (c) the positive ion density at the top centered position, (d) the electron temperature at the same position, (e) the plasma homogeneity at the edge positions of the probes and (f) the H^- density, is shown in figure 5.14 for a source pressure of 0.45 Pa and 0.6 Pa in hydrogen operation. For determination of $U_{\mathrm{bias}} - \Phi_{\mathrm{pl}}$, the plasma potential measured with the RF compensated top probe at the centered position in front of the extraction apertures is used. The following trends are identified:

(a) The extracted H^- current density is only slightly influenced by the sheath potential profile and not significantly dependent on the source pressure. In contrary, the amount of co-extracted electrons is decreased for increasing values of the sheath potential profile in the electron repelling case and is stable in the electron attracting case. This behavior has been already shown in figure 5.8. The amount of co-extracted electrons is higher at the lower source pressure independent on the sheath potential profile.

(b) The bias current increases for larger values of the sheath potential profile with saturation at high values of the sheath potential profile, as already shown in figure 5.5. A larger bias current is drawn at 0.6 Pa.

(c) The positive ion density – measured with the top probe at the centered position – shows the typical behavior (compare with figure 5.10) with a
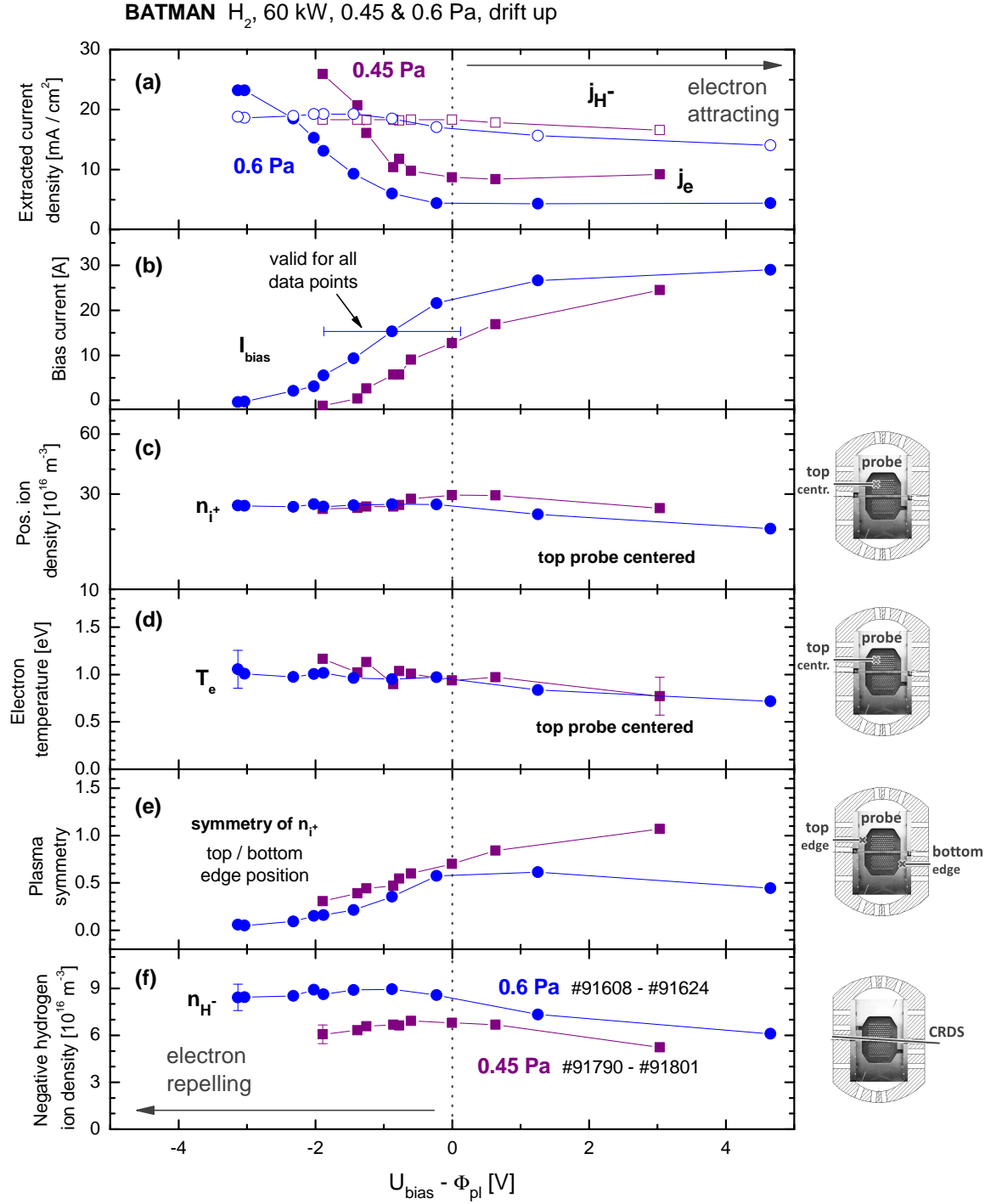
Figure 5.14: *Dependence of several source quantities on the sheath potential profile, comparing two source pressures in hydrogen operation: (a) source performance, (b) bias current, (c) positive ion density, (d) electron temperature, (e) plasma symmetry, (f) negative hydrogen ion density.*

slight increase for larger values of the sheath potential profile due to the increase of the vertical plasma drift. Almost no difference takes place for varying source pressure.

(d) No significant change of the measured electron temperature (top probe centered position) happens neither for varying sheath potential profile nor for the different source pressures.

(e) For the plasma symmetry, the definition in equation (4.1) is used with the positive ion density measured at the top and bottom edge position. The vertical asymmetry is increased at higher values of the sheath potential profile due to the increasing plasma drift. Regarding the different source pressures, no significant deviation occurs for $U_{\mathrm{bias}} - \Phi_{\mathrm{pl}} < 0$ V, whereas in case of $U_{\mathrm{bias}} - \Phi_{\mathrm{pl}} > 0$ V the plasma is more symmetric at higher source pressure.

(f) The negative hydrogen ion density shows a similar dependence on the sheath potential profile for both source pressures (in particular a decrease at a high value of the sheath potential profile, compare with figure 5.8). However, $n_{\mathrm{H^-}}$ is larger at higher source pressure. This dependence of the negative hydrogen ion density on the varying source pressure has been already discussed in section 5.1.

The reason for the different amount of co-extracted electrons as well as the drawn bias current for different source pressures is complex: at first glance, when co-extracting a larger amount of electrons at low pressure, a larger flux of electrons towards the extraction apertures would be expected. However, since the positive ion density as well as the electron temperature is similar at both source pressures and the difference of the negative hydrogen ion density (about 2×10^{16} m^{-3}) is one order of magnitude lower than the positive ion density, the local electron flux (at the top probe inside position, 7 mm distance to the PG) shows no significant difference. Of course it has to be taken into account that the plasma parameters are measured locally and the extracted currents are averaged over the full size of the extraction apertures – however, the plasma symmetry measured at the edge positions of the probes shows at least for the electron repelling case no significant pressure dependence.

Thus, the probe measurement show similar electron fluxes towards the plasma grid. However, the distribution of electron fluxes is changing: when considering

only the axial component of the electron flux (towards the plasma grid), electrons can either penetrate the sheath at the plasma grid and thus hit the plasma grid (counting to the bias current), or reach the plasma meniscus of an extraction aperture leading to its extraction, or they are reflected back towards the source due to a repelling electric field in the sheath or due to collisions. Two effects regarding this distribution are indicated in figure 5.14 (a) and (b): at higher values of the sheath potential profile, a larger fraction of electrons is collected by the plasma grid whereas a lower amount is extracted. The second effect takes place for varying source pressure: at higher source pressure, the bias current is increased whereas the amount of co-extracted electrons is decreased.

In the following, the electron flux in the extended boundary layer is compared quantitatively with the sum of the bias and co-extracted electron current. As a favorable operational point of the source for the present magnetic filter field setup, the setting $U_{\text{bias}} - \Phi_{\text{pl}} = 0$ V in figure 5.14 is chosen. The measured parameters (linearly interpolated) are listed in table 5.1. However, as already discussed, the bias current at this setting does not only consist of electrons, but also of positive ions. Thus, for comparison of electron fluxes, the maximum drawn bias current $I_{\text{bias,max}}$, in which positive ions collected on the PG play a minor role, is chosen. However, since especially in the 0.45 Pa case saturation is not yet completely reached at the maximum applied bias voltage, $I_{\text{bias,max}}$ is erroneous by some amperes.

Further on, the assumption of $n_{\text{e}} = n_{\text{i}+} - n_{\text{H}-}$ is taken, although the negative hydrogen ion density is measured line-of-sight integrated at a slightly different position. Calculation of the electron current flux towards the plasma grid ($j_{\text{e}} = \frac{1}{4}n_{\text{e}}e\bar{v}$) yields 575 $^{\text{mA}}/_{\text{cm}^2}$ for 0.45 Pa and 448 $^{\text{mA}}/_{\text{cm}^2}$ for 0.6 Pa, respectively. For the total size of the uncovered plasma grid including the area of the extraction apertures (426 cm^2 + 63 cm^2 = 489 cm^2) this yields a current of 275 A for 0.45 Pa and 219 A for 0.6 Pa, being about one order of magnitude larger than the sum of the small co-extracted electron current and large bias current (25 A for 0.45 Pa and 29 A for 0.6 Pa). The difference can be caused by the following reasons:

- For the calculation of the electron flux, the plasma parameters of the top probe at the centered position are used – due to the plasma drift towards the upper side, the total electron flux is overestimated. To quantify the amount of overestimation, the mean positive ion density in figure 5.9 (b) is chosen: $n_{\text{i}+} = 0.5 \times (2.9 + 1.9) \times 10^{17}$ m^{-3} (0.45 Pa case). This yields with the same estimations as above a reduced electron current of 145 A (in

Table 5.1: *Measured parameters (figure 5.14) at $U_{\mathrm{bias}} - \Phi_{\mathrm{pl}} = 0$ V for the source pressure of 0.45 Pa and 0.6 Pa.*

Parameter	0.45 Pa	0.6 Pa
I_{e}	0.55 A	0.28 A
$I_{\mathrm{bias,max}}$	24.5 A	29.0 A
$n_{\mathrm{i+}}$	2.9×10^{17} m^{-3}	2.6×10^{17} m^{-3}
$n_{\mathrm{H^-}}$	6.8×10^{16} m^{-3}	8.4×10^{16} m^{-3}
T_{e}	0.9 eV	0.9 eV

comparison to 275 A) – still being a factor of six larger than the sum of co-extracted electron current and bias current.

- The calculated electron current in the extended boundary layer is only valid for a uniform velocity distribution. Due to the magnetic field consisting of the filter field and the electron deflection field and the subsequent magnetization of electrons, the axial flux towards the plasma grid is hindered. As shown in figure 2.11, the strength of the electron deflection field is increasing strongly towards the PG at an axial distance below 1 cm, resulting in a complex field topology and thus in a complex transport.

As assumption of the lower limit of the electron flux towards the plasma grid, the electron transport is considered perpendicular to the magnetic field lines – thus, magnetic field components in axial direction are neglected. The electron diffusion velocity is estimated as $v_{\mathrm{diff}} = r_{\mathrm{L}} \nu$, since an electron is transported by a mean value of one Larmor radius each collision. For the collision frequency ν, Coulomb collisions with positive and negative ions and elastic collisions with H and H$_2$ are taken into account. Coulomb collisions with electrons are not considered, because they lead to no net transport perpendicular to the magnetic field [34]. The Coulomb collision frequency of electrons with ions ν_{ei} is given by [89]

$$\nu_{\mathrm{ei}} = \frac{\sqrt{2} Z^2 e^4 n_{\mathrm{i}} \ln \Lambda}{12 \pi^{3/2} \epsilon_0^2 \sqrt{m_{\mathrm{e}}} \left(k_{\mathrm{B}} T_{\mathrm{e}} \right)^{3/2}}, \tag{5.2}$$

with the charge number Z of the ion and the Coulomb logarithm $\ln \Lambda = \ln \left[12 \pi \left(\epsilon_0 k_{\mathrm{B}} T_{\mathrm{e}} \right)^{3/2} / \left(e^3 n_{\mathrm{e}}^{1/2} \right) \right]$. The frequency of elastic collisions is given by $\nu_{\mathrm{eH}_x} = X_{\mathrm{eH}_x} n_{\mathrm{H}_x}$, with the rate coefficient X_{eH_x} of elastic electron collision with H or H$_2$, respectively. The rate coefficients have been calculated by [27]

using cross sections from [90, 91, 92]. With the measured plasma parameters of the 0.45 Pa case and the mean positive ion density discussed in the item above, this results in

$$\nu = \nu_{\mathrm{ei+}} + \nu_{\mathrm{ei-}} + \nu_{\mathrm{eH}} + \nu_{\mathrm{eH_2}} = (8.5 + 2.5 + 0.9 + 2.2) \times 10^6 \text{ Hz} = 1.4 \times 10^7 \text{ Hz}.$$

The magnetic field strength of 4 mT in axial distance of 7 mm to the PG yields a Larmor radius of the electrons of $r_{\mathrm{L}} = 0.8$ mm (equation (2.9)). Thus, the electron diffusion velocity is estimated to $v_{\mathrm{diff}} = 1.2 \times 10^4$ m/s. This results in an electron current density of $j_{\mathrm{e}} = 33$ mA/cm^2 and a total electron current of 16 A, which is slightly lower than the sum of co-extracted electron current and bias current (25 A), but much closer than the assumption of isotropic electron fluxes. Already this estimation shows the importance of magnetization for the electron transport close to the PG.

- An axially increasing H$^-$ density towards the PG due to the dominance of surface production and subsequent diffusion would result in a decrease of the electron density towards the plasma grid in order to sustain quasi-neutrality. However, as discussed in section 5.1, experiments in a similar source revealed no significant increase of $n_{\mathrm{H-}}$ towards the PG [87] at an axial distance of 2 mm and 24 mm.

Consequently, the electron dynamics influencing the distribution of electrons either towards the sheath of the plasma grid (and thus to the bias current) or to the plasma meniscus (and thus to the co-extracted electron current) is controlled by the transport in the magnetic field close to the PG, which consists of a complex 3D shape. Access to the subsequently complex fluxes is however only possible by usage of modeling codes and not by diagnostics – nevertheless, it can be stated that the structure of the magnetic field close to the PG is expected to have a direct influence on the electron dynamics.
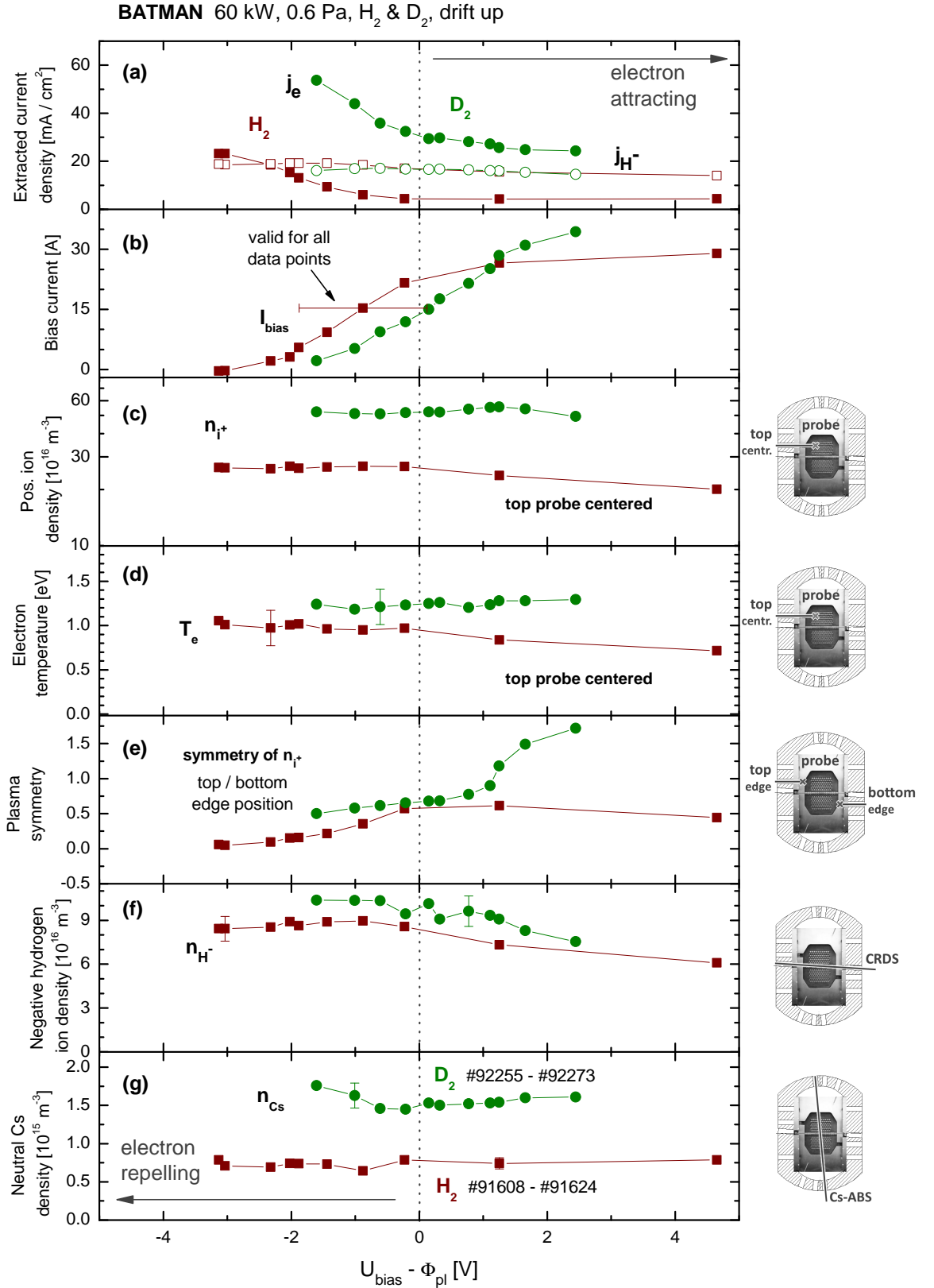
Comparison of hydrogen and deuterium

Bias scans for the comparison of hydrogen and deuterium operation have been carried out at the same two source pressures shown before. Figure 5.15 shows the comparison for a source pressure of 0.6 Pa, the comparison at the source pressure of 0.45 Pa, which is closer to the requirement of the ITER source, is then followed in figure 5.16. The data points for hydrogen are the same as in figure 5.14

– however, to ease the comparison, they are plotted again in the following figures. The lowest possible value of the sheath potential profile is limited by the larger amount of co-extracted electrons in deuterium operation. Thus, the accessible range of $U_{\mathrm{bias}} - \Phi_{\mathrm{pl}} < 0$ V is smaller in deuterium operation compared to hydrogen.

Since the relative behavior of the plasma parameters for varying sheath potential profiles have been already discussed in detail, only the deviation between hydrogen and deuterium is considered. The following trends can be identified at $p_{\mathrm{source}} = 0.6$ Pa (figure 5.15):

(a) Whereas the amount of extracted H$^-$ and D$^-$ current density is almost similar, a much larger amount of electrons is co-extracted in deuterium operation – the minimum value of j_{e} is increased from 4.3 mA/cm^2 in hydrogen by a factor of almost six to 24.3 mA/cm^2 in deuterium. This well-known behavior triggered the demand of a detailed comparison. Both isotopes show the same relative trend for varying sheath potential profile.

(b) The bias current shows the same behavior and a similar value for both isotopes, when considering the error bar of the determined plasma potential and thus sheath potential profile. However, the maximum drawn current is slightly increased in deuterium operation.

(c) The positive ion density at the top centered position is about two times higher in deuterium, independent on the sheath potential profile.

(d) The measured electron temperature is increased from about 1.0 eV to 1.2 eV in deuterium operation, independent on the sheath potential profile. However, the limitations of the electron temperature measurement with the Langmuir probe, which have been discussed in section 3.3, must be taken into account.

(e) The vertical plasma symmetry is similar for $U_{\mathrm{bias}} - \Phi_{\mathrm{pl}} < 1$ V, whereas at higher values positive ions are distributed less homogeneous in deuterium.

(f) The negative ion density is higher in deuterium with a difference of about 1.5×10^{16} m^{-3}, which is almost independent on the sheath potential profile.

(g) The neutral Cs density is higher in deuterium. This is a direct result of the experimental observation that a higher Cs evaporation rate is necessary in deuterium in order to achieve the optimum source performance. Due

Figure 5.15: *Dependence of several source quantities on the sheath potential profile, comparing hydrogen and deuterium at 0.6 Pa: (a) source performance, (b) bias current, (c) positive ion density, (d) electron temperature, (e) plasma symmetry, (f) negative hydrogen ion density, (g) neutral Cs density.*

Table 5.2: *Plasma parameters inside the driver at $p = 0.6$ Pa, $P = 70$ kW for hydrogen and deuterium operation [35].*

Parameter	H_2	D_2
n_H/n_{H_2}, n_D/n_{D_2}	0.37	0.49
n_e	0.67×10^{18} m^{-3}	0.80×10^{18} m^{-3}
T_e	9 eV	7.5 eV

to averaging along a vertical LOS, there is no dependence on the sheath potential profile.

A similar amount of extracted H^- and D^- current density requires the same flux of produced negative ions at the plasma grid, whereas due to the higher mass and thus reduced particle velocity the density of negative ions is increased in the extended boundary layer – the measurement agrees with this consideration, as already discussed in section 5.1.

Regarding the amount of produced negative ions, it is necessary to characterize the flux of H and H^+ from the driver towards the plasma grid. Since dissociation of hydrogen molecules and ionization of hydrogen mainly takes place in the hot driver plasma, the comparison of plasma parameters in the driver is desirable between hydrogen and deuterium operation. The characterization of the driver plasma by means of OES at the axial LOS through the driver has been carried out in the past [35] for the source pressure of 0.6 Pa; however, at an slightly elevated applied RF power of 70 kW. Nevertheless, a qualitative comparison between hydrogen and deuterium is possible and also valid for the measurement campaign shown in figure 5.15. The resulting plasma parameters are listed in table 5.2.

The density ratio n_H/n_{H_2} of hydrogen molecules is significantly higher in deuterium compared to hydrogen operation (0.49 compared to 0.37). Also the electron density is increased in deuterium (0.80×10^{18} m^{-3} compared to 0.67×10^{18} m^{-3}), whereas the electron temperature is slightly decreased (7.5 eV compared to 9 eV). For the same dissociation degree, the flux of dissociated conversion particles towards the plasma grid would be reduced by a factor of $\sqrt{2}$ in deuterium due to the doubled mass. However, the larger dissociation degree in deuterium can at least partly compensate the mass difference, resulting in similar fluxes of conversion particles towards the plasma grid. This result is in good agreement with the almost similar amount of extracted negative ions in hydrogen and deuterium as well as with the increased D^- density compared to H^-: because $\Gamma = nv \propto m^{-0.5}$, a similar

flux of surface-produced negative hydrogen ions $\Gamma_{H^-} \approx \Gamma_{D^-}$ results in $n_{D^-} > n_{H^-}$ – being in good agreement with the measurement shown in figure 5.15 (f).

A clear isotope effect happens for the positive ion density in the extended boundary layer, which is almost doubled in deuterium operation. The plasma parameter in the driver show the same trend, with a slightly higher electron density in deuterium. The amount of negative hydrogen ions in the driver is not significant, leading to $n_e = n_{i^+}$. The increase of the positive ion density in the extended boundary layer is more pronounced than the increase of the negative hydrogen ion density, resulting in an increased electron density in D_2 operation. In combination with the similar plasma symmetry at low values of the sheath potential profile, the flux of electrons from the extended boundary layer towards the plasma grid is larger in deuterium.

As stated before, the transport of electrons towards the PG in the magnetic field with complex 3D structure in the volume close to the PG is complex. Thus, only qualitative statements can be made. The increased electron flux leads to a highly increased amount of co-extracted electrons in combination with a slightly increased maximum bias current in deuterium operation compared to hydrogen. The reason for this differing current distribution is however not experimentally accessible for diagnostics, as mentioned before.

The comparison of the same quantities in both isotopes at a source pressure of 0.45 Pa is shown in figure 5.16. Similar trends as for 0.6 Pa can be identified, however, with the following exceptions: (a) j_{D^-} is slightly lower than j_{H^-}, (b) the bias current is significantly larger in deuterium operation, (f) the negative hydrogen ion density is similar and thus not increased in D_2 and (g) the neutral Cs density is lower in deuterium operation. In particular the lower Cs density shows that the source has not been optimal conditioned, resulting in a lower production rate of D^-, hence to an increased fraction of electrons n_e/n_{D^-} and thus to the different behavior (a), (b) and (f).

However, the main statement regarding the co-extraction of electrons, what was made for the 0.6 Pa case above, is still valid at 0.45 Pa: the amount of co-extracted electron current is strongly increased in D_2 (a), the positive ion density in front of the extraction apertures (c) as well as the measured electron temperature at the same position (d) is increased, whereas the vertical plasma symmetry (e) is similar for both isotopes. The resulting increased electron flux in the extended boundary layer is balanced by a larger amount of co-extracted electrons in combination with an increased bias current.
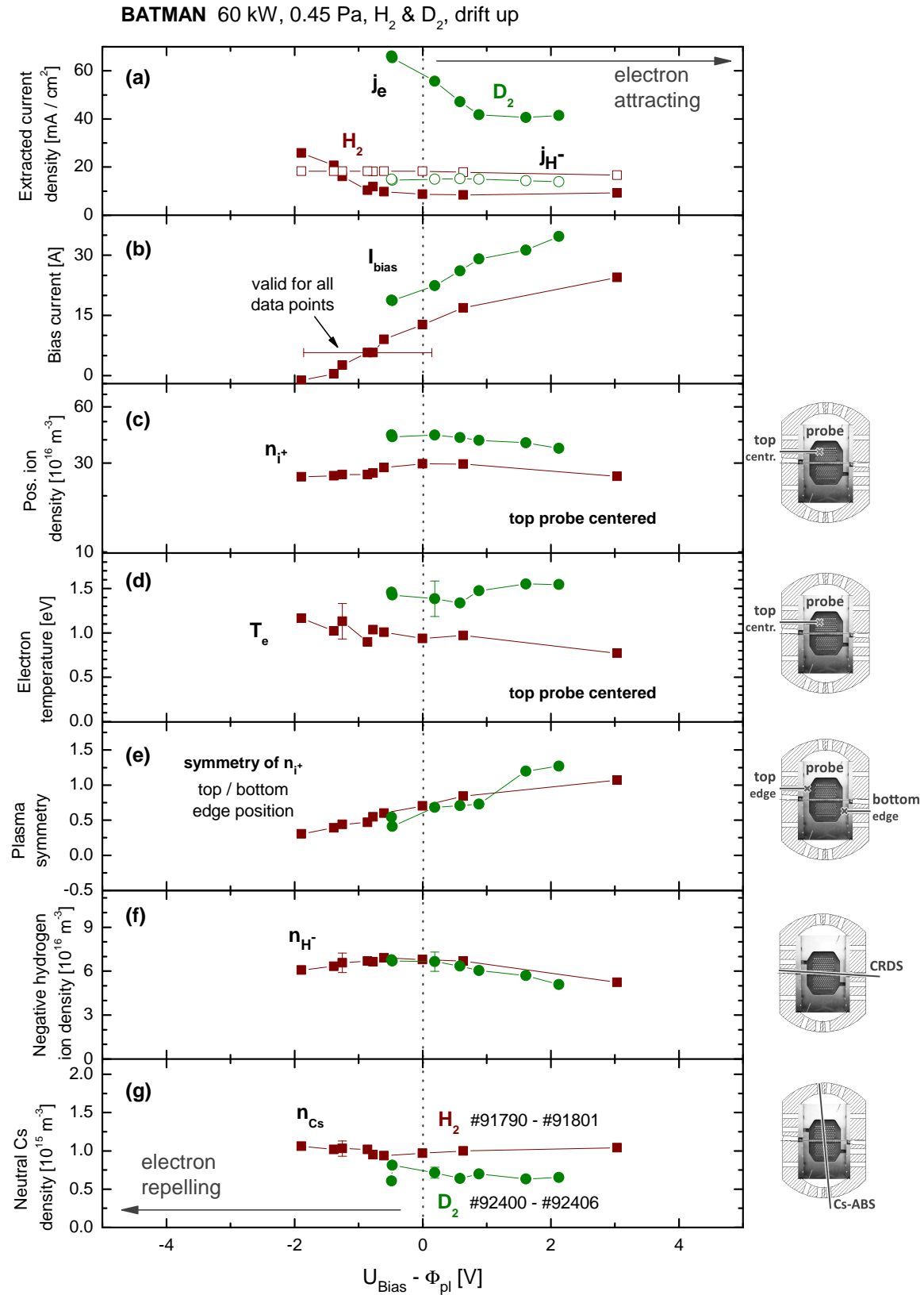
Figure 5.16: *Dependence of several source quantities on the sheath potential profile, comparing hydrogen and deuterium at 0.45 Pa: (a) source performance, (b) bias current, (c) positive ion density, (d) electron temperature, (e) plasma symmetry, (f) negative hydrogen ion density, (g) neutral Cs density.*

5.5 Conclusion

The applied bias to the plasma grid influences the sheath potential profile $U_{\text{bias}} - \Phi_{\text{pl}}$, what leads to a variation of the $\vec{E} \times \vec{B}$ drift and thus to a change of the vertical plasma symmetry. In addition, due to the transition from an electron repelling to an electron attracting sheath in the applied bias voltage range, the drawn bias current reacts sensitive on the applied bias voltage and thus also the amount of co-extracted electrons, which is reduced to its minimum in case of an electron attracting sheath.

The extracted H^- current density correlates almost linearly with the H^- density during Cs conditioning as well as for varying RF power, what shows a clear connection of plasma parameters in the extended boundary layer with the source performance.

A qualitative correlation exists between the sum of bias current and co-extracted electron current with the electron density, investigated for varying source pressure and isotopes. Quantitatively it was seen that the hindered transport of electrons in the magnetic field is the key parameter for the lowered sum of bias current and co-extracted electron current. Thus, the distribution of electron fluxes between bias current and co-extracted electron current is controlled by the magnetic field close to the plasma sheath and extraction meniscus. A deeper inside into the complex distribution can only be obtained by modeling codes, which is an ongoing task.

Nevertheless, the increased amount of co-extracted electrons in deuterium operation compared to hydrogen is a consequence of the increased electron density in the extended boundary layer. This result is in good agreement with a former characterization of the driver plasma, where a slightly increased electron density has been observed in deuterium operation. The increased dissociation degree of deuterium molecules compared to hydrogen results in a similar extracted negative ion current density in both isotopes, if the source is optimal conditioned.

6 Outlook towards larger sources

The results of this work, carried out at the small prototype source, lead to predictions for larger fusion relevant negative hydrogen ion sources. With the improved understanding of the Cs dynamics, the following consequences are expected:

- Homogeneous Cs evaporation is less important due to the homogenizing effect of the Cs distribution during plasma phases and subsequently homogeneous fluxes of Cs towards the PG. Thus, the position of the Cs oven(s)[25] and the design of their evaporation nozzle may be of minor importance in order to achieve homogeneous Cs conditions on the plasma grid. However, there are some boundary conditions, i.e. the avoidance of large Cs losses through the grid in order to sustain the high voltage holding of the extraction system.

- Sufficient Cs reservoirs at the source walls are required during long pulses in order to sustain stable Cs conditions. The long-pulse Cs dynamics at MANITU was controlled by the undesired release of Cs from the heat-up of the not actively cooled bias plate. Thus, ELISE is the first test facility, at which the long-pulse Cs dynamics under ITER relevant conditions can be investigated. Sustaining a sufficient flux of Cs towards the PG in order to sustain a stable and low work function will be a challenging aim for the future. Furthermore, the increasing ratio between plasma volume and wall area at larger sources might lead to differences in the Cs dynamics during plasma phases and thus to the required amount of Cs reservoirs and Cs evaporation.

In addition, the results regarding the plasma dynamics in the extended boundary layer lead to the following predictions:

- Changes of the vertical plasma symmetry, which is influenced by $\vec{F} \times \vec{B}$ drifts, are expected, because the magnetic filter field topology is necessarily

---

[25]The use of multiple Cs ovens is planned for the ITER source. Two ovens are used at ELISE.

differently shaped at the larger sources: a sufficiently large magnetic field strength in the horizontal center of the source cannot be generated by permanent magnets due to the increased source width, and is thus created by applying a vertical electrical current at the plasma grid.

- Not much difference regarding the extraction of a homogeneous negative hydrogen ion beam is expected due to the size scaling. As has been shown, H^- is distributed more homogeneously inside the prototype source compared to the plasma because of the high relevance of conversion out of hydrogen atoms. However, the challenge of achieving a homogeneous and temporally stable low work function at the plasma grid mentioned above remains.

- The amount of co-extracted electrons, the bias current and its distribution between these two quantities is expected to be sensitive on the magnetic field topology close to the plasma grid. As mentioned above, the filter field differs at the larger sources, with a horizontally more homogeneous distribution in front of the PG and no steep positive gradients towards the side wall, avoiding effects caused by a magnetic mirror.

- The bias current and as a consequence the amount of co-extracted electrons reacts very sensitive on the potential profile in the plasma sheath of the PG and thus on the bias voltage. The sheath potential profile can however differ locally in large sources, if the plasma potential is not homogeneous in front of the PG. The optimum operational point could not be achieved homogeneously in front of the PG in this case. Hence, the determination of the plasma potential with some spatial resolution is a desirable task in larger sources.

- A similar behavior is expected regarding the difference between deuterium and hydrogen operation at the larger sources compared to the prototype source, i.e. a similar amount of extracted negative ions in combination with an increased amount of co-extracted electrons in deuterium, because the observed difference is attributed to changes of the driver plasma.

These predictions are presently investigated at the ELISE test facility.

7 Summary

The neutral beam injection system of the upcoming ITER fusion experiment is based on the production, acceleration and neutralization of negative hydrogen ions. The development of large-scale (0.2 m^2 extraction area at a size of 1×2 m^2) sources for negative hydrogen ions fulfilling the ITER requirements is an ongoing and challenging task. A prototype source has been developed successfully at IPP Garching, which has roughly $^1/_8$ the size of the ITER source. The main production of H$^-$ takes place by surface conversion of hydrogen atoms and ions, produced in a hydrogen plasma, on a caesiated grid. Due to the high chemical reactivity of Cs in combination with the vacuum conditions inside the source and pulsed plasma operation (a pulse length of up to one hour is required for ITER), a complex Cs dynamics takes place. Gaining a deeper insight into the Cs dynamics was one aim of this work, since, especially for the design and operation of upcoming larger sources, knowledge about the requirement of homogeneous Cs evaporation and the determination of the optimum Cs evaporation rate is desirable.

The ITER requirements have been fulfilled by the small prototype sources, although not simultaneously in one source. Open issues are the size scalability towards the full-size ITER source as well as the amount of inevitably co-extracted electrons in long deuterium pulses: co-extracted electrons are removed from the particle beam by magnets bending the electrons onto the extraction grid creating a local heat load. The maximum acceptable heat load is technologically limited by the cooling capabilities, leading to a limitation of the tolerable amount of co-extracted electrons. Experimentally observed is a higher amount of co-extracted electrons in deuterium compared to hydrogen operation. This forms in particular a problem during long pulses, where an increase of the amount of co-extracted electrons is usually observed after several minutes. A reduction of the co-extracted electron current would be desirable also for sources beyond ITER, because then a larger amount of negative ions could be extracted using a higher extraction voltage or an increased power for plasma generation.

Since the amount of co-extracted electrons is a crucial parameter for the source

performance, some effort is taken for its reduction: on the one hand, the plasma production is separated from the conversion grid by an expansion chamber with a magnetic filter field. The hot and dense driver plasma ($T_e \approx 10$ eV, $n_e \approx 10^{18}$ m^{-3}), required for dissociation of hydrogen molecules and ionization processes, is cooled down in electron temperature and density by one order of magnitude each towards the conversion grid – cooling down the electron temperature is not only required for the reduction of the amount of co-extracted electrons, but also to reduce the destruction of H$^-$ particles by electron stripping. In addition, a positive bias voltage of the conversion grid with respect to the source walls reduces the amount of co-extracted electrons. Thus, the important physics of such a source takes place at the downstream side of the magnetic filter close to the plasma grid (this region is called extended boundary layer): the production of H$^-$, its transport through the plasma and its extraction through the grid in combination with electrons out of the plasma. Experimental comparisons of the plasma dynamics in the extended boundary layer with the extracted currents in hydrogen and deuterium operation are eligible in order to find correlations and thus to gain a better understanding of relevant plasma parameters for achieving high source performance.

As main diagnostic for the investigation of the Cs dynamics in this work, a tunable diode laser absorption spectroscopy system for the determination of the neutral Cs density during plasma and vacuum phases has been applied at the prototype ion source at up to two lines of sight, allowing the measurement of the Cs density with some vertical spatial resolution. The latter is of importance, since the prototype ion source has an intrinsic asymmetry with only one Cs oven mounted in the top part. For the operation of the source, a spatial homogeneous and temporal stable work function of the conversion grid is required. A former determination of the work function in a lab experiment under similar vacuum and Cs conditions revealed that the prototype ion source operates with a work function of bulk Cs (2.14 eV) and thus the Cs coverage of the conversion grid is at least several monolayers thick if the source is well conditioned. Although a homogeneous distribution of Cs is not necessarily required in order to achieve a homogeneous work function in this case, it helps nonetheless to reduce the amount of required Cs evaporation and is thus desirable.

Detailed experimental studies have been carried out in this work regarding the strong difference in the Cs dynamics between vacuum and plasma phases: the Cs density in vacuum phases is determined by the evaporation of Cs as the source and chemical sticking on the wall as the sink, with a typical line-of-sight integrated Cs

density of 10^{14}–10^{15} m^{-3}. Thus, the homogeneity depends mainly on the position of the Cs oven and the amount of sticking. A statistical analysis of the vertical Cs distribution for several month of operation revealed that the highest frequency occurs at a roughly doubled Cs density at the top LOS compared to the bottom LOS in vacuum phases as a consequence of the asymmetric Cs evaporation from the top part of the source.

A strongly differing Cs dynamics during plasma phases has been found experimentally. Due to plasma-induced redistribution processes, as chemical sputtering out of Cs compounds, the volume density of Cs is strongly increased: the density of neutral Cs is in the order of 10^{15} m^{-3} and Cs is ionized in a large fraction ($> 90\%$) as well. In addition, Cs is distributed much more homogeneous inside the source: a statistical analysis revealed the highest frequency for almost vertical symmetric distribution at a vertical symmetry of 0–0.25 (a value of zero reflects perfect symmetry). Thus, a homogeneous evaporation of Cs is not necessarily required in order to achieve homogeneous Cs conditions. The Cs redistribution in plasma phases shows a kind of memory effect since it depends much more on the amount of Cs reservoirs (pure Cs in combination with Cs compounds) on the wall, and thus on the history of Cs evaporation, than on the actual Cs evaporation rate. The requirement of Cs reservoirs inside the source is especially pronounced in long plasma pulses: if not a sufficient amount of Cs has been evaporated into the source in the past, Cs can be depleted during long (> 100 s) pulses, where particularly the amount of co-extracted electrons reacts very sensitive. The strongly differing Cs dynamics during plasma and vacuum phases can be observed by the Cs absorption spectroscopy, making it the favorable diagnostics for caesium in the source.

A comparison of the neutral Cs density during plasma pulses with the source performance revealed a correlation during the Cs conditioning phase at short term (during one day), however, not at long term (for different experimental campaigns) – resulting in a different required amount of neutral Cs flux towards the conversion grid. This can either be caused by the necessity of taking into account the flux of Cs ions towards the grid or it can be based on a very sensitive dependence of the required Cs flux on the amount of impurities and thus being very sensitive on the complex surface layers consisting of vacuum impurities, Cs compounds and elemental Cs at the surfaces. Therefore, a controlled feedback system adjusting the Cs evaporation rate to a certain neutral Cs density is not possible – which would have simplified the operation of the ion source. Nevertheless, it was found that the neutral Cs density during plasma phases is always in the order of 10^{15} m^{-3}

when achieving high source performance, which gives at least hints regarding the required amount of Cs evaporation. It was also seen that the performance is not sensitive on the current Cs density in plasma phases for a well conditioned source, because a Cs coverage of multiple monolayers on the plasma grid results in the work function of bulk Cs.

For the investigation of the plasma dynamics in the extended boundary layer, the difference of the present magnetic filter field setup at the BATMAN test facility, using permanent magnets with an axial distance of 9 cm to the plasma grid, in comparison to the original setup, which uses an axial distance of 3 cm, has to be taken into account when comparing to former results. Multiple source diagnostics have been applied at the same time in an axial distance of 0.7 cm and 2.2 cm to the plasma grid to find correlations with the source performance. Simultaneous measurement is required because achieving the same source performance at the same parameters (e.g. Cs evaporation rate) is rarely possible: although the prototype source is able to achieve the same high performance in different experimental campaigns, the complex Cs dynamics mentioned above can lead to different Cs conditions in different experimental campaigns. In addition to the routinely applied Cs absorption spectroscopy for the determination of the neutral Cs density, the LOS-averaged volume density of negative hydrogen ions is determined via cavity ring-down spectroscopy. Langmuir probe measurements reveal the local plasma potential and therefore the potential profile in the sheath close to the conversion grid and additionally the positive ion density and electron temperature. The vertical symmetry of the plasma (defined as the symmetry of positive ions) can be determined in this way as well as electron fluxes in the extended boundary layer, in which the electron density is calculated as the difference between the positive ion density and the negative hydrogen ion density due to the quasi-neutrality of the plasma. The determination of the sheath potential profile is of particular importance since it directly influences electron fluxes from the bulk plasma towards the plasma grid.

A comparison of the measurements in the extended boundary layer with the driver plasma is desirable. By characterizing the driver plasma, statements about the flux of conversion particles towards the plasma grid can be made. For this purpose, a former characterization of the driver plasma by means of optical emission spectroscopy has been used.

Measurements have been carried out for comparing the isotopes hydrogen and deuterium at two source pressures, 0.45 Pa and 0.6 Pa. The pressure of 0.6 Pa has

been chosen since it is a standard operational pressure of the prototype source and therefore a comparison with former measurements is possible, whereas the lower pressure is more relevant for the development of the ITER source, which has to operate at 0.3 Pa.

When comparing local plasma parameters with the source performance averaged over the plasma grid, the plasma symmetry has to be taken into account. The vertical symmetry is influenced by the bias due to a varying axial electric field distribution, leading to a change of the dominant $\vec{E} \times \vec{B}$ drift. With the present magnetic filter field setup, an almost vertical symmetric plasma distribution has been found at low applied bias voltages whereas the asymmetry has been increased to a value of 1–2 at high applied bias. However, no significant change in the symmetry has been determined for varying source pressure or isotope if values at the same sheath potential profile are compared. A qualitative comparison of the plasma symmetry with the H$^-$ symmetry has shown a more homogeneous distribution of H$^-$ compared to positive ions, which is a consequence of the high relevance of H$^-$ production out of conversion of neutral H. The latter is dominantly produced in the driver and thus is not affected by the plasma drift.

The H$^-$ density is increased during the conditioning process from 10^{16} m^{-3} up to 10^{17} m^{-3} when achieving high source performance. The extracted negative hydrogen ion density $j_{\text{H-}}$ and its volume density $n_{\text{H-}}$ measured in the extended boundary layer correlates almost linearly during Cs conditioning for constant operational parameters as well as for varying RF power. This correlation shows the link of the source performance with parameters inside the extended boundary layer. In particular, an increase of $n_{\text{D-}}/j_{\text{D-}}$ by almost a factor of $\sqrt{2}$ has been observed in deuterium compared to hydrogen operation due to the mass difference, showing that the physics in the boundary layer is basically the same in both isotopes.

No significant isotope effect happens regarding the amount of extracted H$^-$ and D$^-$ current density, respectively. For this reason, the flux of produced H$^-$ and D$^-$ particles is similar, resulting in a measured increased D$^-$ density due to the doubled mass. This dependency agrees well with the former measurement of the driver plasma, where an increased dissociation degree in deuterium compared to hydrogen has been determined. Therefore, the flux of conversion particles out of the driver is similar for both isotopes.

The amount of co-extracted electrons is influenced by the potential profile $U_{\text{bias}} - \Phi_{\text{pl}}$ in the sheath of the plasma grid. Since this difference is only varied

by some volts (i.e. from -3 V to $+3$ V) for typically applied bias voltages (i.e. 15–30 V), it is important to determine the local plasma potential in front of the extraction apertures for comparing the sheath potential profile with the source performance. For values of $U_{\mathrm{bias}} - \Phi_{\mathrm{pl}} < 0$ V, electrons are hindered from reaching the plasma grid and thus not removed out of the sheath. In this case, the amount of co-extracted electrons is increased by a factor of 2–4 for lower values of the sheath potential profile at lower bias voltages. As expected from the sheath physics, no significant change of the amount of co-extracted electron happens for $U_{\mathrm{bias}} - \Phi_{\mathrm{pl}} > 0$ V since all electrons from the sheath edge are collected on the plasma grid; however, the co-extracted negative hydrogen ion current density is slightly decreased (up to 10% in the applied bias range) due to the resulting potential barrier for surface produced negative ions.

The flux of electrons towards the plasma grid influences the amount of co-extracted electrons. The electron flux is distributed to the part hitting the plasma grid and thus counting to the bias current, to the part penetrating through the meniscus and thus being co-extracted out of the source, or it is reflected back to the bulk plasma by collisions or a potential barrier. A quantitative comparison of the electron current towards the PG in the boundary layer with the sum of bias and co-extracted electron current (i.e. 20–30 A) results in an overestimation of the electron flux towards the PG of more than one order of magnitude (i.e. > 100 A) if a simple isotropic electron velocity distribution in the boundary layer is assumed, whereas a hindered transport perpendicular to the magnetic field lines results into a slight underestimation (i.e. ≈ 16 A). This shows that the electron transport is clearly affected by the magnetic field close to the PG, containing additionally axial magnetic field components.

Qualitative balancing of the electron flux in the boundary layer with the bias and co-extracted electron current for varying source pressure yields the same flux in the boundary layer at lower source pressure, whereas the distribution is shifted to a larger amount of co-extracted electrons compared to the bias current. A comparison of hydrogen with deuterium operation reveals an increased positive ion density in the extended boundary layer from about 3×10^{17} m^{-3} to a value of 5–6 $\times 10^{17}$ m^{-3} in deuterium operation. Since the difference in the negative hydrogen ion density is smaller in the order of 10^{16} m^{-3}, the electron flux is increased in deuterium. This results in a slight increase of the bias current and a large increase of the measured amount of co-extracted electrons by a factor of up to six. The reason for the different distribution must be a consequence of the

complex electron transport in the magnetic field with complex 3D structure close to the plasma grid, which is unfortunately not accessible with source diagnostics. The source performance is determined by the plasma parameters at the plasma meniscus, which is the boundary between the source plasma and the extracted particle beam. A theoretical approach by modeling is an ongoing task, for which the experimental results carried out during this work are of high importance for use as input data and for benchmarking.

Bibliography

[1] M. Shimada, *et al.*, *Chapter 1: Overview and summary*. Nuclear Fusion **47** (6), 1 (2007).

[2] U. Stroth, *Plasmaphysik – Phänomene, Grundlagen, Anwendungen*, vol. 1 (Vieweg+Teubner, 2011).

[3] ITER Organization, website (2013). Available online at `http://www.iter.org`; visited on November 21 2013.

[4] D. R. Mikkelsen, C. E. Singer, *Optimization of Steady-State Beam-Driven Tokamak Reactors*. Fusion Science and Technology **4**, 237 (1983).

[5] J. Jacquinot, M. Keilhacker, P. Rebut, *Chapter 2: Mission and Highlights of the JET Joint Undertaking: 1978-1999*. Fusion Science and Technology **53** (4), 866 (2008).

[6] C. Gormezano, *et al.*, *Chapter 6: Steady state operation*. Nuclear Fusion **47** (6), 285 (2007).

[7] D. Lide, *CRC Handbook of Chemistry and Physics* (CRC press, 2002), 88th edn.

[8] K. Berkner, R. Pyle, J. Stearns, *Intense, mixed-energy hydrogen beams for CTR injection*. Nuclear Fusion **15** (2), 249 (1975).

[9] A. Krylov, R. Hemsworth, *Gas flow and related beam losses in the ITER neutral beam injector*. Fusion Engineering and Design **81** (19), 2239 (2006).

[10] E. Speth, *et al.*, *Overview of the RF source development programme at IPP Garching*. Nuclear Fusion **46** (6), 220 (2006).

[11] R. S. Hemsworth, A. Tanga, V. Antoni, *Status of the ITER neutral beam injection system*. Review of Scientific Instruments **79** (2), 02C109 (2008).

[12] A. Masiello, *et al.*, *The European contribution to the development of the ITER NB injector*. Fusion Engineering and Design **86** (6-8), 860 (2011).

[13] W. Kraus, *et al.*, *The development of the radio frequency driven negative ion source for neutral beam injectors*. Review of Scientific Instruments **83** (2), 02B104 (2012).

[14] P. Franzen, *et al.*, *RADI—A RF source size-scaling experiment towards the ITER neutral beam negative ion source*. Fusion Engineering and Design **82** (4), 407 (2007).

[15] P. Franzen, *et al.*, *Physical and Experimental Background of the Design of the ELISE Test Facility*. AIP Conference Proceedings **1097** (1), 451 (2009).

[16] M. Bacal, *Physics aspects of negative ion sources*. Nuclear Fusion **46** (6), 250 (2006).

[17] M. Bacal, C. Michaut, L. I. Elizarov, F. El Balghiti, *Basic processes of negative hydrogen ion production and destruction in sources and beams (invited)*. Review of Scientific Instruments **67** (3), 1138 (1996).

[18] P. W. van Amersfoort, *et al.*, *Formation of negative hydrogen ions on a cesiated W(110) surface; the influence of hydrogen implantation*. Journal of Applied Physics **58** (9), 3566 (1985).

[19] B. Rasser, J. V. Wunnik, J. Los, *Theoretical models of the negative ionization of hydrogen on clean tungsten, cesiated tungsten and cesium surfaces at low energies*. Surface Science **118** (3), 697 (1982).

[20] Y. Belchenko, G. Dimov, V. Dudnikov, *A powerful injector of neutrals with a surface-plasma source of negative ions*. Nuclear Fusion **14** (1), 113 (1974).

[21] R. G. Wilson, *Electron and Ion Emission from Polycrystalline Surfaces of Be, Ti, Cr, Ni, Cu, Pt, and Type-304 Stainless Steel in Cesium Vapor*. Journal of Applied Physics **37** (8), 3161 (1966).

[22] R. G. Wilson, *Electron and Ion Emission from Polycrystalline Surfaces of Nb, Mo, Ta, W, Re, Os, and Ir in Cesium Vapor*. Journal of Applied Physics **37**, 4125 (1966).

[23] B. S. Lee, M. Seidl, *Surface production of H^- ions by hyperthermal hydrogen atoms*. Applied Physics Letters **61** (24), 2857 (1992).

[24] J. D. Isenberg, H. J. Kwon, M. Seidl, *Surface production of H^- ions by backscattering of H^+ and H_2^+ ions in the 3–50 eV ion energy range*. AIP Conference Proceedings **287** (1), 38 (1992).

[25] D. Wünderlich, R. Gutser, U. Fantz, *PIC code for the plasma sheath in large caesiated RF sources for negative hydrogen ions*. Plasma Sources Science and Technology **18** (4), 045031 (2009).

[26] R. K. Janev, W. D. Langer, *Elementary processes in hydrogen-helium plasmas* (Springer, 1987).

[27] D. Wünderlich, private communication (2014).

[28] B. Heinemann, *et al.*, *Design of the "half-size" ITER neutral beam source for the test facility ELISE*. Fusion Engineering and Design **84** (2-6), 915 (2009).

[29] P. Franzen, *et al.*, *Magnetic filter field dependence of the performance of the RF driven IPP prototype source for negative hydrogen ions*. Plasma Physics and Controlled Fusion **53** (11), 115006 (2011).

[30] K. N. Leung, K. W. Ehlers, M. Bacal, *Extraction of volume-produced H^- ions from a multicusp source*. Review of Scientific Instruments **54** (1), 56 (1983).

[31] M. A. Lieberman, A. J. Lichtenberg, *Principles of Plasma Discharges and Materials Processing* (Wiley Interscience, 2005), second edn.

[32] P. Chabert, N. Braithwaite, *Physics of Radio-Frequency Plasmas* (Cambridge University Press, 2011), first edn.

[33] R. Gutser, D. Wünderlich, U. Fantz, the NNBI-Team, *Negative hydrogen ion transport in RF-driven ion sources for ITER NBI*. Plasma Physics and Controlled Fusion **51** (4), 045005 (2009).

[34] C. L. Longmire, M. N. Rosenbluth, *Diffusion of Charged Particles across a Magnetic Field*. Phys. Rev. **103**, 507 (1956).

[35] U. Fantz, L. Schiesko, D. Wünderlich, NNBI-Team, *A comparison of hydrogen and deuterium plasmas in the IPP prototype ion source for fusion*. AIP Conference Proceedings **1515** (1), 187 (2013).

[36] L. Schiesko, P. McNeely, P. Franzen, U. Fantz, the NNBI Team, *Magnetic field dependence of the plasma properties in a negative hydrogen ion source for fusion*. Plasma Physics and Controlled Fusion **54** (10), 105002 (2012).

[37] S. Christ-Koch, U. Fantz, M. Berger, the NNBI-Team, *Laser photodetachment on a high power, low pressure rf-driven negative hydrogen ion source*. Plasma Sources Science and Technology **18** (2), 025003 (2009).

[38] P. McNeely, S. V. Dudin, S. Christ-Koch, U. Fantz, the NNBI-Team, *A Langmuir probe system for high power RF-driven negative ion sources on high potential*. Plasma Sources Science and Technology **18** (1), 014011 (2009).

[39] M. Berger, U. Fantz, S. Christ-Koch, the NNBI-Team, *Cavity ring-down spectroscopy on a high power rf driven source for negative hydrogen ions*. Plasma Sources Science and Technology **18** (2), 025004 (2009).

[40] U. Fantz, C. Wimmer, the NNBI-Team, *Quantification of Cesium in Negative Hydrogen Ion Sources by Laser Absorption Spectroscopy*. AIP Conference Proceedings **1390** (1), 348 (2011).

[41] U. Fantz, *et al.*, *Spectroscopy – a powerful diagnostic tool in source development*. Nuclear Fusion **46** (6), 297 (2006).

[42] D. Wünderlich, S. Mochalskyy, U. Fantz, P. Franzen, the NNBI-Team, *Modelling the ion source for ITER NBI: from the generation of negative hydrogen ions to their extraction*. Plasma Sources Science and Technology **23** (1), 015008 (2014).

[43] W. Eckstein, J. Biersack, *Reflection of low-energy hydrogen from solids*. Applied Physics A **38** (2), 123 (1985).

[44] A. Manhard, U. Fantz, A. Stäbler, H. Greuner, B. Crowley, Spectroscopic studies on positive ion based neutral beam injection systems, *Tech. Rep. 4/289*, Max-Planck-Institut für Plasmaphysik (2008).

[45] J. B. Taylor, I. Langmuir, *Vapor Pressure of Caesium by the Positive Ion Method*. Phys. Rev. **51**, 753 (1937).

[46] L. Pauling, *Atomic Radii and Interatomic Distances in Metals*. Journal of the American Chemical Society **69** (3), 542 (1947).

[47] U. Fantz, C. Wimmer, *Optimizing the laser absorption technique for quantification of caesium densities in negative hydrogen ion sources*. Journal of Physics D: Applied Physics **44** (33), 335202 (2011).

[48] R. Gutser, *Experiments and Simulations for the Dynamics of Cesium in Negative Hydrogen Ion Sources for ITER N-NBI*, Ph.D. thesis, Universität Augsburg (2010).

[49] U. Fantz, R. Gutser, C. Wimmer, *Fundamental experiments on evaporation of cesium in ion sources.* Review of Scientific Instruments **81** (2), 02B102 (2010).

[50] C. J. Sansonetti, K. L. Andrew, *Spectrum and energy levels of singly ionized cesium: I. Revision and extension of the Cs II energy levels.* J. Opt. Soc. Am. B **3** (3), 386 (1986).

[51] R. Gutser, C. Wimmer, U. Fantz, *Work function measurements during plasma exposition at conditions relevant in negative ion sources for the ITER neutral beam injection.* Review of Scientific Instruments **82** (2), 023506 (2011).

[52] Y. Oka, *et al.*, *Studies of H^- source for large helical device-neutral beam injector (invited).* Review of Scientific Instruments **75** (5), 1803 (2004).

[53] U. Fantz, R. Friedl, M. Fröschle, *Controllable evaporation of cesium from a dispenser oven.* Review of Scientific Instruments **83** (12), 123305 (2012).

[54] H. B. Michaelson, *The work function of the elements and its periodicity.* Journal of Applied Physics **48** (11), 4729 (1977).

[55] F. Stienkemeier, M. Wewer, F. Meier, H. O. Lutz, *Langmuir–Taylor surface ionization of alkali (Li, Na, K) and alkaline earth (Ca, Sr, Ba) atoms attached to helium droplets.* Review of Scientific Instruments **71** (9), 3480 (2000).

[56] U. Fantz, C. Wimmer, *Cesium dynamics in long pulse operation of negative hydrogen ion sources for fusion.* Review of Scientific Instruments **83** (2), 02B110 (2012).

[57] A. P. Thorne, *Spectrophysics*, vol. 2 (Chapman and Hall, 1988).

[58] S. Briefi, C. Wimmer, U. Fantz, *Correction factors for saturation effects in white light and laser absorption spectroscopy for application to low pressure plasmas.* Physics of Plasmas **19** (5), 053501 (2012).

[59] C. Wimmer, *Laserabsorptionsspektroskopie zur Quantifizierung von Cäsium*, Diploma thesis, Universität Augsburg (2010).

[60] A. O'Keefe, D. A. G. Deacon, *Cavity ring–down optical spectrometer for absorption measurements using pulsed laser sources.* Review of Scientific Instruments **59** (12), 2544 (1988).

[61] M. Berger, *Cavity-Ringdown-Spektroskopie an Wasserstoff-Niederdruck-plasmen*, Ph.D. thesis, Universität Augsburg (2006).

[62] C. Barnett, *et al.*, *Atomic data for controlled fusion research* (1977).

[63] G. Berden, R. Peeters, G. Meijer, *Cavity ring-down spectroscopy: Experimental schemes and applications.* International Reviews in Physical Chemistry **19** (4), 565 (2000).

[64] K. K. Lehmann, D. Romanini, *The superposition principle and cavity ring-down spectroscopy.* The Journal of Chemical Physics **105** (23), 10263 (1996).

[65] H. M. Mott-Smith, I. Langmuir, *The Theory of Collectors in Gaseous Discharges.* Phys. Rev. **28**, 727 (1926).

[66] F. F. Chen, *Langmuir probes in RF plasma: surprising validity of OML theory.* Plasma Sources Science and Technology **18** (3), 035012 (2009).

[67] J. E. Allen, R. L. F. Boyd, P. Reynolds, *The Collection of Positive Ions by a Probe Immersed in a Plasma.* Proceedings of the Physical Society. Section B **70** (3), 297 (1957).

[68] I. B. Bernstein, I. N. Rabinowitz, *Theory of Electrostatic Probes in a Low-Density Plasma.* Physics of Fluids (1958-1988) **2** (2), 112 (1959).

[69] J. Laframboise, *Theory of spherical and cylindrical langmuir probes in a collisionless, maxwellian plasma at rest.* UTIAS Report **100** (1966).

[70] F. F. Chen, *Lecture Notes on Langmuir Probe Diagnostics* (2003).

[71] R. H. Huddlestone, S. L. Leonard, *Plasma Diagnostic Techniques* (Academic Press, 1965).

[72] S. Linnane, M. B. Hopkins, *Analysis of an uncompensated Langmuir probe in a radio frequency plasma.* Plasma Sources Science and Technology **18** (4), 045017 (2009).

[73] V. A. Godyak, R. B. Piejak, B. M. Alexandrovich, *Measurement of electron energy distribution in low-pressure RF discharges.* Plasma Sources Science and Technology **1** (1), 36 (1992).

[74] P. Scheubert, U. Fantz, P. Awakowicz, H. Paulin, *Experimental and theoretical characterization of an inductively coupled plasma source.* Journal of Applied Physics **90** (2), 587 (2001).

[75] J. Dörfler, *Vergleich der Plasmaparameter induktiv gekoppelter Niederdruckplasmen bei 27,12 MHz und bei 2 MHz*, Master thesis (in preparation), Universität Augsburg (2014).

[76] J. Bredin, P. Chabert, A. Aanesland, *Langmuir probe analysis of highly electronegative plasmas.* Applied Physics Letters **102** (15), 154107 (2013).

[77] A. Y. Wong, D. L. Mamas, D. Arnush, *Negative ion plasmas.* Physics of Fluids (1958-1988) **18** (11), 1489 (1975).

[78] P. McNeely, L. Schiesko, *Investigation of fringe plasma parameters on a high power rf driven ion source.* Review of Scientific Instruments **81** (2), 02B111 (2010).

[79] L. Schiesko, P. McNeely, U. Fantz, P. Franzen, the NNBI-Team, *Caesium influence on plasma parameters and source performance during conditioning of the prototype ITER neutral beam injector negative ion source.* Plasma Physics and Controlled Fusion **53** (8), 085029 (2011).

[80] D. Wünderlich, S. Dietrich, U. Fantz, *Application of a collisional radiative model to atomic hydrogen for diagnostic purposes.* Journal of Quantitative Spectroscopy and Radiative Transfer **110** (1-2), 62 (2009).

[81] U. Fantz, D. Wünderlich, *Atomic and Molecular Collisional Radiative Modeling for Spectroscopy of Low Temperature and Magnetic Fusion Plasmas.* AIP Conference Proceedings **1344** (1), 204 (2011).

[82] P. Franzen, U. Fantz, *On the NBI System for Substantial Current Drive in a Fusion Power Plant: Status and R&D Needs.* Fusion Engineering and Design (2014). Submitted.

[83] R. Friedl, *Experimental investigations on the caesium dynamics in H_2/D_2 low temperature plasmas*, Ph.D. thesis, Universität Augsburg (2013).

[84] U. Fantz, *et al.*, *Diagnostics of the cesium amount in an RF negative ion source and the correlation with the extracted current density.* Fusion Engineering and Design **74** (1-4), 299 (2005).

[85] A. Lorenz, U. Fantz, P. Franzen, Spatially Resolved H_α-Doppler Spectroscopy Applied to a Hydrogen Beam from a Negative Ion Source, *Tech. Rep. 4/285*, Max-Planck-Institut für Plasmaphysik (2006).

[86] B. Ruf, *Reconstruction of Negative Hydrogen Ion Beam Properties from Beamline Diagnostics*, Ph.D. thesis submitted, Universität Augsburg (2014).

[87] H. Nakano, *et al.*, *H^- density profile and response to applied bias and extraction voltages in H^- source.* AIP Conference Proceedings **1515** (1), 237 (2013).

[88] P. Franzen, U. Fantz, the NNBI-Team, *Beam Homogeneity Dependence on the Magnetic Filter Field at the IPP Test Facility MANITU*. AIP Conference Proceedings **1390** (1), 310 (2011).

[89] A. Anders, *A Formulary for Plasma Physics* (Akademie-Verlag Berlin, 1990).

[90] S. J. Buckman, A. V. Phelps, *Vibrational excitation of D_2 by low energy electrons.* The Journal of Chemical Physics **82** (11), 4999 (1985).

[91] Y. Itikawa, *Momentum-transfer cross sections for electron collisions with atoms and molecules.* Atomic Data and Nuclear Data Tables **14** (1), 1 (1974).

[92] I. Bray, D. A. Konovalov, I. E. McCarthy, *Coupled-channel optical calculation of electron-hydrogen scattering: Elastic scattering from 0.5 to 30 eV*. Phys. Rev. A **43**, 5878 (1991).

Acknowledgements

Curriculum Vitae

Name:	Christian Wimmer
Geburtsdatum:	7. Mai 1985 in Augsburg
Nationalität:	Deutsch
Familienstand:	ledig

09/1991 – 07/1995	Grundschule Göggingen-West, Augsburg
09/1995 – 06/2004	Gymnasium bei St. Anna, Augsburg Erwerb der allgemeinen Hochschulreife
09/2004 – 02/2011	Studiengang Diplom Physik an der Universität Augsburg Erwerb des Diploms in Physik
03/2011 – 02/2014	Doktorand am Max-Planck-Institut für Plasmaphysik, Garching: Bereich ITED, Arbeitsgruppe Neutralinjektion

Garching b. München, 10. Juni 2014